VYSOKÉ UČENÍ TECHNICKÉ V BRNĚ
BRNO UNIVERSITY OF TECHNOLOGY

FAKULTA STROJNÍHO INŽENÝRSTVÍ
ÚSTAV MECHANIKY TĚLES, MECHATRONIKY
A BIOMECHANIKY
FACULTY OF MECHANICAL ENGINEERING
INSTITUTE OF SOLID MECHANICS, MECHATRONICS AND BIOMECHANISC

VLIV GEOMETRICKÝCH PARAMETRŮ NA RIZIKO RUPTURY U VÝDUTĚ BŘIŠNÍ AORTY

INFLUENCE OF GEOMETRICAL PARAMETERS ON RUPTURE RISK OF ABDOMINAL AORTIC ANEURYSM

DISERTAČNÍ PRÁCE
DOCTORAL THESIS

AUTOR PRÁCE
AUTHOR
Ing. Miroslav Zemánek

VEDOUCÍ PRÁCE
SUPERVISOR
Doc. Ing. Jiří Burša Ph.D.

BRNO 2010

ABSTRAKT

Tato práce je zaměřena na problematiku výpočtového a experimentálního modelování deformačně napjatostních stavů měkkých tkání se zaměřením na riziko ruptury u výdutě břišní aorty (AAA).

V první části (kap. 1) je stručně nastíněn současný stav dané problematiky. Tato část shrnuje důležité poznatky publikované v dostupné literatuře. Pozornost je věnována zejména klíčovým faktorům pro stanovení rizika ruptury AAA. V další kapitole (kap. 2) je stručně popsána histologie cévní stěny a její výsledné mechanické chování, jakož i její patologie, především AAA.

Druhá část práce (kap.3) je věnována experimentálnímu vyhodnocování deformačně napjatostního chování měkkých tkání, které je nutným předpokladem k věrohodnému výpočtovému modelování tohoto chování. V této kapitole je stručně popsáno experimentální zařízení speciálně vyvinuté pro testování měkkých tkání a typy zkoušek, které lze na tomto zařízení provádět. Dále jsou shrnuty klíčové faktory ovlivňující deformačně napjatostní chování měkkých tkání a experimentální ověření těchto faktorů na vzorcích z prasečích hrudních aort. V závěru této kapitoly jsou shrnuty nové poznatky vyplývající z experimentálního testování.

Třetí část disertační práce (kap.4) je zaměřena na matematický popis deformačně napjatostního chování měkkých tkání, stručný popis používaných konstitutivních vztahu a postup při identifikaci parametrů pro tyto konstitutivní modely určované na základě provedených experimentálních zkoušek.

Poslední část disertační práce (kap.5) je věnována výpočtovému modelování deformačně napjatostního chování AAA. V této kapitole jsou nejdříve shrnuty klíčové faktory a předpoklady pro vytváření modelů a pro vyhodnocování výsledku a dále jsou uvedeny materiálové parametry pro konstitutivní modely implementované do programu ANSYS. Byly provedeny testovací výpočty při použití hypotetické zjednodušené geometrie AAA, na kterých byly vyhodnoceny vlivy změny geometrie a vliv změny konsitutivního modelu na extrémní napětí ve stěně AAA. U reálné geometrie AAA byla navržena a otestována metoda výpočtu nezatížené geometrie z reálných CT snímků. Dále byl testován vliv zvýšení vnitřního tlaku jako rizika ruptury AAA.

V závěru práce jsou shrnuty poznatky a možnosti výpočtového modelování a návrhy na další práce.

KLÍČOVÁ SLOVA

Biologické měkké tkáně, výduť břišní aorty, zkouška ve víceosé napjatosti, hyperleasticita, hustota energie napjatosti.

SUMMARY

The main objective of this thesis is finite element and experimental modeling of stress-strain states of the soft tissues specially focused on rupture risk of abdominal aortic aneurysm (AAA).

The first chapter (chap. 1) summarizes the present state of the mentioned problematic and the major information published in the present-day literature. The key factors for AAA rupture risk decision are also summarized in this chapter. The next chapter (chap. 2) describe the artery wall histology, type of aneurysms and mechanical behavior of artery wall.

The second part of the thesis (chap. 3) is focused on experimental modeling of stress-strain states of soft tissues which is necessary for reliable finite element modeling of this behavior. In this chapter a specially designed and produced experimental testing rig is described and the type of tests which is possible to realize with this testing rig. The key factors influencing the stress-strain behavior of the aortic tissue are also summarized and experimentaly tested on porcine thoracic aortas. The new knowledge resulting from experimental testing are summarized at the end of this chapter.

The intention of third part (chap. 4) is the mathematical description of the stress-strain behavior of soft tissues, description of frequently used constitutive models and the parameter identification for these constitutive models based on the realized tension tests.

The last chapter (chap. 5) is devoted to finite element modeling of the stress-strain states of AAA behavior. First the key factors and assumptions for finite element models creation and evaluation are summarized as well as the material parameters of the constitutive models which are implemented in ANSYS software. Several simulations were realized using hypothetical AAA geometry where the impact of some geometrical parameters change was tested. The backward incremental method using for evaluation of unloading state was designed and tested at real AAA geometry reconstructed from CT scans. Hypertension as one of the key factor for AAA rupture risk was tested using unloaded geometry.

The new knowledge and possibilities of finite element modeling are summarized at the end of this thesis. The proposals to next research work is also summarized.

KEYWORDS

Soft tissue, abdominal aortic aneurysm, biaxial tension tests, hyperelasticity, strain energy density.

Prohlašuji, že tuto disertační práci jsem vypracoval samostatně a s použitím odborné literatury a dalších informačních zdrojů, které jsou všechny citovány. V disertační práci jsem použil také texty a informace z článků, ve kterých jsem autor nebo spoluautor.

Práce je sepsána v anglickém jazyce.

I herewith declare that I have personally penned the doctoral thesis. I have only used the mentioned sources and utilities and have marked parts copied from elsewhere, either literally or by content as such. I have also used the texts and informations from author´s and co-author´s publications.

The doctoral thesis is written in English language.

Ing. Zemánek Miroslav

ACKNOWLEDGMENTS

I wish to express my deep gratitude to my supervisor Doc. Ing. Jiří Burša Ph.D. for all guidance, tremendous support and encouragement throughout my research. I also express many thanks to Ing. Michal Děták for all his helps in experimental part of the work.

The work could not be realized without the cooperation with St. Ann Hospital in Brno, Clinics of Imaging Methods in acquisition and evaluation of CT scans which is highly appreciated.

I would also like to thank my family for the support they provided me.

TABLE OF CONTENTS

LIST OF TABLES

LIST OF FIGURES

NOMENCLATURE

AAA		Abdominal Aortic Aneurysm
ANSYS		Finite element analysis software from ANSYS Inc.
ABAQUS		Finite element analysis software from DS Simulia.
CCD		Charge-Coupled Device
CTA		Computer Tomography Angiography
FEA		Finite element analysis
FEM		Finite element method
FEAP		Finite element analysis program written by Prof. R.L.Taylor.
ILT		Intra-Luminal Thrombus
PC		Personal Computer
PDS		Probabilistic design system
ProE		Pro/engineer software from PTC corp.
NaCl		Sodium chloride
nD		n dimensional (n = 1, 2, 3)
SCOPUS		International abstract and citation database
STATISTICA		Statistical sofrware from StatSoft company
TAA		Thoracic Aortic Aneurysm
TIBIXUS		Off-line image analysis software written by Ing. P. Skácel Ph.D.
X-ray		X-radiation (Röntgen radiation)
A, B		Artery layer (chapter: 4.2.7)
E	[Pa]	Young´s modulus
F	[-]	Deformation gradient tensor
E_{ij}	[-]	Green Lagrange strain tensor (i,j = 1, 2, 3)
E_{ij}	[-]	Almansi Hamel strain tensor (i,j = 1, 2, 3)
e_{ij}	[-]	Logarithmic (natural) strain (i,j = 1, 2, 3)
e	[m]	Aneurysm eccentricity
F	[N]	Force
F_R (f_r)	[-]	Dimensionless parameter – radius ratio (chapter: 5.4.1)
F_L (f_l)	[-]	Dimensionless parameter – length vs. radius (chapter: 5.4.1)
F_E (f_e)	[-]	Dimensionless parameter - eccentricity (chapter: 5.4.1)
h	[m]	Artery wall thickness
pH	[-]	potential of Hydrogen
ln	[-]	natural logarithm
L		loss function (chapter: 4.3.2)
L	[m]	Deformed length
L_0	[m]	Original length
Lan	[m]	Aneurysm length
Ra	[m]	Artery radius
Ran	[m]	Aneurysm radius
SD	[%]	Standard Deviation
λ	[-]	Stretch ratio
μ	[-]	Poisson ratio
σ_{ij}	[Pa]	Cauchy stress tensor (i,j = 1, 2, 3)

σ_1	[Pa]	first (maximum) principal Cauchy stress
σ_2	[Pa]	second principal Cauchy stress
σ_{1nom}	[Pa]	maximum principal Cauchy stress at normal (nominal) part of the artery
S_{ij}	[Pa]	2. Piola Kirchhoff stress tensor (i,j = 1, 2, 3)
T_{ij}	[Pa]	1. Piola Kirchhoff stress tensor (i,j = 1, 2, 3)
$W, \overline{W}$	[J/m^3; Pa]	Strain energy density function
a, b, d		material parameters (chapter: 4.2.1)
A, B, C, D, E, G, H		material parameters (chapter: 4.2.3)
c, b_i		material parameters (chapter: 4.2.4)
c, c_i		material parameters (chapter: 4.2.5)
$\overline{I}_1, \overline{I}_4, \overline{I}_6$		Reduced invariants of right Cauchy-Green def. tensor (chapter: 4.2.6)
c, d, k_1, k_2		material parameters (chapter: 4.2.6)
f^A, f^B		volume fraction factors (chapter: 4.2.7)
f^A, f^M		volume fraction factors (chapter: 5.2.4)
$a_i, b_j, c_k, d_l, e_m, f_n, g_o$		material parameters (chapter: 4.2.9)
φ	[°]	angle of reinforcing fibres (chapter: 4.2.6 and 4.2.7)
α	[°]	angle between AAA and normal part of artery
w_1, w_2		weighting factors (chapter: 4.3.1)
f_s		stress-based nonlinear function (chapter: 4.3.1)
f_w		energy-based nonlinear function (chapter: 4.3.1)
ψ_i		Strain energy function (chapter: 4.3.1)

1 MOTIVATION AND INTRODUCTION

1.1 Backround

Abdominal aortic aneurysm (AAA) is a permanent local dilatation of the aorta in its abdominal part (Figure 1-1). A reliable predictor for rupture has not been found yet. Clearly the maximum AAA diameter and its expansion rate are the most frequently used criteria for surgical intervention.

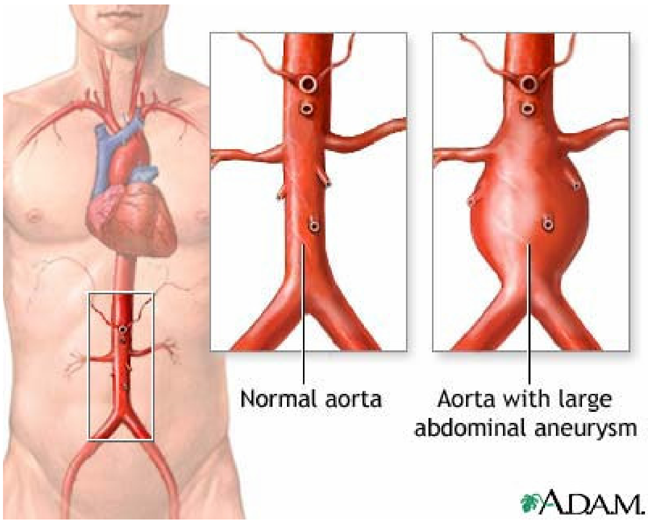

Figure 1-1 Abdominal Aortic Aneurysm (AAA) [65]

1.2 Problem formulation

In order to predict the rupture risk of AAA, the stress in the AAA is computed. There are several difficulties in evaluating the stress for example to get material properties (mechanical properties), geometrical properties (initial shape and thickness) and boundary conditions (loading pressure etc.). The main goal of this doctoral thesis is to determine influence of geometrical parameters on the stress response and on rupture risk of abdominal aortic aneurysm.

1.3 Literature review

Many articles are written on AAAs. In the following chapters the present state of the key factors for AAA rupture risk criteria (1.3.1) and possibilities in 3D FEA modeling (1.3.2) are summarized.

1.3.1 AAA rupture risk criteria described in [35]:

- Maximum diameter – clinical data show that the rupture risk is exponentially related to the maximum AAA diameter. The maximum transverse diameter is taken as the main criterion for judging the necessity of surgical intervention in asymptomatic AAAs because it is easy to measure. Clinically the maximum AAA transversal diameters of 5cm for women and 6cm for men are most commonly used to recommend a surgical intervention.

- Expansion rate – clinically, a high expansion rate, say from 0.5 cm per year and up, is often associated with a high risk of rupture.
- Mechanical stress [27], [35], [36], [37] and [38] – a general consensus is that the AAA peak wall stress (e.g. in comparison with wall stress in the healthy artery) is the best indicator of AAA rupture. Because direct stress measurement in AAA patients are not possible, finite element analysis (FEA) is an efficient tool. For example studies [27], [36] and [38] show maximum of von Mises wall stress distribution along the healty and diseased artery.
- Hypertension – clinically, hypertension is considered to be a key factor contributing to AAA rupture.
- Asymmetry index – in consequence of the local support provided by lumbar vertebrates, most AAAs are asymmetric. Generally, the anterior size is greater than the posterior size with a larger wall thickness at the posterior side. Several studies [45], [58] reported that the effect of asymmetry increase the maximum wall stress.
- Effect of intra-luminal thrombus – an intra-luminal thrombus (ILT) (Figure 1-2 [41]) is an accumulation of fibrin, blood cells, platelets, blood proteins and cellular debris adhering to the AAA inner wall. At present, the effect of ILT on AAA rupture is still controversial. Some investigators [59] think ILT may reduce the stress in the AAA wall in contrast some researches [60] declare that ILT could accelerate AAA rupture.

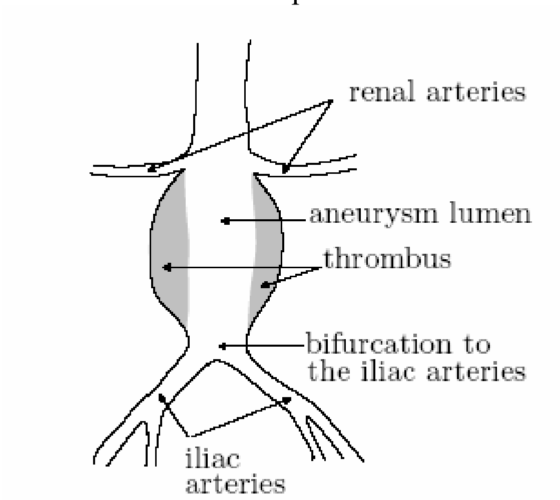

Figure 1-2 Schematic sketch of AAA (from [41])

- Change of wall stiffness and strength – clinical observations [35] show that most AAA walls become progressively stiffer as the diameter increases. This is because of the biomechanical remodelation of the wall. Wall stiffness is not necessarily advantageous for preventing AAA rupture, because along with the increase of wall stiffness, the wall ultimate stress and especially ultimate strain will accordingly decreases [32].
- Saccular index – i.e. the ratio of maximum AAA diameter to the length of AAA region. Clinical observations [35] indicate that the smaller the saccular index the higher is the possibility of AAA rupture.

1.3.2 FEA modeling

Most of recent studies used a 3D model of AAA as a necessary model level for credible conclusions. Some of the studies [27], [36], [45] used hypothetical idealised aneurysm models instead AAA model based and reconstructed from the patient-specific CT scans. A disadvantage of all the medical imaging methods is that they can never provide the unloaded aneurysmal geometry in a living subject which would be the preferred zero-stress starting geometry for a wall stress simulation load sequence. Some studies used the real measured geometry as an unloaded starting point for a simulation and full systolic pressure applied on this geometry. This method causes the size of the systolic geometry may be overestimated. The more recent paper (for details see the next chapter 1.3.3) is based on an inverse modeling approach to compute the unloaded configuration for AAA.

1.3.3 Computational backward method for reconstruction of unloaded AAA

The computational methods developed for predicting the unloaded geometry generally try to overcome the problem with overestimated patient-specific AAA geometry. The following methods are described in the recent literature:

- Backward incremental method [31], [41], [42]. The method described in [31] assumme that entire path of each node in the AAA surface under pressure may be reliably approximated by a straight line. Briefly the basic approach is to first determine displacement field by pressure load applying and assuming it to be stress free and then this displacement field is scaled by a multiplication factor. The method is realized using software ABAQUS in [31]. The method described in [41] and [42] is based on the backward application of iteratively computed forward deformations. Author also used the software ABAQUS and the Neo-Hook constitutive model [63]. Application of backward incremental method in combination with anisotropic constitutive models for arterial wall has not yet been described.
- Inverse elastostatic computational method [43], [44]. The solution for the initial geometry is faciliated via the introduction of the inverse motion which is a mathematical inverse of the forward motion. The approach is to reparametrize the Cauchy stress which is normally a function of the forward deformation gradient in inverse deformation gradient. The implementation of this scheme results in a FEM formulation that involves minimum change to the standard element. The authors used this method in combination with isotropic and anisotropic constitutive models. The inverse procedure has been implemented in an in-house version of a nonlinear FEM code FEAP originally developed at University of California Berkeley by Prof. R.L. Taylor.

2 ARTERIAL HISTOLOGY, MECHANICAL BEHAVIOR AND CLASSIFICATION OF ANEURYSMS

2.1 Arterial histology [8]

This overview is included for the purpose of clarifying the macroscopic and microscopic structure of arterial walls and to provide essential information without a background in biology or physiology. From the macroscopic point of view, arteries are divided into „elastic arteries" (for example: aorta, carotid or iliac arteries) and muscular arteries (for example: femoral, celiac, cerebral arteries). From microscopic point of view, the arterial walls are composed of three distinct layers, the intima (tunica intima), the media (tunica media) and the adventitia (tunica adventitia).

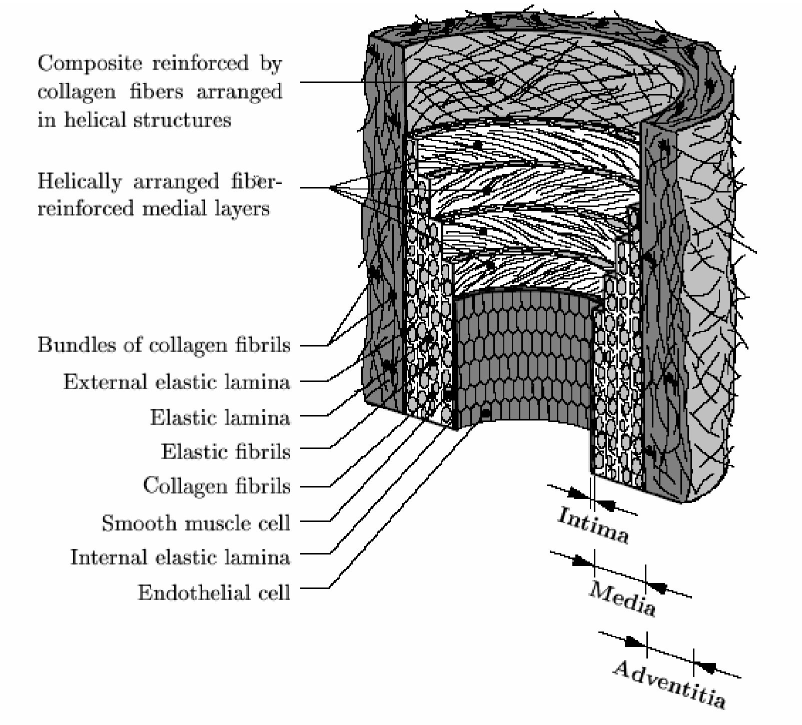

Figure 2-1 Layers in the artery (from [8])

2.1.1 Intima

The intima is a thin layer of a single layer of endothelial cells lining the arterial wall and resting on a thin basal membrane (basal lamina). The thickness and stiffnes varies with topography, age and disease. Pathological changes may be associated with atherosclerosis, the most common disease of arterial walls. It involves deposition of fatty substances, calcium, cellular waste products and fibrin (a clotting material in the blood). The resulting build-up is called atherosclerotic plaque. Hence, the mechanical behavior of atherosclerotic arteries differs significantly from that of healthy arteries.

2.1.2 Media

The media is a thick layer which provides the majority of the strength of arterial wall under physiological deformation. The media consists of a complex three-dimensional network of smooth muscle cells, and elastin and collagen fibrils. The fenestrated elastic laminae separate the media into a varying number of well-defined concentrically fiber-reinforced medial layers. The media is separated from the intima and adventitia by so-called internal elastic lamina and external elastic lamina respectively. The orientation of and close interconnection between the elastic and collagen fibrils, elastic laminae, and smooth muscle cells together constitute a continuous fibrous helix. The helix has a small pitch so that the fibrils in the media are almost circumferentially oriented. This structured arrangement gives the media high strength, resilience and the ability to resist loads in both the longitudinal and circumferential directions. From the mechanical point of view, the media is the most significant layer in arteries except for excessive deformations.

2.1.3 Adventitia

The adventitia consits mainly of fibroblasts and fibrocytes (cells that produce collagen and elastin), histological ground substance and thick bundles of collagen fibrils forming a fibrous tissue. The thickness of the adventitia depends strongly on the type (elastic or muscular) and the physiological function of the blood vessel and its topographical site. When the artery radius is expanded, the wavy collagen fibrils within the network straighten and provide protection from rupture of the artery. The wavy collagen fibrils configuration in adventitia causes that the adventitia is much less stiff in the load-free configuration and at low pressures than the media.

2.2 Typical mechanical behavior of the arterial wall

This section summarizes some of the basic biomechanical features of the arterial wall that result from its structure and are essential for credible modeling of healthy and diseased arterial wall. Generally, arteries are deformable nearly incompressible composite that exhibit highly nonlinear stress-strain responses with a characteristic stiffening at higher pressure [4]. The mechanical properties change along the arterial tree and are different at each of the arterial layers [3]. Arteries are pre-stressed; that is, in their load-free configuration the residual stresses occur in them. A good way of characterizing the residual circumferential stresses is through the opening angle measured after artery cut in a radial direction. The arteries embedded in the body are also under an axial pre-strain; hence, it shortens after excision from the body. Arterial walls exhibit several types of inelastic phenomena. For example, arteries show viscoelastic effects under constant load and hysteresis under cyclic loading [1]. Some properties of the arterial wall were experimentally tested and verified in this doctoral thesis (see. chapter: 3.3).

2.3 Classification of aneurysms [71], [75] and [76]

Aneurysms can be classified in several different ways:

- Morphology – aneurysms can be described by their shape. Traditionally they are described as either fusiform (chapter 2.3.1) or saccular (chapter 2.3.2).
- True or false - as mentioned in chapter 2.1 the aortic wall consists of three layers. If the aneurysm wall still consits of all three layers of the aortic wall, it is called a true aneurysm. If only the outer layer of the aortic wall remains, the aneurysm is called a pseudoaneurysm or false aneurysm (Figure 2-3). Pseudoaneurysms may occur as a result of trauma when the inner layers are torn apart.
- Location - most aneurysms occur in the aorta. The two types of aortic aneurysm are abdominal aortic aneurysm (AAA) (Figure 2-4) and thoracic aortic aneurysm (TAA). Aneurysms that occur in an artery in the brain are called cerebral aneurysms (Figure 2-4) and aneurysms that occur in arteries other than aorta are called peripheral aneurysms.
- Arterial vs. venous – arterial aneurysms are much more common but venous aneurysms do happen (e.g. the popliteal venous aneurysm).
- Aneurysms also can be classified in severeal different ways such as the growth rate of aneurysm or classification based on size of aneurysm (small, medium, large and giant).

Some of the mentioned type of aneurysms are described below:

2.3.1 Fusiform aneurysms

Most fusiform aneurysms are „true aneurysms" (Figure 2-2) and is an outward bulging of the artery wall in all directions.

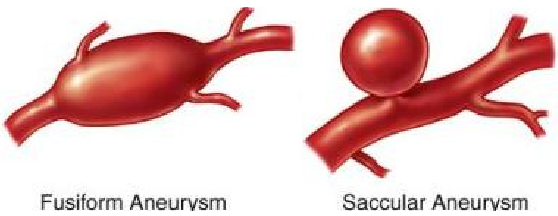

Figure 2-2 Fusiform and saccular aneurysms [76]

2.3.2 Saccular aneurysms

A saccular aneurysm appear to be a smaller blister on the side of the aorta (Figure 2-2). It is asymmetrical (uneven). Saccular aneurysms are typically caused by trauma such as a car accident or by a penetrating aortic ulcer. The cerebral aneurysms are often characterized as a saccular.

2.3.3 Dissecting (false) aneurysms

Dissecting aneurysms occur when a tear begins within the wall of the aorta, causing its three layers to separate. Dissection weakens the wall of the aorta, which enlarges. Dissection may cause aneurysms, but an existing aneurysm may also dissect. Dissections may occur anywhere along the aorta. Treatment depends on the location. Dissections involving the ascending aorta (in the front near the heart) often are treated with emergency surgery. Dissections involving the descending thoracic aorta (in the back) are treated with medication. Although uncommon, dissections are the most common aortic syndrome that causes acute (severe) signs and symptoms. Dissections can be lethal if not treated by surgeons and physicians with expertise in treating this disorder.

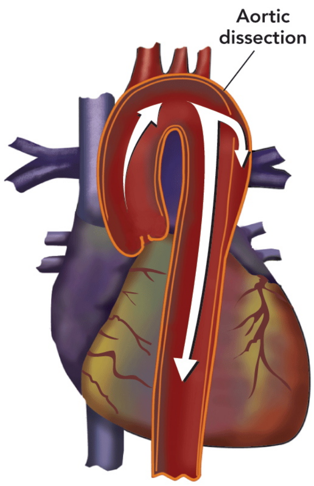

Figure 2-3 Dissecting (false) aneurysms [76]

2.3.4 Abdominal aortic aneurysms

Nearly 75 percent of aortic aneurysms are abdominal (Figure 2-4).Abdominal aortic aneurysms are located along the portion of the aorta that passes through the abdomen, carrying blood to the vital organs until it splits off into two smaller (iliac) arteries that supply blood to the pelvis and legs. Abdominal aortic aneurysms can affect anyone, but most often occur in men ages 40 to 80. Most abdominal aortic aneurysms are caused by atherosclerosis (hardening of the arteries.)

2.3.5 Thoracic aortic aneurysms

Approximately 25 percent of aortic aneurysms are thoracic (Figure 2-4).Thoracic aneurysms can occur anywhere along the aorta above the diaphragm (a membrane separating the chest from the abdomen), including the ascending aorta, the aortic arch, and the descending thoracic aorta.They can result from connective tissue disorders such as Marfan syndrome (i.e. genetic disorder of the connective tissue), previous dissection (separation of the layers of the wall) of the aorta, prolonged hypertension (high blood pressure) and trauma (usually falls or motor vehicle accidents). Thoracic aortic aneurysms also may occur in people who have bicuspid aortic valves, a condition in which two cusps, instead of the normal three, seal the valves when they're closed.

2.3.6 Cerebral aneurysms

Aneurysms that occur in an artery in the brain are called cerebral aneurysms. They are sometimes called berry aneurysms because they are often the size of a small berry. Most cerebral aneurysms produce no symptoms until they become large, begin to leak blood, or rupture. A ruptured cerebral aneurysm causes a stroke. Signs and symptoms can include a sudden, extremely severe headache, nausea, vomiting, stiff neck, sudden weakness in an area of the body, sudden difficulty speaking, and even loss of consciousness, coma, or death. The danger of a cerebral aneurysm depends on its size and location in the brain, whether it leaks or ruptures, and the person's age and overall health.

2.3.7 Peripheral aneurysms

Aneurysms that occur in arteries other than the aorta (and not in the brain) are called peripheral aneurysms. Common locations for peripheral aneurysms include the artery that runs down the back of the thigh behind the knee (popliteal artery), the main artery in the groin (femoral artery), and the main artery in the neck (carotid artery). Peripheral aneurysms are not as likely to rupture as aortic aneurysms, but blood clots can form in peripheral aneurysms. If a blood clot breaks away from the aneurysm, it can block blood flow through the artery. If a peripheral aneurysm is large, it can press on a nearby nerve or vein and cause pain, numbness, or swelling.

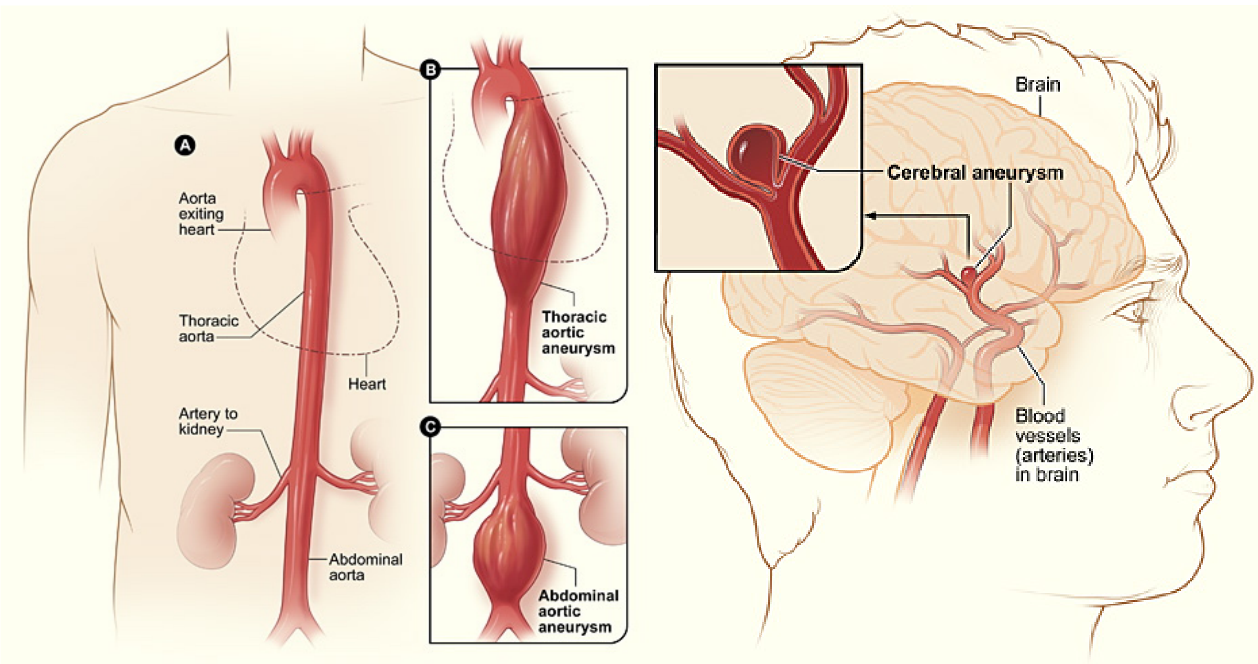

Figure 2-4 Location of aneurysms [76]

2.4 Surgical interventions [66], [67], [68]

Two main types of surgery to repair AAA are open abdominal or open chest repair and endovascular repair. The traditional and most common type of surgery for AAA is open abdominal or open chest repair. It involves a major incision in the abdomen or chest. General anesthesia is needed with this procedure. The aneurysm is slited or removed and the section of aorta is replaced with an artifical graft (Figure 2-5). The surgery takes 3 to 6 hours and it often takes a month to recover from open abdominal or open chest surgery and return to full activity.

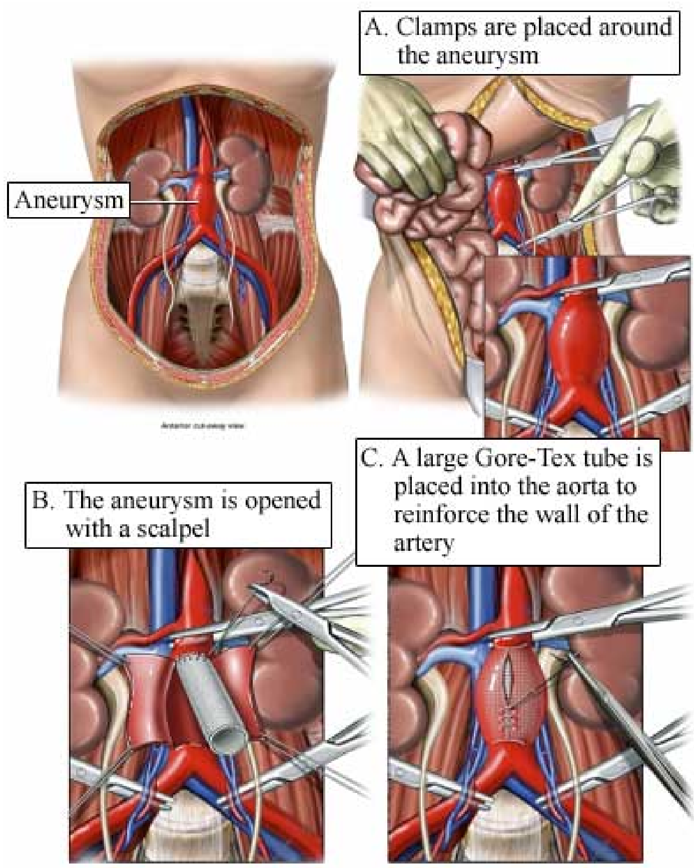

Figure 2-5 Open surgical aneurysm repair [66]

In endovascular repair, the aneurysm is not removed, but a stent graft (Figure 2-6) is inserted into the aorta to strengten it. The stent graft is an implant consisting of an artificial graft with stents to ensure the graft fixation inside the artery. This type of surgery is performed through catheters (tubes) inserted into the arteries; it does not require surgical opening of the chest or abdomen (Figure 2-7). To perform endovascular repair, the doctor first inserts a catheter into an artery in the groin (upper thigh) and threads up to the area of the aneurysm. Then watching it on X-ray, the surgeon threads the stent graft into the aorta to the aneurysm. The graft is then expanded inside the aorta and fastened in place to form a stable channel for blood flow. The graft reinforces the weakened section of the aorta to prevent the aneurysm from rupturing. Endovascular repair surgery reduces recovery time to a few days and greatly reduces the time in hospital. The disadvantage is that not all of the aneurysms can be repaired with this procedure.

Figure 2-6 Endovascular stent graft [69]

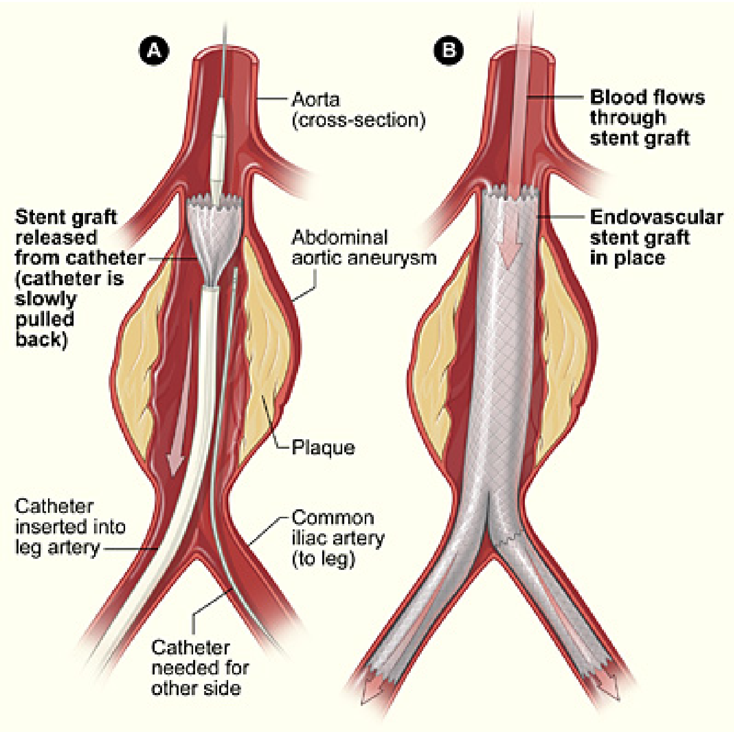

Figure 2-7 Endovascular stent graft treatment of an AAA [67]

3 EXPERIMENTAL STUDY OF MECHANICAL PROPERTIES OF AORTIC TISSUE

Biaxial testing is required to fully characterize anisotropic properties of soft tissues or to set-up biaxial stress-strain states to provide more accurate in vivo simulation. In addition, constitutive models cannot be developed based on uniaxial testing alone because fibres may realign along the loading direction [12]. A tube-like specimen of the whole artery fixed on both ends and loaded by internal pressure is often used for biaxial tension testing but the disadvantages are the possibility to change the strains in both directions independently and the possibility of tesnig of particular arterial layers. Therefore a planar specimen of artery which is loaded in two orhtogonal directions is more frequently used. In cooperation of our institute with the company Camea s.r.o. equipment for biaxial testing of hyperelastic materials (soft tissues and elastomers) has been designed and produced; this is described in chapter 3.1.1 in detail. The source data have been published in author´s publications (VI, VII, VIII).

3.1 Experimental setup and procedure

The experimental setup and procedure comprehends the following tasks:

a) specimen preparation and measurement of the specimen dimensions
b) setup of the boundary conditions for the measurement (temperature, preload etc.)
c) application of defined forces or displacements
d) the measurement of the load and the related deformation of the specimen
e) evaluation of strain (or stretch) and stress values in the directions of loading
f) saving or archiving of the measured and evaluated data

3.1.1 Biaxial testing rig

The testing rig (Figure 3-1) consists of a bedplate carrying two orthogonal ball screws, equiped with force gauges, two servo motors and four carriages ensuring symmetric biaxial deformation of the specimen and a programmable CCD camera located on a support stand. The specimen can be immersed in physiological saline solution with specific *pH* and controlled temperature; the whole test is driven by a PC using a tailored software system. For clamping of specimens, four clips are attached to each of the carriages by a system of levers. The CCD camera is used for contactless evaluation of displacements of created contrast points. The independent control of displacements in both loading directions enables us to obtain stress-strain or stress-stretches characteristic for various types of biaxial stress states that are described in the following chapter 3.1.2.

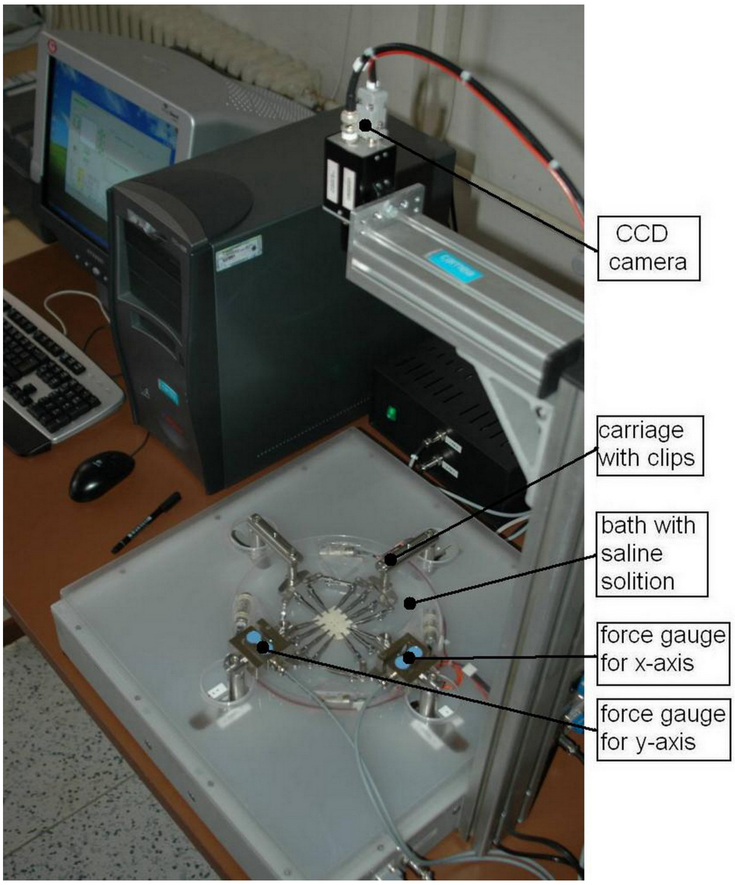

Figure 3-1 General view of testing rig

3.1.2 Type of tests

The independent control of displacements in both directions enables us to obtain the stress-strain characteristics for various states of biaxial tension. Each of these characteristics can be represented as a curve above the plane of strain components (Figure 3-2). It is possible to obtain stress-strain characteristics in the following types of tests:

a) **equibiaxial tension tests** – equal strains in both loading directions (curve 1)
b) **planar tension tests** – uniaxial extension in either „1“ or „2“ direction with constrained (zero) transversal contraction (curves 2 and 3)
c) **proportional tension tests** - biaxial loading with mutually proportional strain components in both loading directions (curve 4)
d) **tension tests with constant transversal strain** – increasing load in either „1“ or „2“ direction and a constant (non-zero) strain in the other one (curves 5 and 6)
e) **uniaxial tension tests** – loading only in either „1“ or „2“ direction with a free transversal contraction (7, 8)

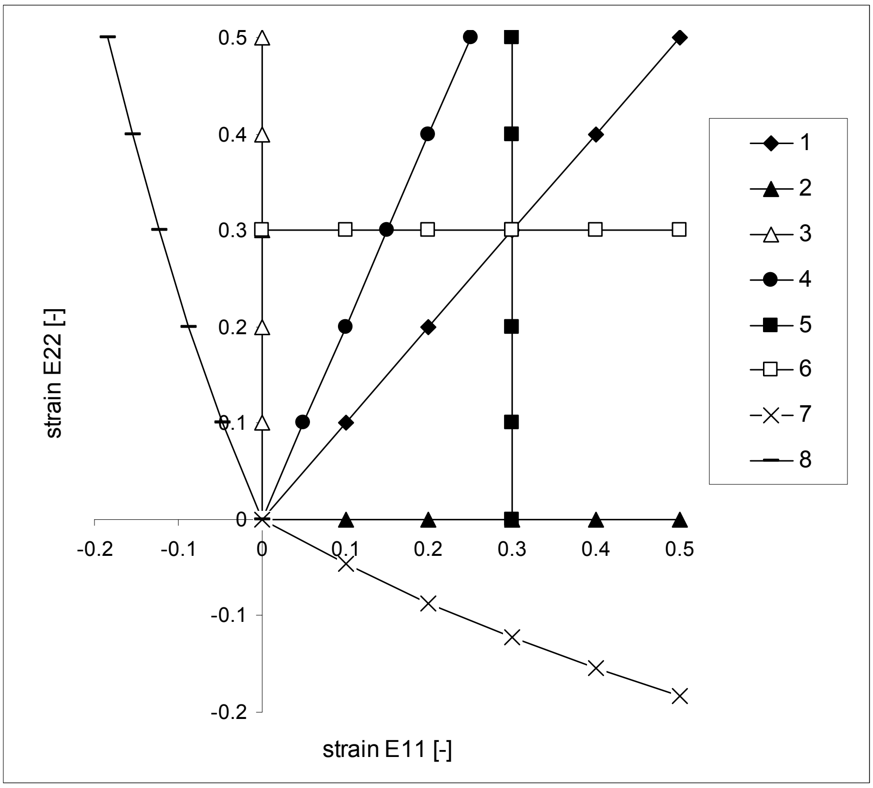

Figure 3-2 Representation of strains in the basic types of tests

3.1.3 Specimen preparation

Mechanical tests of soft tissues are realized „in vitro“using square or rectangular specimens. The specimens were cut-out from porcine thoracic aortas between aortic arc and renal arteries. Porcine thoracic aorta was chosen for its simple availability and similarity to human aortic tissue. Every edge of the specimen must be clamped by two or four clips to achieve a uniform distribution of load along the specimen width. Plastic templates are used for keeping the defined spacing distance between opposite and neighbouring clips (Figure 3-3). The clips must ensure holding of the specimen without its damage, therefore the torque used for tightening of the clip screws should be controlled. The disadvantage of the described clamping method is impossibility of ultimate tensile stresses measurement at specimens because the clips cause a stress concentration around clips especially in the specimen corners (see chapter 3.2). The tissue thickness was measured manually in three different locations and an average value was calculated and used for evalutation. The reference markers - four black points were drawn on the specimen surface with alcohol-based permanent ink [1] or 1mm diameter steel balls were glued onto the specimen surface [18], [19]. Then the specimen was immersed into the physiological saline solution (0.9% NaCl) with controlled temperature (Figure 3-4). Preload of the specimens was realized by a maximum total load of 0.5N; after preloading the specimen was loaded by a constant strain rate. During the test, positions of reference points were recorded by the CCD camera (together with the measured force values) and the data were used for further processing by special authorized software Tibixus, making the off-line image analysis. The influence of several factors was tested in the experiments and presented in the chapter 3.3.

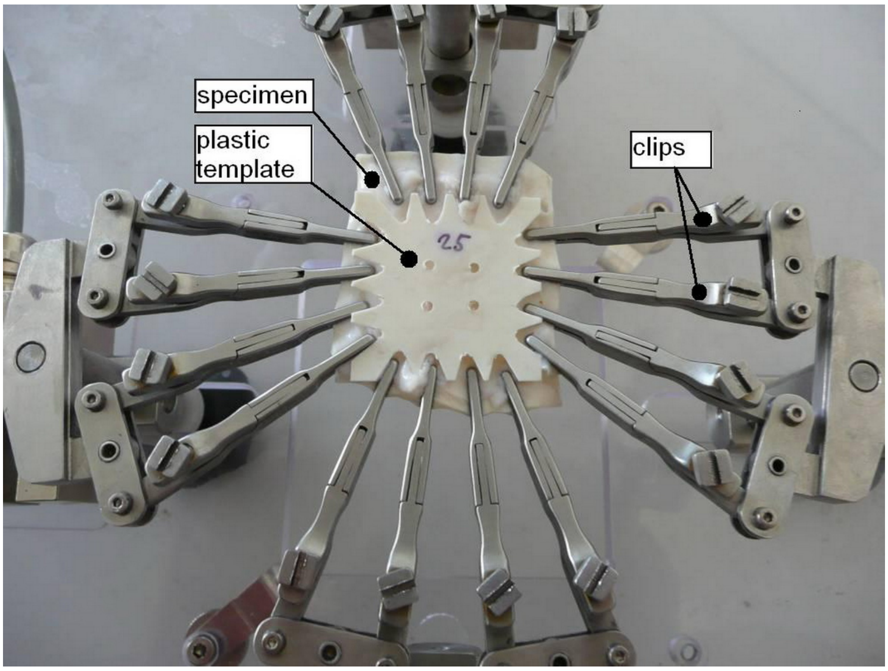

Figure 3-3 Clamping of specimen using a plastic template

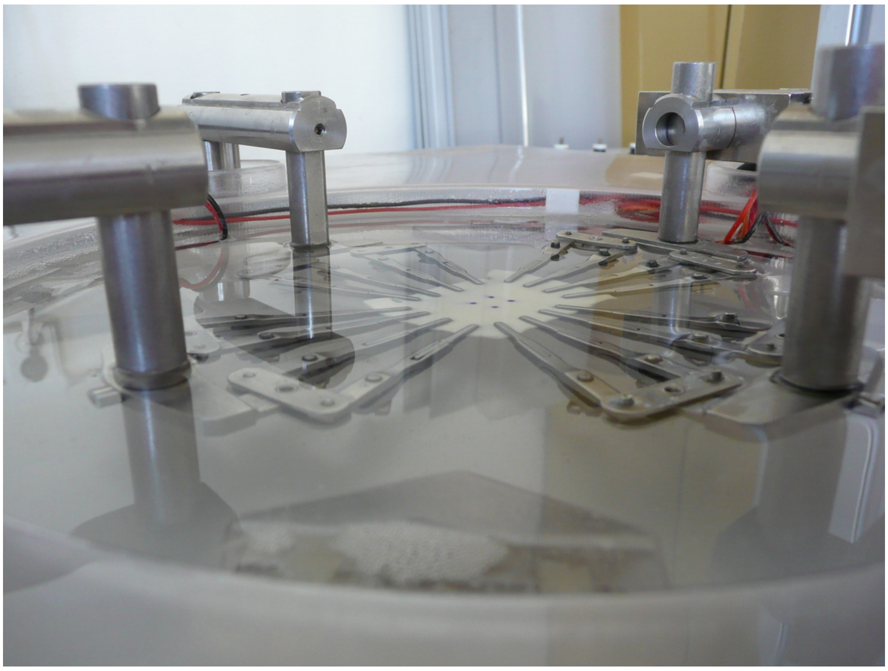
Figure 3-4 Specimen immersed in physiological saline solution

3.2 Ultimate tensile stress measurement

As mentioned in chapter 3.1.3 the way of specimen clamping causes the stress concentration around the clips. Therefore failure of the specimens occurs at these locations. This fact causes limitation of the load. The range of maximum load (stretch ratio vs. cauchy stress graphs) before specimen failure is shown on Figure 3-5 and Figure 3-7. The specimen failures during planar and equibiaxial tests are shown on Figure 3-6 and Figure 3-8. The experimentally estimated ultimate stress measured by pressure-imposed test [47] of porcine thoracic aortas is 1.8±0.4Mpa (mean±SD) for the specimen proximal to the heart and 2.3±0.8Mpa for the distal specimens. Comparing the ultimate stresses measured in the longitudinal (axial) tensile test [47] are 1.5±0.5Mpa for proximal and 2.0±0.7Mpa for distal specimen. Significant differencies were found between the pressure-imposed test results and the circumferential tensile test results where the ultimate stresses are 4.0±0.7Mpa for proximal and 3.3±0.6Mpa for distal specimen.

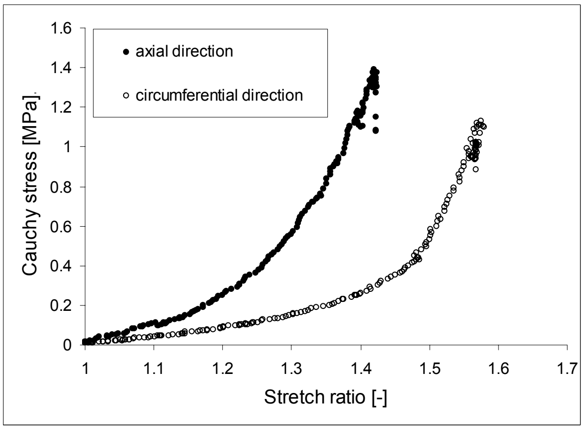

Figure 3-5 Planar tension tests (3.1.2) - graph

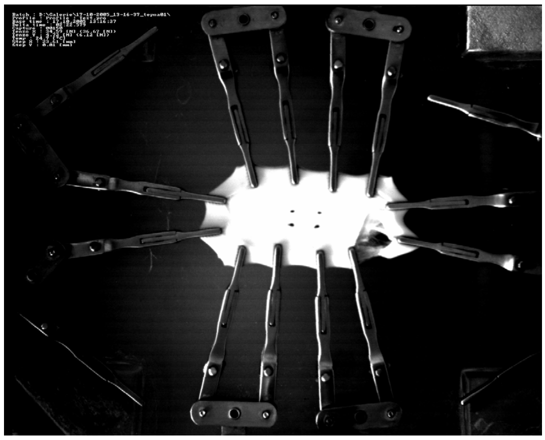

Figure 3-6 Planar tension test

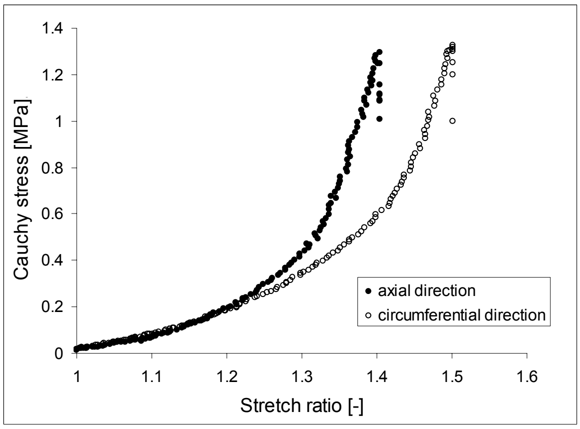

Figure 3-7 Equibiaxial tension test (3.1.2) - graph

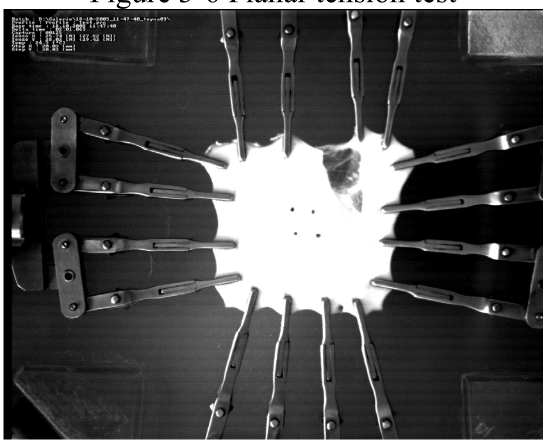

Figure 3-8 Equibiaxial tension test

3.3 Artery wall bahavior of non-separated artery

The result of the equibiaxial test of the non-separated artery wall of the thoracic aorta is shown on Figure 3-9. The non-separated artery walls were used for the experiments because anatomical instruments for layer-separation was not available. The typical layer separation [11] is shown on Figure 3-10. The results show that the artery wall is stiffer in circumferential direction at lower strains and stiffer in axial direction at higher strains. The observed developing of artery stiffness during deformation is consequence of different angle of families of fibres at the individual artery layer. The fibres have a characteristic waviness in the undeformed configuration whereas stiffening during deformation has been attributed to the straightening of the aortic lamellae and the increasing dispersion and allignment of collagen fibres [49] and [55]. This phenomena has also been reported in [51], [53], [54].

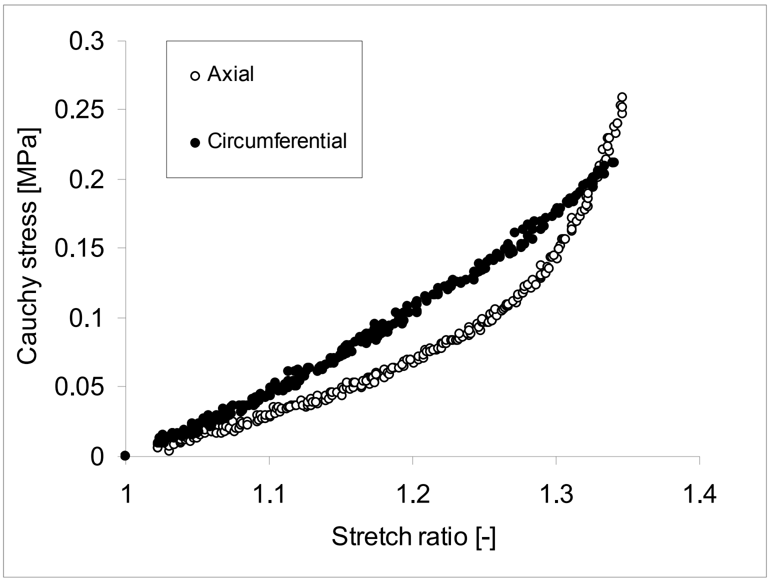

Figure 3-9 Equibiaxial stress-strain response for non-separated artery wall

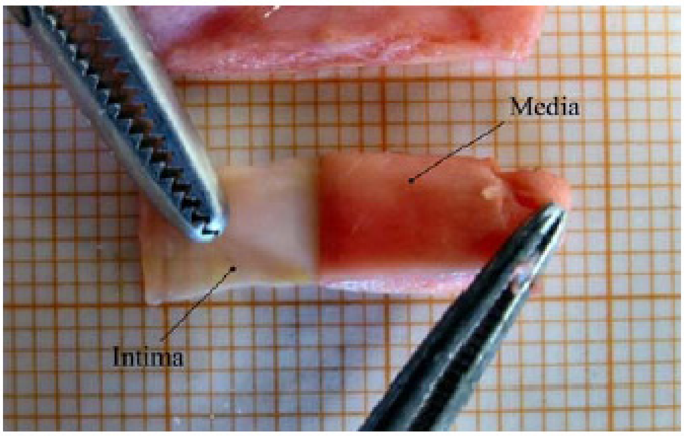

Figure 3-10 Layer separation of an aortic patch using standard anatomical instruments [11]

3.4 Experimental results of testing under influence of various factors

The source data have been published in author´s publications (I, II, IV).

3.4.1 Influence of temperature changes

Specimens were tested at temperatures 30°C and 37°C after having balanced their temperature for several minutes in the physiological saline solution. Temperature increase by 1°C results in a stiffness decrease of ~5% (Figure 3-11); this corresponds to values in literature [1]. The standard temperature of 37°C is generally used in mechanical testing of arteries ([2], [9]) as well as in all the following tests.

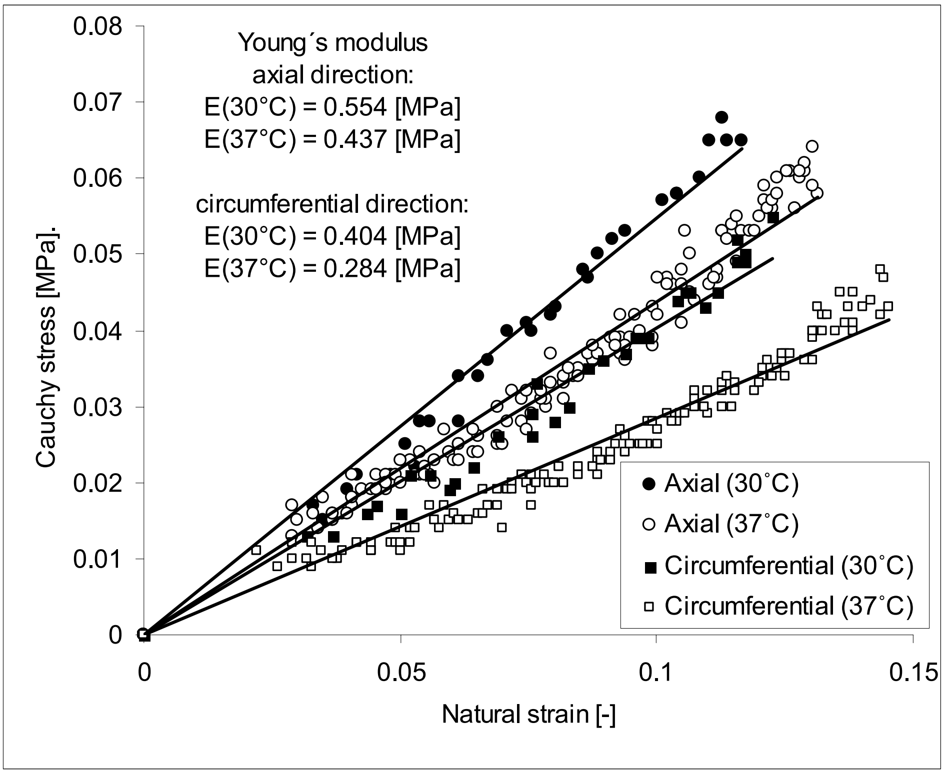

Figure 3-11 Equibiaxial stress-strain responses for different temperatures

3.4.2 Influence of specimen conservation

Arterial specimens are commonly preserved using refrigeration and freezing. Rare studies examined the effect of freezing and some of them (for example [14]-[17]) presented ambiguous results. To test the influence of the freezing process, fresh specimens of arterial wall were tested within 2 hours from excision (ectomy) and then refrigerated at -20°C and tested overnight again under the same conditions. We concluded that specimens after refrigeration and thawing have shown no significant changes in mechanical properties compared with the fresh ones (Figure 3-12). The maximum relative stress differences are 5% and 7.5% for axial and circumferential directions, respectively. The influence of longer refrigeration of specimens (in weeks or months) was not tested.

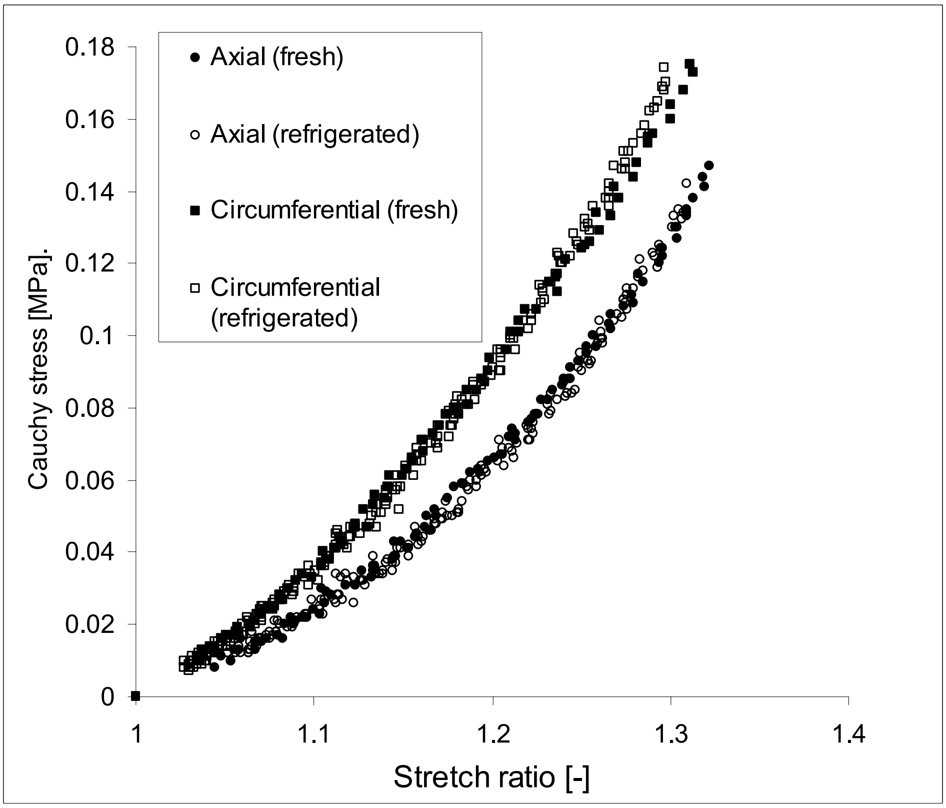

Figure 3-12 Equibiaxial stress-strain responses for fresh and refrigerated specimen

3.4.3 Influence of loading rate

Generally the tension response of soft tissues depends on the strain rate. Most soft tissues, among others arterial wall as well, appear to behave nearly incompressibly and in a markedly viscoelastic manner [1]. The physiological strain rate of healthy aortic wall is about $1s^{-1}$ (in the systolic phase of the cardiac cycle). This value depends on the artery location, age, artery and heart disease etc. Our rig enables us testing at strain rates from $0.004s^{-1}$ up to $0.100s^{-1}$ only. The stress-stretch responses in this strain rate range are shown in Figure 3-13. The specimens have been analyzed from a statistical point of view. Calculated stress standard deviations are in the range from 4.3% up to 6.4% of the average stress values (Figure 3-14).

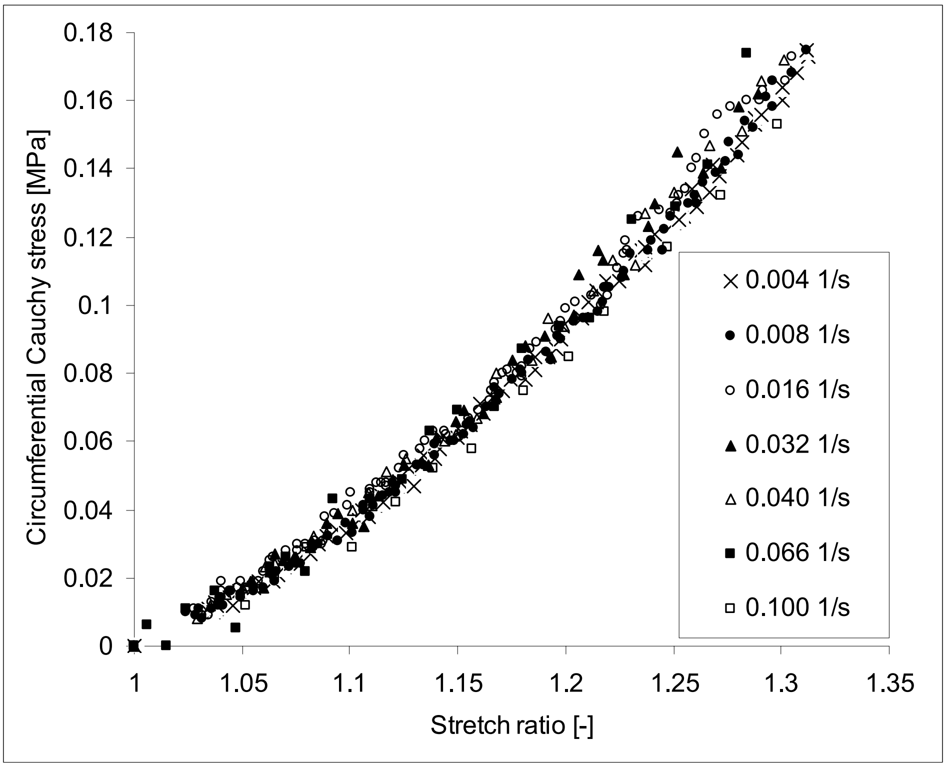

Figure 3-13 Equibiaxial stress-stretch responses for different loading rates

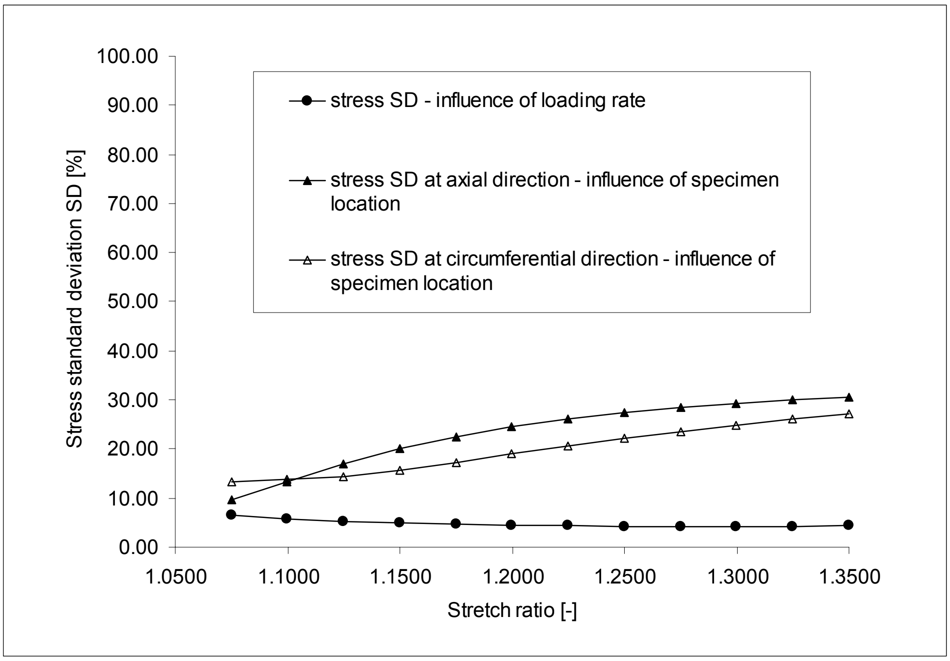

Figure 3-14 Standard deviations [%] in stresses as function of stretch ratio [-]

3.4.4 Influence of specimen location

The influence of specimen location was also tested experimentally. It was possible to obtain only three or four specimens (approximatelly 40 x 40mm) from one thoracic aorta and only one at each axial location; the difference in axial location of the neighbouring specimens was about 50mm. The stress-stretch responses of four specimens in various axial locations are shown in Figure 3-15 and Figure 3-16. It is evident that, in addition to the thickness, the stiffness has also changed significantly between the specimens of the same aorta; therefore the evaluation of material parameters is valid only for the particular axial location. The stress standard deviations over all measurements are 10% up to 30% of the average stress values (Figure 3-14). However, it is necessary to carry out three types of tests of each specimen (equibiaxial and planar tension tests in either „1"or „2" principal directions) for identification of material parameters of constitutive equations describing biaxial behavior of the specimen. Therefore it is not possible to test the specimen over the full physiological range of loading because tearing could begin. Impossibility of getting more specimens from the same location represents a limitation in evaluation of biaxial tension tests and in identification of material parameters of constitutive models.

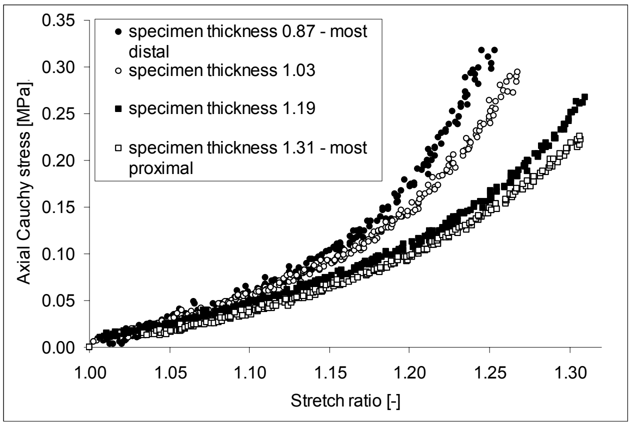

Figure 3-15 Equibiaxial stress-stretch responses in various location along the thoracic aorta – axial Cauchy stress [MPa]

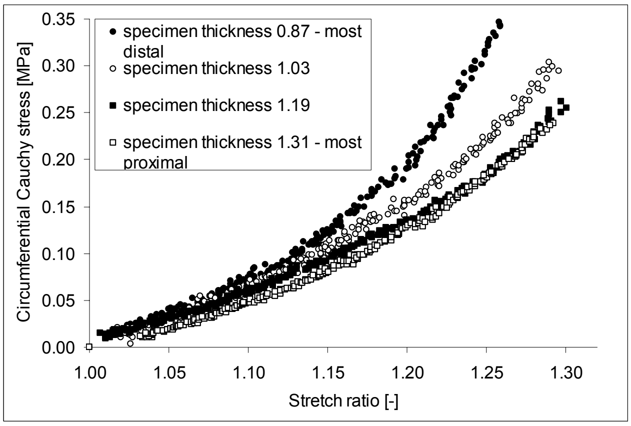

Figure 3-16 Equibiaxial stress-stretch responses in various location along the thoracic aorta – circumferential Cauchy stress [MPa]

3.4.5 Influence of preconditioning

Cyclic stress response during tension testing has been described in a number of biomechanical books and journals (e.g. [1], [2], [10] - [13]). Typically the specimens had been subjected to loading and unloading cycles in uniaxial tension until the stress softening effect diminished and the material exhibited a nearly repeatable cyclic behavior. The material is then said to be „preconditioned". An arterial wall consists of three major layers: the innermost intima, the media and the outermost adventitia. The adventitia consists of fibrous components (collagen and elastin fibres) and a non-fibrous matrix. The results published in [12] show a direct relation between changes in orientation and extension of the collagen fibres under load. The number of the necessary preconditioning cycles during uniaxial tensile tests depends on the origin of the specimen (species, localization, age, type of artery, etc.). In our experiments, the influence of preconditioning of specimens was tested not only in uniaxial (Figure 3-19) but in equibiaxial (Figure 3-17) and planar (Figure 3-18) tension tests.

The results of the preconditioning tests are summarized in Tab. 1. We can conclude that the effect of preconditioning is negligible up to stretch ratio λ=1.35 for equibiaxial tension test. (Higher stretch values have not been tested because of the risk of rupture in the vicinity of clamps – the highest stress concentration occurs in the corner of the specimen between the neighbouring clamps moving in perpendicular directions.) No significant changes in stress-strain relations occurred during the first six cycles (Figure 3-17). The maximal relative stress differences between the 1st and 2nd cycles are 4.8% and 3.0% for axial and circumferential directions, respectively. The maximal relative stress differences between the 1st and 6th cycles are 9.2% and 6.2% for axial and circumferential directions, respectively. On the contrary, the data obtained in the planar and uniaxial tension tests (Figure 3-18, Figure 3-19) show a more pronounced shift of loading curves among the first several cycles. Significant differences were found between the 1st and 2nd cycles. In axial direction, the maximal relative stress differences are 24.0% and 69.5% in planar and uniaxial tension tests, respectively. Contrary to the first two cycles, the maximal relative stress differences between 5th and 6th cycles are 4.7% and 3.5% in planar and uniaxial tension tests, respectively. As these differences lie below the expected dispersion of results, six cycles were chosen as sufficient for preconditioning. In circumferential direction the influence of preconditioning is a rather lower probably as consequence of the preferably circumferential orientation of reinforcing fibres.

It can be concluded that changes in material behaviour during preconditioning are related to the pronounced alignment of the collagen fibres towards the applied force [12]. Therefore it appears realistic that no changes connected with preconditioning occur in equibiaxial tension Figure 3-17 where no preferential direction of the applied load exists.

Tab. 1 Summary of stress differences between individual preconditioning cycles.

	stress differences [%] in the physiological range of loading					
	equibiaxial tension test		planar tension test		uniaxial tension test	
	axial direction	circ. direction	axial direction	circ. direction	axial direction	circ. direction
cycle 1 - 6	9.0 – 9.2	5.1 – 6.2	25.6 – 63.2	7.0 – 6.8	17.4 – 80.3	5.0 – 17.0
cycle 1 - 2	3.7 – 4.8	2.9 – 3.0	16.7 – 24.0	5.6 – 2.4	15.7 – 69.5	5.0 – 13.3
cycle 5 - 6	3.8 – 1.7	2.0 – 2.8	5.1 – 4.7	4.2 – 0.6	2.9 – 3.5	0.0 – 3.3

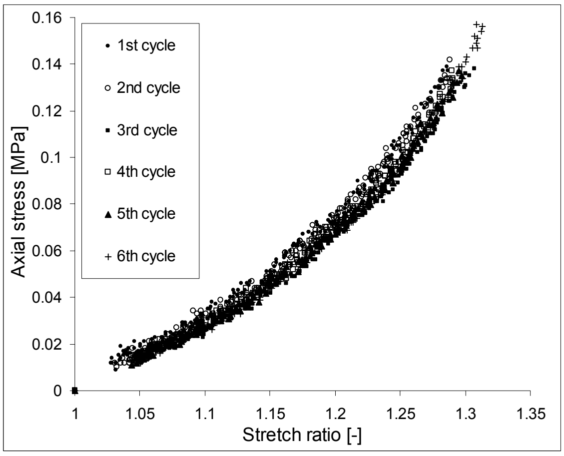

A) axial direction B) circumferential direction

Figure 3-17 Cyclic stress-stretch responses in equibiaxial tension tests

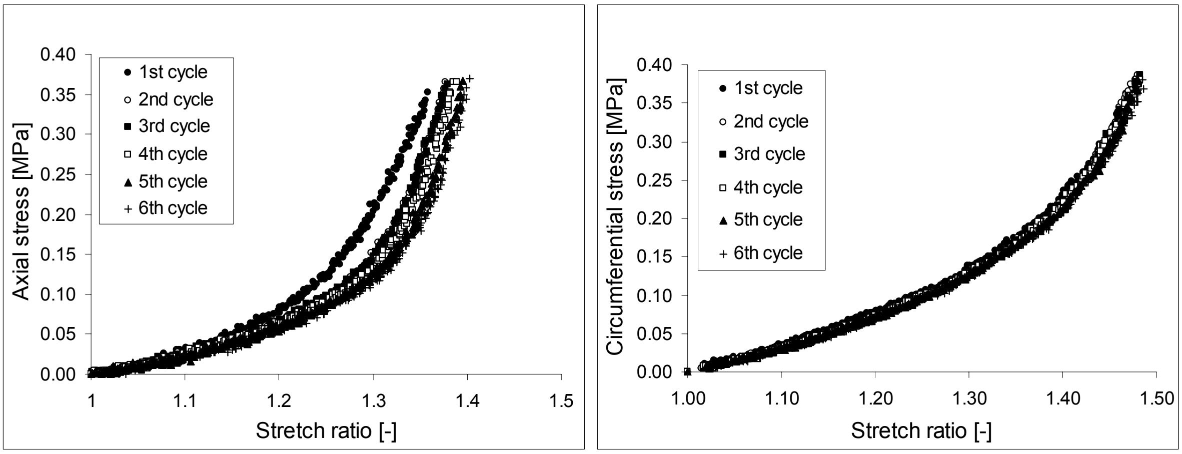

A) axial direction B) circumferential direction

Figure 3-18 Cyclic stress-stretch responses in planar tension tests

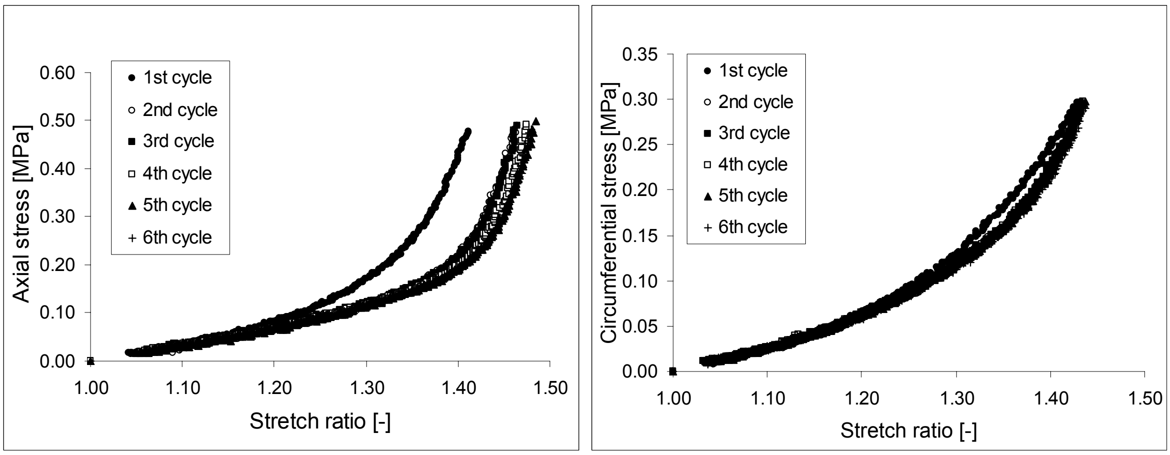

A) axial direction B) circumferential direction

Figure 3-19 Cyclic stress-stretch responses in uniaxial tension tests

4 CONSTITUTIVE MODELS OF THE ARTERIAL WALL

4.1 Constitutive relations

Appropriate constitutive relations are needed for computational modeling of stress-strain states in arteries. Because of large strain of arterial tissue and its pseudoelastic behavior, hyperelastic constitutive models are preferably used. Hyperelastic constitutive relations, isotropic as well as anisotropic, represent a mathematical description of relations among stress and strain components that are derived from strain energy density function *W*. If such a strain-energy function exists, the stress components can be obtained as derivatives of *W* with respect to the correspnding strain components:

$$S_{11} = \frac{\partial W}{\partial E_{11}} \qquad S_{22} = \frac{\partial W}{\partial E_{22}} \tag{4-1}$$

where S_{ij} is 2. Piola Kirchhoff stress tensor which is conjugated with Green Lagrange strain tensor E_{ij}. Let us consider a rectangular specimen as shown in Figure 4-1, then it is possible to define the components of stress tensor by several relations [1] presented in equations (4-2), (4-3) and (4-4):

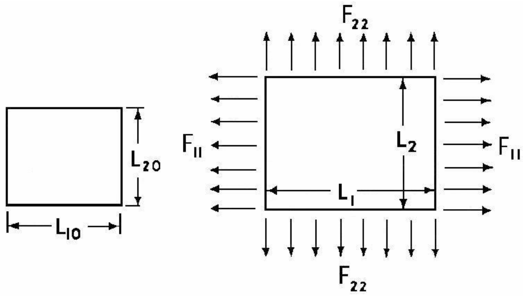

Figure 4-1 Geometry and deformation state of the specimen

$$\sigma_{11} = \frac{F_{11}}{L_2 \cdot h} \qquad \sigma_{22} = \frac{F_{22}}{L_1 \cdot h} \qquad \textit{Cauchy and Euler (true stress)} \tag{4-2}$$

$$T_{11} = \frac{F_{11}}{L_{20} \cdot h_0} \qquad T_{22} = \frac{F_{22}}{L_{10} \cdot h_0} \qquad \textit{Piola and Lagrange} \quad (1.P.K.) \quad (\textit{engineering stress}) \tag{4-3}$$

$$\left.\begin{aligned} S_{11} &= \frac{1}{\lambda_1} \cdot T_{11} = \frac{1}{\lambda_1^2} \cdot \sigma_{11} \\ S_{22} &= \frac{1}{\lambda_2} \cdot T_{22} = \frac{1}{\lambda_2^2} \cdot \sigma_{22} \end{aligned}\right\} \qquad \textit{Kirchhoff} \quad (2.P.K.) \tag{4-4}$$

where F_{11}, F_{22} are two pairs of forces acting on the edges of the specimen, L_{10}, L_{20}, h_0 are the original dimensions of specimen at the zero stress state L_1, L_2, h are the deformed dimensions of specimen, the ratios λ_1 and λ_2 are the principal stretch ratios:

$$\lambda_1 = \frac{L_1}{L_{10}},\ \lambda_2 = \frac{L_2}{L_{20}} \tag{4-5}$$

Rem. *Incompressible material (where relation* $\lambda_1\lambda_2\lambda_3=1$ *is valid) is a presumption for equation (4-4).*

The corresponding components (principal components) of strain tensors can be defined by the following relations [1]:

$$E_1 = \frac{1}{2}\cdot\left(\lambda_1^2 - 1\right) \qquad E_2 = \frac{1}{2}\cdot\left(\lambda_2^2 - 1\right) \qquad \textit{Green and St.Venant} \quad (\textit{Lagrange}) \tag{4-6}$$

$$\mathrm{E}_1 = \frac{1}{2}\cdot\left(1 - \frac{1}{\lambda_1^2}\right) \qquad \mathrm{E}_2 = \frac{1}{2}\cdot\left(1 - \frac{1}{\lambda_2^2}\right) \qquad \textit{Almansi and Hamel} \quad (\textit{Euler}) \tag{4-7}$$

$$e_1 = \ln\lambda_1 \qquad e_2 = \ln\lambda_2 \qquad \textit{Logarithmic} \ (\textit{natural}) \ \textit{strain} \tag{4-8}$$

Only pairs of mutually conjugated stress and strain tensors give the strain energy density. For example:

Cauchy stress tensor is conjugated with logarithmic strain tensor because both of these tensors are related to the actual dimensions.

Kirchhoff stress tensor (2.P.K) is conjugated with Green (Lagrange) strain tensor.

4.2 Overview of frequent types of strain energy density functions

For an identification of parameters from experimental data a selection of a convenient constitutive model is necessary. These models can be either phenomenological or structural i.e. based on some information on the tissue structure (histology). Strain energy function defined per unit reference volume is assumed in the shape (4-9) where J is the volume ratio, i.e., the determinant of the deformation gradient **F** [4] which is a primary measure of deformation. Since most of the soft biological tissues behave like incompressible materials (J=1, no change in volume during deformation), U is treated as a (purely mathematically motivated) penalty function enforcing the incompressibility constraint.

$$W = \overline{W} + U(J) \tag{4-9}$$

The most frequent phenomenological constitutive models used in AAA models are defined on the base of the following strain energy density functions:

4.2.1 Isotropic polynomial model [63]:

The isotropic polynomial model (Yeoh model) is a special (reduced) shape of the Mooney-Rivlin model and is used for abdominal aortic aneurysms in several studies e.g. [27], [42] and [43]. The model used specifically for AAA is specified by the following energy function:

$$W = a\left(\overline{I}_1 - 3\right) + b\left(\overline{I}_1 - 3\right)^2 + U(J) \tag{4-10}$$

where a, b are material parameters. This constitutive model is implemented in ANSYS.

4.2.2 Isotropic exponential model

The isotropic exponential strain energy function was proposed by Blatr, Demiray and Delfino et al. [24], [25] and [26]:

$$W = \frac{a}{b}\left(e^{\frac{b}{2}(\overline{I}_1 - 3)} - 1\right) + \frac{1}{d}\ln^2 J \tag{4-11}$$

where $a > 0$ is a stress-like material parameter, $b > 0$ is a non-dimensional paremeter, d is a compressibility parameter.

4.2.3 Polynomial model proposed by Patel and Vaishnav et al. [21]:

$$W = AE_{11}^2 + BE_{11}E_{22} + CE_{22}^2 + DE_{11}^3 + EE_{11}^2E_{22} + GE_{11}E_{22}^2 + HE_{22}^3 \tag{4-12}$$

where A, B, C, D, E, G, H are stress-like material parameters and E_{ij} are components of Green-Langrange strain tensor.

4.2.4 Exponential model proposed by Fung et al. [1]:

$$W = \frac{c}{2}\left[\left(\exp Q\right) - 1\right] \tag{4-13}$$

$$\textit{where} \quad Q = b_1E_{\Theta\Theta}^2 + b_2E_{ZZ}^2 + b_3E_{RR}^2 + 2b_4E_{\Theta\Theta}E_{ZZ} + 2b_5E_{ZZ}E_{RR} + 2b_6E_{RR}E_{\Theta\Theta} + b_7E_{\Theta Z}^2 + b_8E_{RZ}^2 + b_9E_{R\Theta}^2$$

where c is a stress-like material parameter, b_i, $i=1,\dots,9$ are non-dimensional material parameters and E_{ij} are components of Green-Langrange strain tensor referred to cylindrical polar coordinates ($R\theta Z$).

Rem: *The physical meanings of the individual parameters are unclear therefore it is important to be sure that the optimization process is performed within a range of parameters for which convexity of the strain energy function is assured* [8].

The alternative potential $\overline{W}(E_{\theta\theta}, E_{ZZ})$ known as “two-dimensional counterpart” of W is very popular and used in the literature [8]. Two-dimensional formulation is not capable of describing the three-dimensional anisotropic behavior of the material but for a special case of loading the $\overline{W}$ can be suitable for predicting the three-dimensional state of stress. Considering incompressible material deformed in biaxial tension test ($E_{\theta Z}=E_{RZ}=E_{R\theta}=0$) the E_{RR} is computed from $E_{\theta\theta}$ and E_{ZZ}:

$$E_{RR} = \frac{1}{2(2E_{ZZ}+1)(2E_{\Theta\Theta}+1)} - \frac{1}{2} \tag{4-14}$$

Using these assumptions an alternative two-dimensional approximation of W may be given in the form:

$$W(E_{RR}, E_{\Theta\Theta}, E_{ZZ}, E_{R\Theta}, E_{RZ}, E_{\Theta Z}) = \overline{W}(E_{ZZ}, E_{\Theta\Theta}) \tag{4-15}$$

Using the chain rule, the derivatives:

$$\frac{\partial \overline{W}}{\partial E_{\alpha}} = \frac{\partial W}{\partial E_{\alpha}} + \frac{\partial W}{\partial E_{RR}} \frac{\partial E_{RR}}{\partial E_{\alpha}} \qquad (\alpha = ZZ, \Theta\Theta) \tag{4-16}$$

The stresses are:

$$S_{ZZ} = \frac{\partial \overline{W}}{\partial E_{ZZ}}, \quad S_{\Theta\Theta} = \frac{\partial \overline{W}}{\partial E_{\Theta\Theta}}, \quad S_{RR} = 0 \tag{4-17}$$

4.2.5 Logarithmic 2D model proposed by Takamizawa and Hayashi [22], [23]:

$$W = -c \ln\left(1 - Q\right) \tag{4-18}$$

$$\textit{where} \quad Q = \frac{1}{2}c_1 E_{11}^2 + \frac{1}{2}c_2 E_{22}^2 + c_3 E_{11} E_{22}$$

where c is a stress-like material parameter, c_1, c_2, c_3 are non-dimensional material parameters and E_{ij} are components of Green-Langrange strain tensor.

Rem: *The logarithmic model is limited by maximum strain values on the order of* 10^{-1} *(the tissue-specific range depends on its value of material parameters); for excessive strains the value of Q extends beyond* 1 *and* ln(1-Q) *in not defined.*

4.2.6 A single-layer anisotropic exponential model:

A single-layer exponential model was proposed by Spencer [6] and particulated by Hozapfel et al. [8]. This model is based on some histological information on (collagen) reinforcing fibres in the individual arterial layers which must be dissected before experimental testing. The strain energy density formula consists of an isotropic part $\overline{W}_{iso}$ and an anisotropic part $\overline{W}_{aniso}$. The isotropic part is expressed in the Neo-Hookean form [63], while the anisotropic part is described by an exponential function. The volumetric elastic response U is given scalar-valued objective function of J. The isotropic part of the strain energy density represents the matrix properties of the material whereas the anisotropic part is related to the two families of collagen fibers, i.e.:

$$W_{\left(\bar{I}_1, \bar{I}_4, \bar{I}_6, J\right)} = \overline{W}_{iso\left(\bar{I}_1\right)} + U(J) + \overline{W}_{aniso\left(\bar{I}_4, \bar{I}_6\right)} \tag{4-19}$$

$$\overline{W}_{iso(\overline{I}_1)} = \frac{c}{2}\left(\overline{I}_1 - 3\right) \tag{4-20}$$

$$U(J) = \frac{1}{d}\left(J-1\right)^2 \tag{4-21}$$

$$\overline{W}_{aniso(\overline{I}_4,\overline{I}_6)} = \frac{k_1}{2k_2}\sum_{i=4,6}\left(e^{k_2\left(\overline{I}_i-1\right)^2}-1\right) \quad ..... \quad for \quad \overline{I}_4>1, \overline{I}_6>1 \tag{4-22}$$

$$\overline{W}_{aniso(\overline{I}_4,\overline{I}_6)} = \frac{k_1}{2k_2}\left(e^{k_2\left(\overline{I}_4-1\right)^2}-1\right) \quad ..... \quad for \quad \overline{I}_4>1, \overline{I}_6<1 \tag{4-23}$$

$$\overline{W}_{aniso(\overline{I}_4,\overline{I}_6)} = \frac{k_1}{2k_2}\left(e^{k_2\left(\overline{I}_6-1\right)^2}-1\right) \quad ..... \quad for \quad \overline{I}_4<1, \overline{I}_6>1 \tag{4-24}$$

$$\overline{W}_{aniso(\overline{I}_4,\overline{I}_6)} = 0 \quad ..... \quad for \quad \overline{I}_4<1, \overline{I}_6<1 \tag{4-25}$$

where: c, k_1 are stress-like material parameters

k_2 is a non-dimensional material parameter

d is a compressibility parameter

$\overline{I}_1, \overline{I}_4, \overline{I}_6$ are reduced invariants of right Cauchy-Green def. tensor [5]:

$$\overline{I}_1 = \lambda_1^2 + \lambda_2^2 + 1/(\lambda_1^2\lambda_2^2) \tag{4-26}$$

$$\overline{I}_4 = \overline{I}_6 = \lambda_1^2\cos^2\varphi_1 + \lambda_2^2\sin^2\varphi_1 \tag{4-27}$$

where φ_1 are angle of reinforcing fibres in Cartesian coordinate system

J=det(F), where F is deformation gradient

4.2.7 A double-layer anisotropic exponential model

A single-layer exponential model described above requires dissection of individual artery layers. Considering single-layer exponential model for description of the whole artery wall the observed changes in specimen stiffnes during deformation cannot be satisfactorily described. A double-layer constitutive model derived from the single-layer constitutive model has been performed at authors´site [61]. For description of the homogenized response of the double-layer model the following constitutive relation can be written:

$$W_{\left(\overline{I}_1,\overline{I}_4^A,\overline{I}_6^A,\overline{I}_4^B,\overline{I}_6^B\right)} = f^A W_{\left(\overline{I}_1,\overline{I}_4^A,\overline{I}_6^A\right)} + f^B W_{\left(\overline{I}_1,\overline{I}_4^B,\overline{I}_6^B\right)} + U(J) = \overline{W}_{iso(I_1)} + \sum_{j=A,B}\overline{W}_{aniso(I_4^j,I_6^j)} + U(J) \tag{4-28}$$

where f^A and f^B are the volume fraction factors of each artery layer A and B (equal to thickness fractions) relative to artery wall. Isotropic part $\overline{W}_{iso}$ and volumetric elastic response U is the same as in the single-layer exponential model (chapter 4.2.6). Anisotropic part considering the volume fraction factors can be written:

$$\overline{W}_{aniso}{}^{A} = \frac{f^A k_1^A}{2k_2^A}\left[\left(e^{k_2^A(I_4^A-1)^2}-1\right)+\left(e^{k_2^A(I_6^A-1)^2}-1\right)\right] \tag{4-29}$$

$$\overline{W}_{aniso}{}^{B} = \frac{f^B k_1^B}{2k_2^B}\left[\left(e^{k_2^B(I_4^B-1)^2}-1\right)+\left(e^{k_2^B(I_6^B-1)^2}-1\right)\right] \tag{4-30}$$

4.2.8 Combination of polynomial and exponential model [48]:

The following exponential model described in [48] consists of the exponential models described above. The strain energy density function has a following form:

$$\overline{W} = c_1(\overline{I}_1-3)+c_2(\overline{I}_1-3)^2+D_1(e^{D_2(\overline{I}_i-3)}-1)+\frac{k_1}{2k_2}\sum_{i=4,6}\left(2e^{k_2(\overline{I}_i-1)^2}\right) \tag{4-31}$$

where c_1, c_2, D_1 and k_1 are stress-like material parameters, D_2 and k_2 are non-dimensional material parameters.

4.2.9 Anisotropic polynomial model [63]:

The anisotropic model (implemented in ANSYS) is described by the following polynomial strain energy density formula:

$$W = U(J)+\overline{W}_d\left(\overline{C},A,B\right) \tag{4-32}$$

where the deviatoric part W_d of the strain energy function can be used in the following form:

$$\begin{aligned}\overline{W}_d\left(\overline{C},A,B\right)=&\sum_{i=1}^{3}a_i\left(\overline{I_1}-3\right)^i+\sum_{j=1}^{3}b_j\left(\overline{I_2}-3\right)^j+\sum_{k=2}^{6}c_k\left(\overline{I_4}-1\right)^k+\\&+\sum_{l=2}^{6}d_l\left(\overline{I_5}-1\right)^l+\sum_{m=2}^{6}e_m\left(\overline{I_6}-1\right)^m+\sum_{n=2}^{6}f_n\left(\overline{I_7}-1\right)^n+\sum_{o=2}^{6}g_o\left(\overline{I_8}-\varphi\right)^o\end{aligned} \tag{4-33}$$

where a_i, b_j, c_k, d_l, e_m, f_n, g_o are material parameters and φ represents specific constant related to the directions of fibres.

4.3 Identification of parameters from experimental data

4.3.1 Non-linear least square fit for orthotropic hyperelastic material

Fitting of the constitutive model to experimental data is achieved by optimizing (minimizing) the stress-based nonlinear function [20]:

$$f_s = \sum_{i=1}^{n} \left[w_1 \left(\frac{\partial W}{\partial E_{11}} \Big|_i - S_{11}^i \right)^2 + w_2 \left(\frac{\partial W}{\partial E_{22}} \Big|_i - S_{22}^i \right)^2 \right] \tag{4-34}$$

where n is number of data records, w_1 and w_2 are weighting factors, and $\frac{\partial W}{\partial E_{11}}\Big|_i$ and $\frac{\partial W}{\partial E_{22}}\Big|_i$ are the 2. Piola Kirchhoff stresses predicted by the constitutive model for i-th data record.

The experimental 2. Piola Kirchhoff stresses S_{11}^i and S_{22}^i are calculated directly from the original data according Eq. 4.4.

Alternatively to the stress-based approach expressed by (4.25), an energy-based nonlinear function f_w may also be chosen [20]. Thus:

$$f_w = \sum_{i=1}^{n} \left(\psi_i - W_i \right)^2 \tag{4-35}$$

where n is number of data records, ψ_i is the strain energy for i-th data record predicted by the constitutive model and

$$\overline{W}_i = \int_0^{E_{11}^i} S_{11}^i dE_{11}^i + \int_0^{E_{22}^i} S_{22}^i dE_{22}^i \tag{4-36}$$

is the strain energy computed from experimental data. From a mathematical point of view both approaches are equivalent.

4.3.2 Example of determination of constitutive parameters

The source data have been published in author´s publications (V, VI, VII, VIII). The software STATISTICA 7.0 from StatSoft Inc. is used for determination of constitutive parameters. This software enables a nonlinear estimation using user-specified regression equation and custom loss function [64]. The general form for the desired regression model is with the dependent variable on the left side of the equation and expression including independent variable and the parameters to be estimated on the right side of the equation. The energy-based approach is used for determination of material parameters. The numerical integration is used for evaluation of strain-energy function from the experimental data (Eq. (4-37) and Eq. (4-38)):

$$\overline{W} = \sum_{i=1}^{n} \sum_{j=11}^{22} \frac{\sigma_j^i + \sigma_j^{i-1}}{2} \left(\ln \lambda_j^i - \ln \lambda_j^{i-1} \right) \quad \textit{for isotropic and Holzapfel model} \tag{4-37}$$

$$\overline{W} = \sum_{i=1}^{n} \sum_{j=11}^{22} \frac{S_j^i + S_j^{i-1}}{2} \left(E_j^i - E_j^{i-1} \right) \quad \textit{for Fung model} \tag{4-38}$$

where n is number of experimental data.

In this example the strain energy function W is computed from the experimental data obtained from three types of tests:

a) equibiaxial tension tests – equal strains in both loading directions (Figure 3-2)
b) planar tension tests – uniaxial extension in either „1“ or „2“ directions with the constrained (close to zero) transversal contraction (Figure 3-2)

The Cauchy stresses σ11 and σ22 for pure homogeneous planar biaxial deformation of a thin sheet are then obtained as in [8]:

$$\sigma_i = 2 \cdot \frac{\partial W}{\partial \lambda_i^2} \cdot \lambda_i^2 = \frac{\partial W}{\partial \lambda_i} \cdot \lambda_i \qquad (i = 11, 22) \textit{ for isotropic and Holzapfel model} \tag{4-39}$$

$$\sigma_i = \frac{\partial \overline{W}}{\partial E_i} \lambda_i^2 \qquad (i = 11, 22) \textit{ for Fung model} \tag{4-40}$$

Using the off-line image analysis software Tibixus, cauchy stress and principal stretch ratios in two orthogonal directions are obtained. For application of Fung model these data are then expressed as Kirchoff stresses (2.P.K.) Eq. (4-4) and Green-Lagrange strain Eq. (4-6). The parameters of constitutive models are then obtained by means of the standard nonlinear Levenberg-Marquardt algorithm (or Gauss-Newton algorithm) for multivariate nonlinear regression by minimizing the user specified function. For the single or double-layer model application it is necessary to define not only the estimated function but also least-squares loss function “L” including a penalty function (assessment) designed to “penalize” the parameters. For example, if two parameters (c and k_1) are to be constrained to be greater than zero then one must assess a large penalty to these parameters if these conditions are not met:

$$L = (observed - predicted)^2 + (c < 0) + (k_1 < 0) \tag{4-41}$$

The reason for the loss function definition is the physical meaning of parameters of constitutive model which does not have to be respected from a mathematical point of view. As mentioned in chapter 4.2.6, c and k_1 are stress-like material parameters therefore these parameters must be positive. The parameters of the constitutive model are then obtained by an appropriate algorithm (e.g. Quasi-

Newton, Simplex, Hooke-Jeeves pattern moves or Rosenbrock algorithm) for multivariate nonlinear regression. The resulting regression surface of the strain energy function is shown in Figure 4-2.

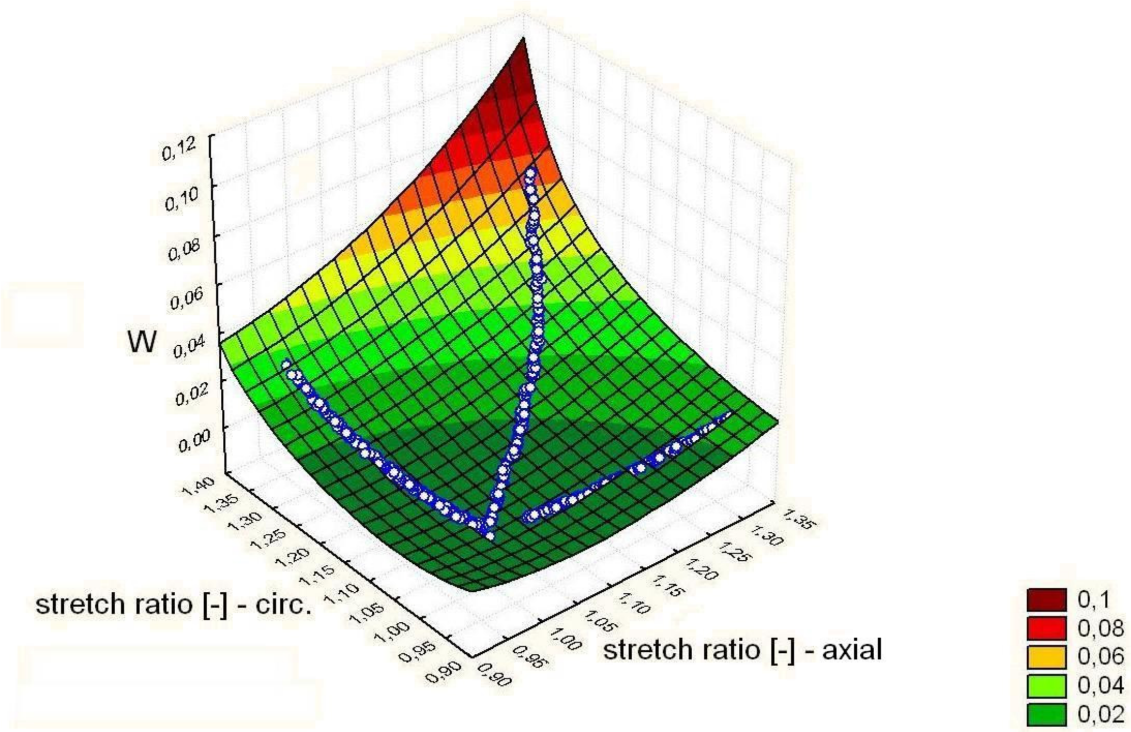

Figure 4-2 Regression surface of strain energy function

Comparisons between the experimental data and the evaluated data (Tab. 2) for exponential isotropic model (4.2.2), exponential anisotropic Fung´s type model (4.2.4) and single or double-layer anisotropic model (4.2.6) implemented in ANSYS at author´s site are shown on Figure 4-4 till Figure 4-15. Apparently the Holzapfel single-layer model was not able to approximate the curve of the whole arterial wall in the direction more distant from the supposed orientation of fibres. The numerical verification of the presented constitutive models is shown in chapter 5.2.

Tab. 2 Mean values of the evaluated material parameters

Model	a	b						
	[MPa]	[-]						
Isotropic (4.2.2)	0.090	1.700						
Model	c	b_1	b_2	b_3	b_4	b_5	b_6	
	[MPa]	[-]	[-]	[-]	[-]	[-]	[-]	
Fung (4.2.4)	34.663	0.0125	0.0101	0.0103	0.0071	0.0064	0.0067	
Model	c	k_{1A}	k_{2A}	φ_A	k_{1B}	k_{2B}	φ_B	$f^A=f^B$
	[MPa]	[MPa]	[-]	[deg]	[MPa]	[-]	[deg]	[-]
Single-layer (4.2.6)	0.073	0.020	2.213	58.3°				
Double-layer (4.2.7)	0.019	0.051	0.011	84.9°	0.080	1.015	36.9°	0.5

*note: lower and upper confidence limits of the evaluated material parameters are also computed but these limits are not applied in the FEA simulations described in chapter 5; therefore these limits are not shown.

**note: the angle of fibres φ is measured from axial to circumferential direction (Figure 4-3).

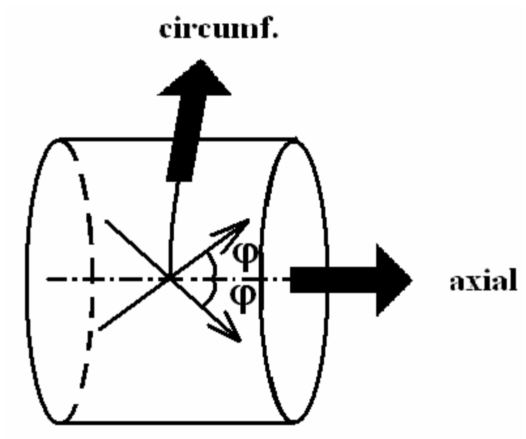

Figure 4-3 Angle of fibres

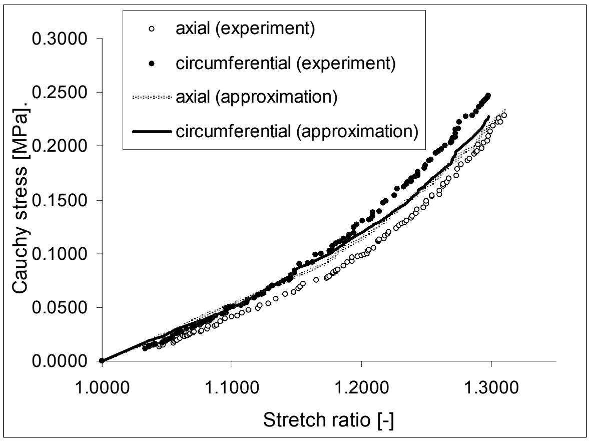

Figure 4-4 Stress-stretch responses in equibiaxial tension test – Isotropic exponential constitutive model (4.2.2)

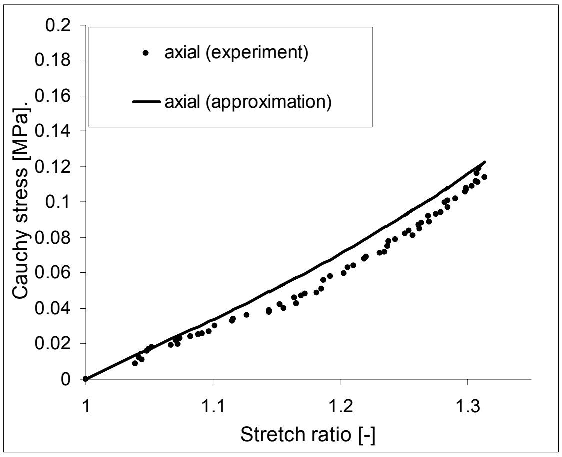

Figure 4-5 Stress-stretch Stress-stretch responses in planar tension test – axial direction test – Isotropic exponential constitutive model (4.2.2)

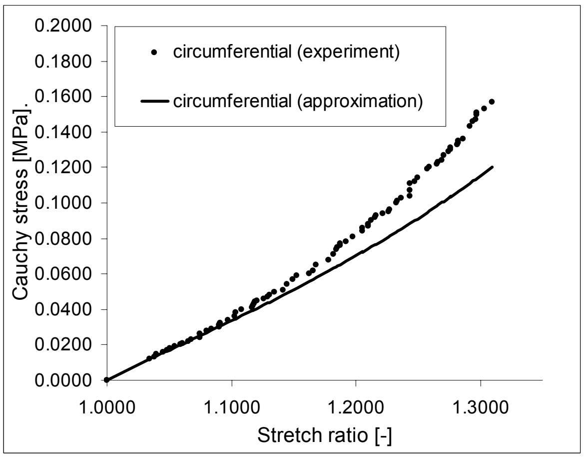

Figure 4-6 Stress-stretch responses in planar tension test – circumferential direction test – Isotropic exponential constitutive model (4.2.2)

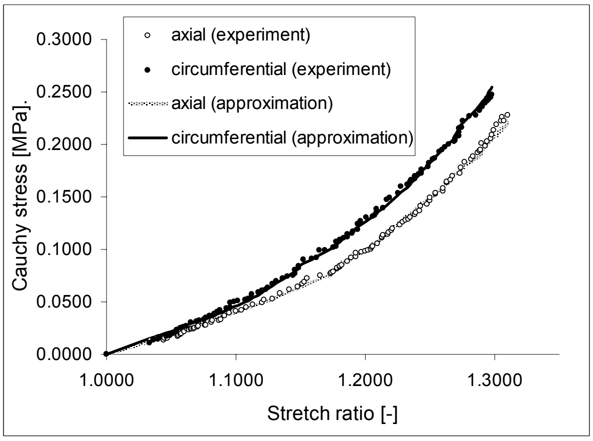

Figure 4-7 Stress-stretch responses in equibiaxial tension test – exponential constitutive model proposed by Fung (4.2.4)

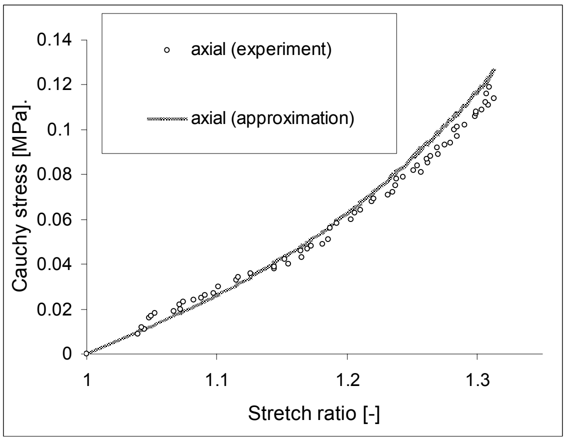

Figure 4-8 Stress-stretch responses in planar tension test – axial direction test – exponential constitutive model proposed by Fung (4.2.4)

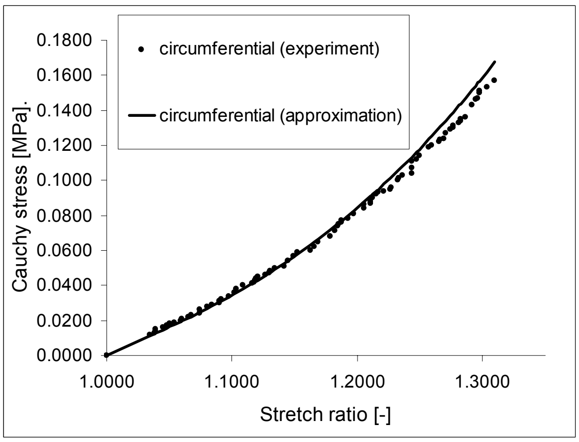

Figure 4-9 Stress-stretch responses in planar tension test – circumferential direction test – exponential constitutive model proposed by Fung (4.2.4)

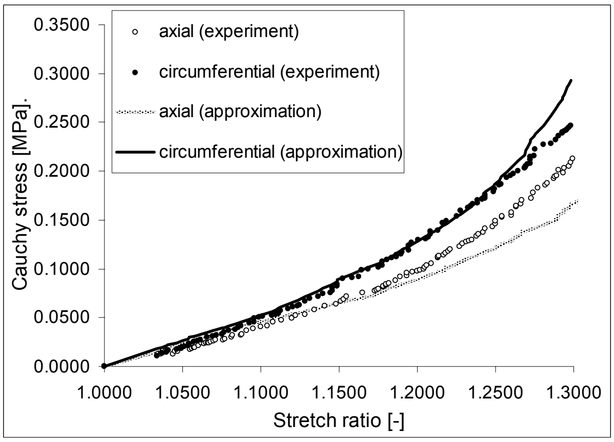

Figure 4-10 Stress-stretch responses in equibiaxial tension test – Holzapfel single-layer exponential constitutive model (4.2.6)

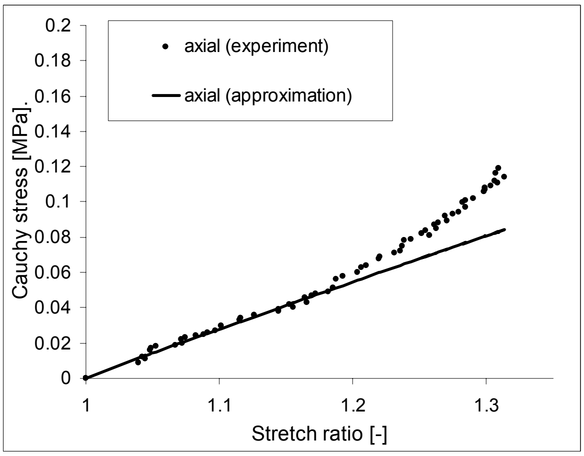

Figure 4-11 Stress-stretch responses in planar tension test – axial direction test – Holzapfel exponential single-layer constitutive model (4.2.6)

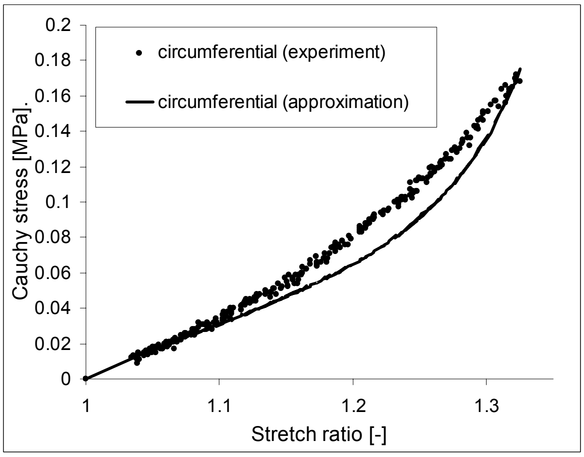

Figure 4-12 Stress-stretch responses in planar tension test – circumferential direction test – Holzapfel exponential single-layer constitutive model (4.2.6)

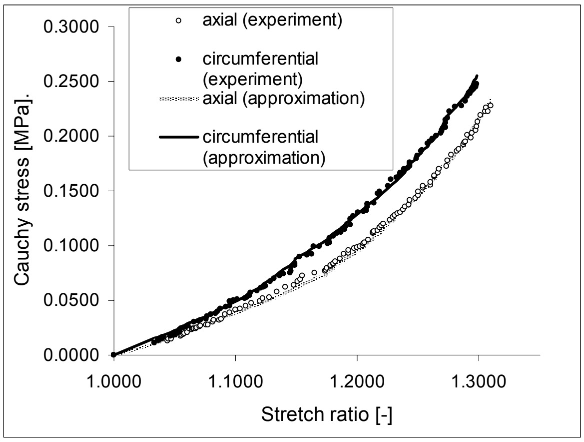

Figure 4-13 Stress-stretch responses in equibiaxial tension test – double-layer exponential constitutive model (4.2.7)

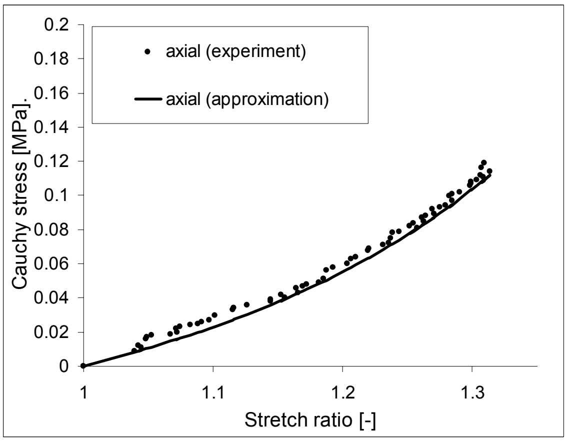

Figure 4-14 Stress-stretch responses in planar tension test – axial direction test – double-layer exponential constitutive model (4.2.7)

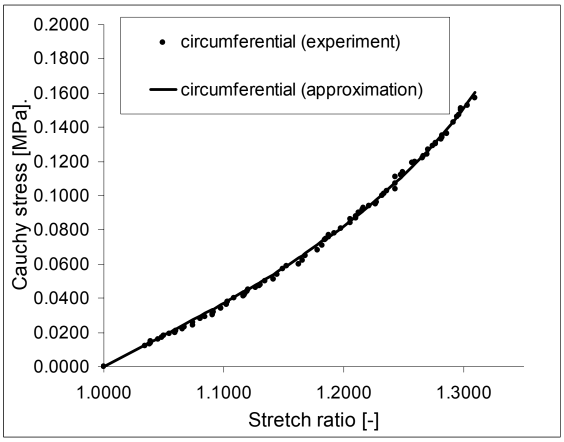

Figure 4-15 Stress-stretch responses in planar tension test – circumferential direction test – double-layer exponential constitutive model (4.2.7)

5 FINITE ELEMENT MODELING – FEA modeling

In this section the AAA FEA modeling is realized using isotropic exponential and the anisotropic exponential model described in chapter 4.2.1, 4.2.2 and 4.2.6. Exponential model proposed by Fung (4.2.4) was also implemented in ANSYS at authors´ site but convexity of the strain energy function is assured for a specific range of parameters [8]. This limitation is the main disadvantage of the model and the first reason why this model is not used in FEA AAA simulations. The second reason is absence of reliable material parameters used in recent literature for real AAA simulations.

5.1 General assumptions for FEA modeling

- Gravitation is negligible with respect to blood pressure.
- The shear stress caused by the blood flow is negligible [37].
- The effect on pressure in the wall from fluid flow turbulences are assumed insignificant [39].
- Initial stress (residual stress) is not taken in to account.
- The temperature changes of a human body are not taken in acount.
- The intra-luminal thrombus is not taken into account.
- The boundary conditions do not include the contact of the AAA with surroundings organs and the vertebral column, which may influence on the results. This assumption is similarly used in the studies [56], [57].
- The AAA wall is purely solid without any fluid component. It is assumed that AAA wall is incompressible.
- For all models the wall thickness is assumed to be uniform in axial and circumferential directions. This assumption has been used in a number of previous studies e.g. [27], [40], [43] and [45].

5.2 FEA simulated experiment

In this section the presented constitutive models 4.2.2, 4.2.4, 4.2.6 and 4.2.7 with the material parameters presented in Tab. 2 were evaluated analytically and verified numerically using ANSYS. The dimensions of the specimen were based on the real specimen dimensions (40×40×1.31mm) used in the experimental part of work.

5.2.1 Isotropic exponential model (4.2.2)

The material parameters used for the isotropic exponential model are recapitulated in Tab. 3:

Tab. 3 Isotropic exponential model - material parameters

Model	*a*	*b*	*d*
	[MPa]	[-]	[MPa]
Isotropic (4.2.2)	0.090	1.700	0

The analytical expression of axial „1" and circumferential „2" stress components for the isotropic exponential model (4.2.2) are obtained using equation (4-11) substituted into equation (4-39):

$$\sigma_1 = \lambda_1 \frac{1}{2} a \left(2\lambda_1 - \frac{2}{\lambda_1^3 \lambda_2^2} \right) e^{\left(\frac{1}{2} b \left(\lambda_1^2 + \lambda_2^2 + \frac{1}{\lambda_1^2 \lambda_2^2} - 3 \right) \right)} \tag{5-1}$$

$$\sigma_2 = \lambda_2 \frac{1}{2} a \left(2\lambda_2 - \frac{2}{\lambda_2^3 \lambda_1^2} \right) e^{\left(\frac{1}{2} b \left(\lambda_1^2 + \lambda_2^2 + \frac{1}{\lambda_1^2 \lambda_2^2} - 3 \right) \right)} \tag{5-2}$$

$$\sigma_3 = 0 \tag{5-3}$$

The axial and circumferential stresses were verified using a simple FEA model consisting of 5×5×2 elements (Figure 5-1).

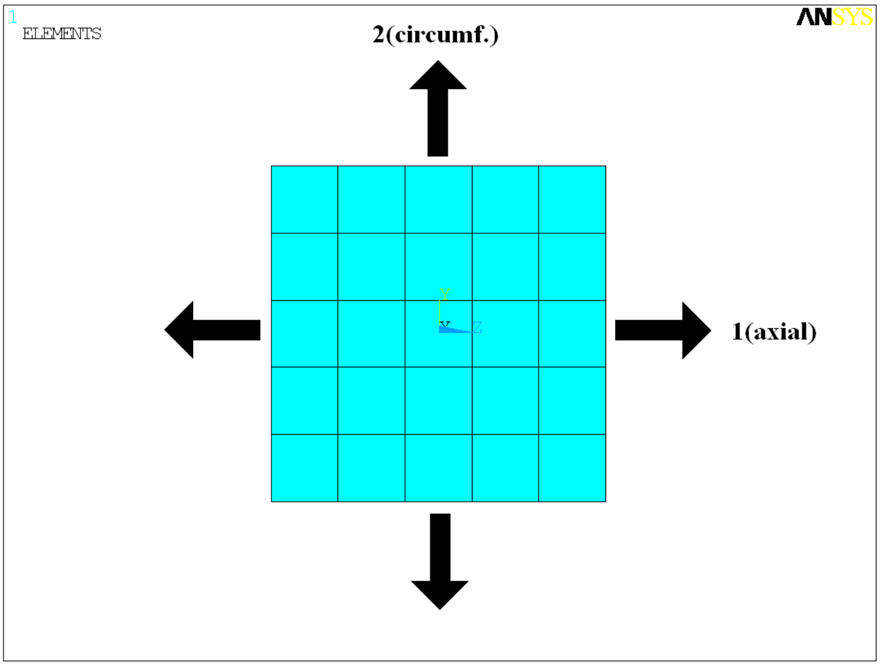

Figure 5-1 FEA model

The „*membrane*" components of the linearized stresses [63] in the corresponding directions were used for the verification of the model. This stresses can be also computed using „*FSUM*" command in ANSYS which sumarizes the nodal forces of elements [63] (like a force gauge in a real experiment) and divides them by the deformed dimensions of element. The both approaches are equivalent. The comparison between the analytical and numerical solutions for the equbiaxial tension test is shown in the Figure 5-2:

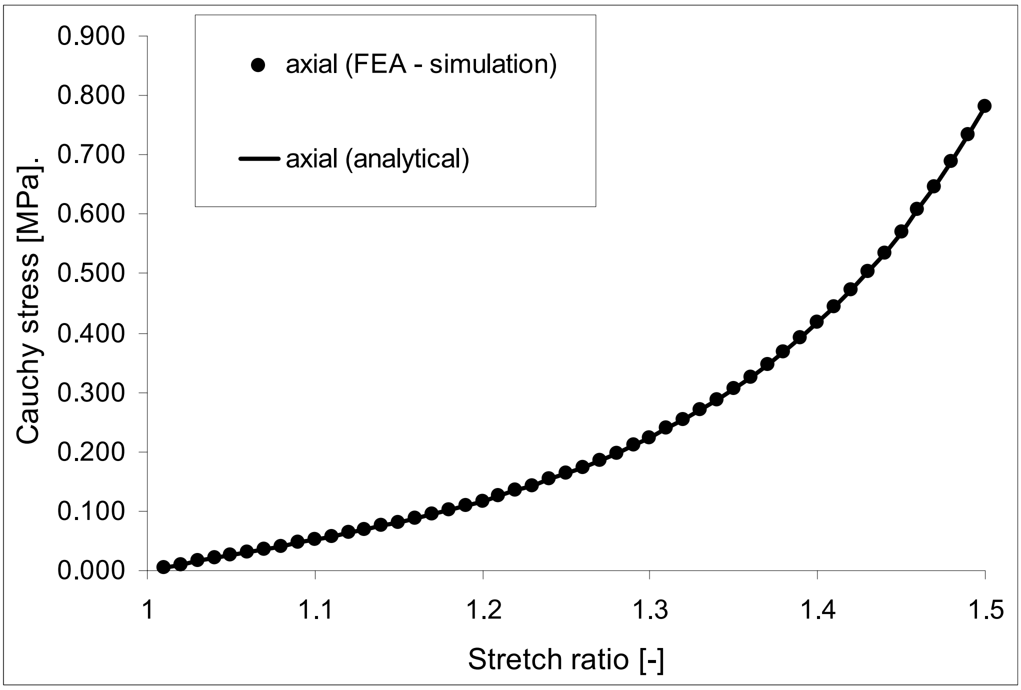

Figure 5-2 Stress-stretch response in the equibiaxial tension test – Isotropic constitutive model (4.2.2)

5.2.2 Exponential model poposed by Fung (4.2.4)

The material parameters used for the anisotropic exponential model proposed by Fung are recapitulated in Tab. 4:

Tab. 4 Anisotropic exponential model proposed by Fung - material parameters

Model	c	b_1	b_2	b_3	b_4	b_5	b_6	d
	[MPa]	[-]	[-]	[-]	[-]	[-]	[-]	[MPa]
Fung (4.2.4)	34.663	0.0125	0.0101	0.0103	0.0071	0.0064	0.0067	0.001

The FEA model and the valuation of stresses is the same as in the previous chapter 5.2.1 (Figure 5-1). The analytical expression of axial „1” and circumferential „2” stress components for the anisotropic exponential model (4.2.4) are obtained using equation (4-16) substituted into equation (4-40):

$$\sigma_1 = \lambda_1^2 (\frac{1}{2} c \left(2b_2E_1 + 2b_4E_2 + 2b_5 \left(\frac{1}{2(2E_1+1)(2E_2+1)} - \frac{1}{2} \right) \right) \cdot \tag{5-4}$$

$$\cdot e^{\left(b_1E_2^2 + b_2E_1^2 + b_3 \left(\frac{1}{2(2E_1+1)(2E_2+1)} - \frac{1}{2} \right) + 2b_4E_2E_1 + 2b_5E_1 \left(\frac{1}{2(2E_1+1)(2E_2+1)} - \frac{1}{2} \right) + 2b6E_2 \left(\frac{1}{2(2E_1+1)(2E_2+1)} - \frac{1}{2} \right) \right)} -$$

$$- \frac{1}{2(2E_1+1)^2(2E_2+1)} \left(c \left(2b_5E_1 + 2b_6E_2 + 2b_3 \left(\frac{1}{2(2E_1+1)(2E_2+1)} - \frac{1}{2} \right) \right) \right) \cdot$$

$$\cdot e^{\left(b_1E_2^2 + b_2E_1^2 + b_3 \left(\frac{1}{2(2E_1+1)(2E_2+1)} - \frac{1}{2} \right) + 2b_4E_2E_1 + 2b_5E_1 \left(\frac{1}{2(2E_1+1)(2E_2+1)} - \frac{1}{2} \right) + 2b6E_2 \left(\frac{1}{2(2E_1+1)(2E_2+1)} - \frac{1}{2} \right) \right)})$$

$$\sigma_2 = \lambda_2^2 (\frac{1}{2} c \left(2b_4E_1 + 2b_1E_2 + 2b_6 \left(\frac{1}{2(2E_1+1)(2E_2+1)} - \frac{1}{2} \right) \right) \cdot \tag{5-5}$$

$$\cdot e^{\left(b_1E_2^2 + b_2E_1^2 + b_3 \left(\frac{1}{2(2E_1+1)(2E_2+1)} - \frac{1}{2} \right) + 2b_4E_2E_1 + 2b_5E_1 \left(\frac{1}{2(2E_1+1)(2E_2+1)} - \frac{1}{2} \right) + 2b6E_2 \left(\frac{1}{2(2E_1+1)(2E_2+1)} - \frac{1}{2} \right) \right)} -$$

$$- \frac{1}{2(2E_1+1)(2E_2+1)^2} \left(c \left(2b_5E_1 + 2b_6E_2 + 2b_3 \left(\frac{1}{2(2E_1+1)(2E_2+1)} - \frac{1}{2} \right) \right) \right) \cdot$$

$$\cdot e^{\left(b_1E_2^2 + b_2E_1^2 + b_3 \left(\frac{1}{2(2E_1+1)(2E_2+1)} - \frac{1}{2} \right) + 2b_4E_2E_1 + 2b_5E_1 \left(\frac{1}{2(2E_1+1)(2E_2+1)} - \frac{1}{2} \right) + 2b6E_2 \left(\frac{1}{2(2E_1+1)(2E_2+1)} - \frac{1}{2} \right) \right)})$$

$$\sigma_3 = 0 \tag{5-6}$$

The comparison between analytical and numerical solutions for the equbiaxial tension test is shown in the Figure 5-3:

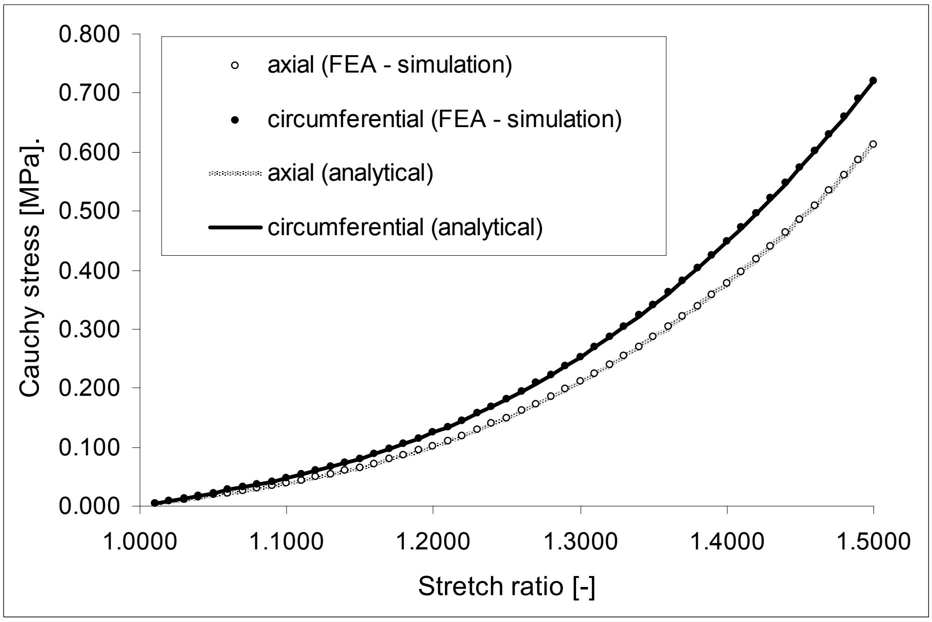

Figure 5-3 Stress-stretch response in the equibiaxial tension test – Anisotropic Fung model (4.2.4)

5.2.3 A single-layer anisotropic exponential model (4.2.6)

The material parameters used for anisotropic exponential single-layer model are recapitulated in the Tab. 5:

Tab. 5 A single-layer anisotropic exponential model – material parameters

Model	c	k_1	k_2	φ	d
	[MPa]	[MPa]	[-]	[deg]	[MPa]
Single-layer (4.2.6)	0.073	0.020	2.213	58.3°	0.0001

The analytical expression of axial „1" and circumferential „2" stress components for the single-layer anisotropic exponential model (4.2.6) are obtained using equation (4-19) substituted into equation (4-39):

$$\sigma_1 = \lambda_1(\frac{1}{2}c\left(2\lambda_1 - \frac{2}{\lambda_1^3\lambda_2^2}\right) + 4k_1(\lambda_1^2\cos^2(\varphi) + \lambda_2^2\sin^2(\varphi) - 1)\lambda_1\cos^2(\varphi)e^{\left(k_2(\lambda_1^2\cos^2(\varphi)+\lambda_2^2\sin^2(\varphi)-1)^2\right)}) \tag{5-7}$$

$$\sigma_2 = \lambda_2(\frac{1}{2}c\left(2\lambda_1 - \frac{2}{\lambda_2^3\lambda_2^2}\right) + 4k_1(\lambda_1^2\cos^2(\varphi) + \lambda_2^2\sin^2(\varphi) - 1)\lambda_2\sin^2(\varphi)e^{\left(k_2(\lambda_1^2\cos^2(\varphi)+\lambda_2^2\sin^2(\varphi)-1)^2\right)}) \tag{5-8}$$

$$\sigma_3 = 0 \tag{5-9}$$

The axial and circumferential stresses were verified using a simple FEA model consisting of 5×5×2 elements (Figure 5-4). The direction of the unit vectors of two families of collagen fibres were defined for every element individually.

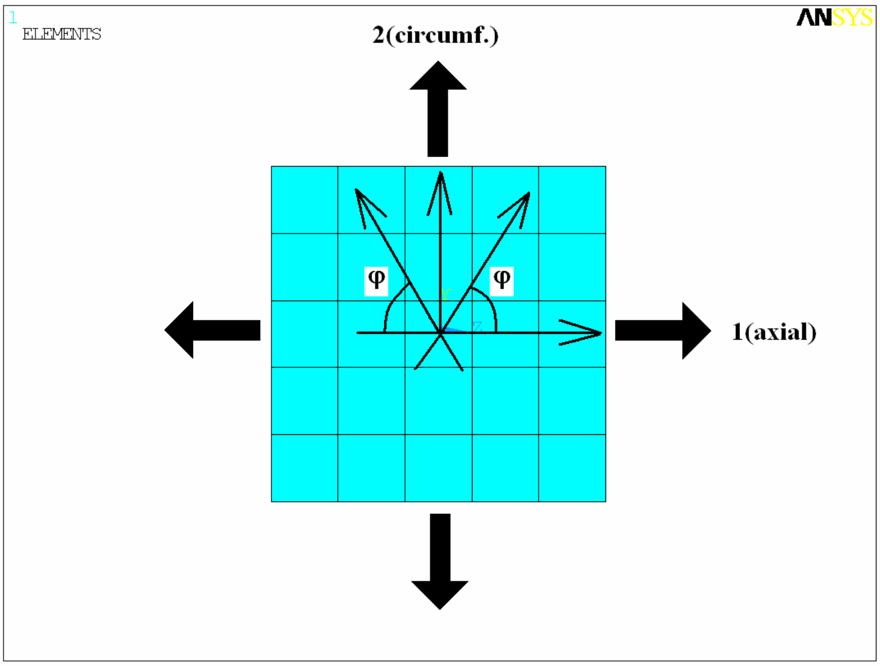

Figure 5-4 FEA model

The comparison between analytical and numerical evaluations for equibiaxial tension test is shown in the Figure 5-5.

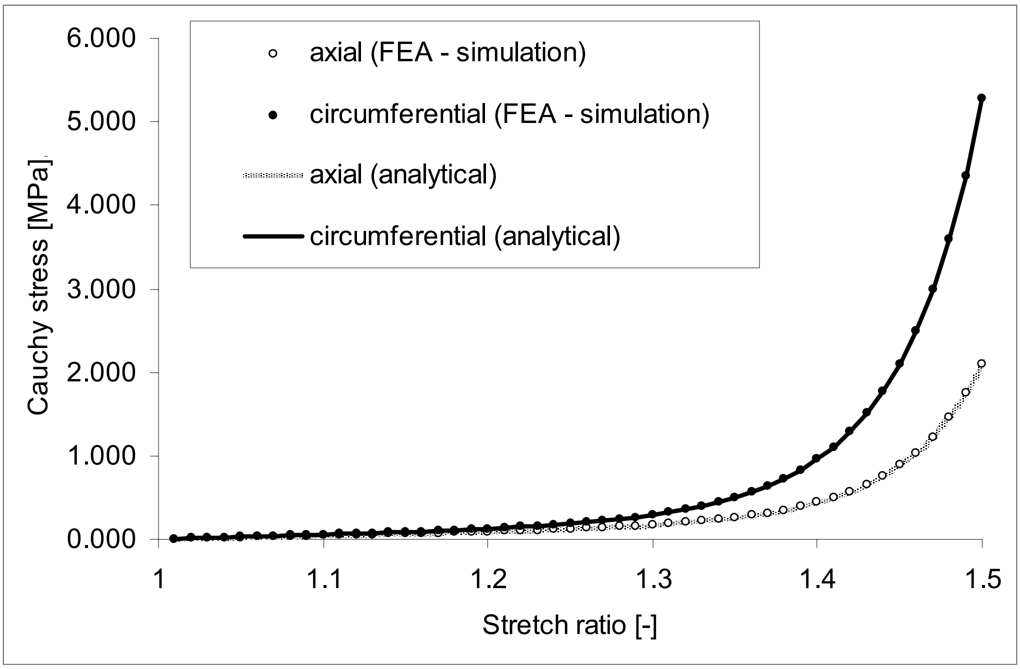

Figure 5-5 Stress-stretch response in equibiaxial tension test – anisotropic exponential single-layer model (4.2.6)

5.2.4 A double-layer anisotropic exponential model (4.2.7)

The material parameters used for anisotropic exponential double-layer model are recapitulated in the Tab. 6:

Tab. 6 Anisotropic exponential double-layer model – material parameters

Model	c	k_{1A}	k_{2A}	φ_A	k_{1B}	k_{2B}	φ_M	$f^A=f^B$	d
	[MPa]	[MPa]	[-]	[deg]	[MPa]	[-]	[deg]	[-]	[MPa]
Double-layer (4.2.7)	0.019	0.051	0.011	84.9°	0.080	1.015	36.9°	0.5	0.00001

The analytical expressions for axial „1" and circumferential „2" stress components of the anisotropic exponential double-layer model (4.2.7) are obtained using equation (4-28) substituted into equation (4-39):

$$\sigma_1 = \lambda_1(\frac{1}{2}c\left(2\lambda_1 - \frac{2}{\lambda_1^3\lambda_2^2}\right) + 4k_1 f^A(\lambda_1^2\cos^2(\varphi) + \lambda_2^2\sin^2(\varphi) - 1)\lambda_1\cos^2(\varphi)e^{\left(k_2(\lambda_1^2\cos^2(\varphi)+\lambda_2^2\sin^2(\varphi)-1)^2\right)} + \tag{5-10}$$

$$+4k_3 f^M(\lambda_1^2\cos^2(\varphi) + \lambda_2^2\sin^2(\varphi) - 1)\lambda_1\cos^2(\varphi)e^{\left(k_4(\lambda_1^2\cos^2(\varphi)+\lambda_2^2\sin^2(\varphi)-1)^2\right)})$$

$$\sigma_2 = \lambda_2(\frac{1}{2}c\left(2\lambda_1 - \frac{2}{\lambda_2^3\lambda_2^2}\right) + 4k_1 f^A(\lambda_1^2\cos^2(\varphi) + \lambda_2^2\sin^2(\varphi) - 1)\lambda_2\sin^2(\varphi)e^{\left(k_2(\lambda_1^2\cos^2(\varphi)+\lambda_2^2\sin^2(\varphi)-1)^2\right)} + \tag{5-11}$$

$$+4k_3 f^M(\lambda_1^2\cos^2(\varphi) + \lambda_2^2\sin^2(\varphi) - 1)\lambda_2\sin^2(\varphi)e^{\left(k_4(\lambda_1^2\cos^2(\varphi)+\lambda_2^2\sin^2(\varphi)-1)^2\right)})$$

$$\sigma_3 = 0 \tag{5-12}$$

The axial and circumferential stresses were verified using a simple FEA model consisting of two layers („A“-adventitia and „M“-media) with 5×5×1 elements (Figure 5-6). The volume fraction f^A and f^M must be kept. Each individual layer is modeled using the single-layer exponential model 4.2.6 with the same isotropic part. The directions of the unit vectors of the families of collagen fibres were defined for every layer and every element individually.

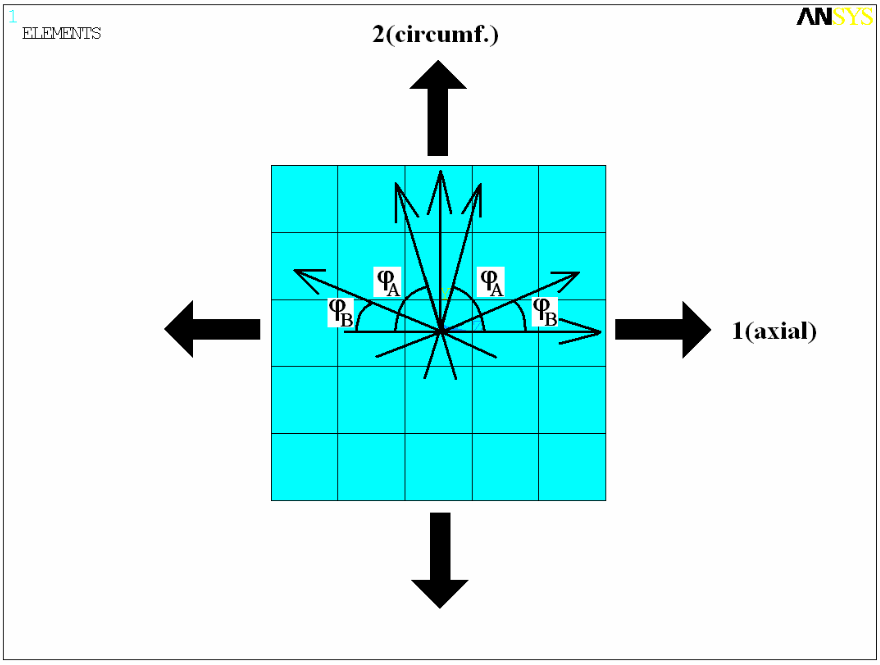

Figure 5-6 FEA model

The comparison between analytical and numerical solutions for equibiaxial tension test is shown in the Figure 5-7.

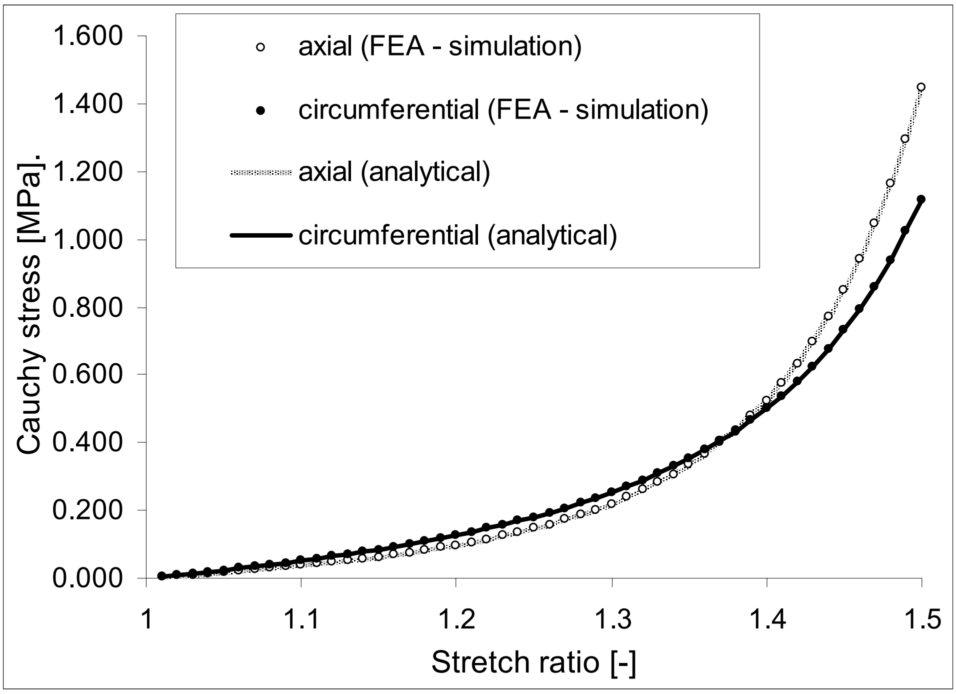

Figure 5-7 Stress-stretch response in the equibiaxial tension test – the anisotropic exponential double-layer model (4.2.7)

5.3 Parameters of the AAA model (AAA properties)

In this section the present state of the key factors for AAA FEA models creation and for evaluation of the results are summarized. The reason is absence of the mechanical testing at real human AAA specimens in our institut. In cooperation with St. Ann Hospital in Brno only CT scans were available for geometry reconstruction of real human AAA.

5.3.1 Failure and mechanical properties of the human arterial wall

The papers [28], [33] are focused to uniaxial tensile testing of freshly excised human aneurysmal and nonaneurysmal infrarenal aorta. Study subjects were patients undergoing surgical repair of AAA. Aortic wall specimens were categorized in three groups: longitudinally oriented AAA specimens (AAA_{long}), circumferentially oriented AAA specimens (AAA_{circ}) or longitudinally oriented „normal" aortic specimens from organ donors ($NORMAL_{long}$). Fifty-two longitudinally oriented specimens were obtained from 45 patients aged 69±2 years and 19 circumferentially oriented specimens from 16 patients aged 76±2 years. Seven „normal" specimens were obtained from the infrarenal aorta of seven cadaveric organ donors aged 47±4 years. The ultimate Cauchy stresses are 864±102 kPa for AAA_{long} specimens, 1019±160 kPa for AAA_{circ} specimens and 2014±394 kPa for $NORMAL_{long}$ specimens. Representative experimental data are shown on Figure 5-8, Figure 5-9 and Figure 5-10.

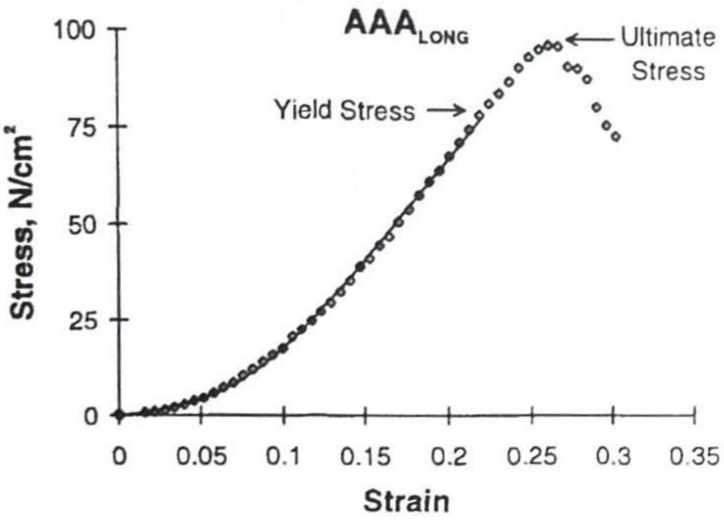

Figure 5-8 Uniaxial tension test of an AAA_{long} specimen (Cauchy stress vs. natural strain)

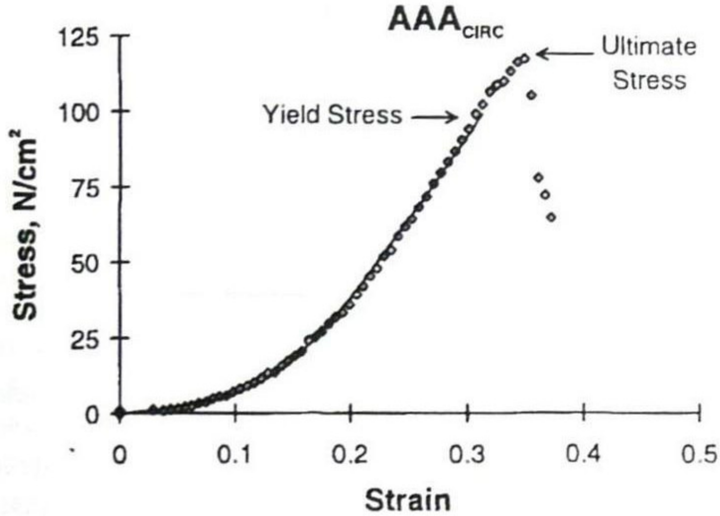

Figure 5-9 Uniaxial tension test of an AAA_{circ} specimen (Cauchy stress vs. natural strain)

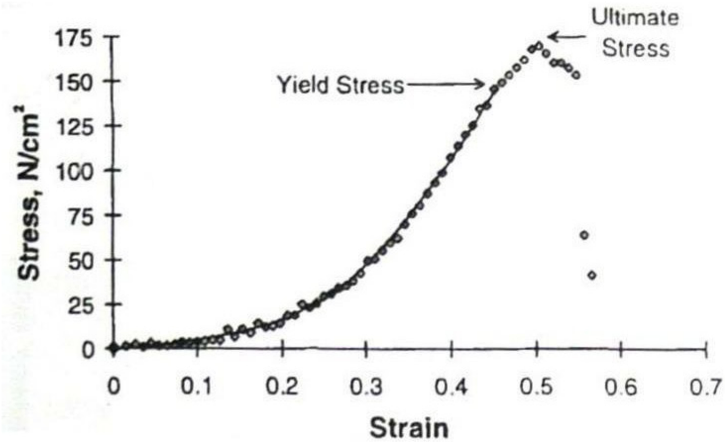

Figure 5-10 Uniaxial tension test of a $NORMAL_{long}$ specimen (Cauchy stress vs. natural strain)

Van de Geest et al. [34] reported anisotropic mechanical response of the healthy abdominal aorta of patients greater than 60 years old (Figure 5-11). The different curves represent different ratios between axial (LL) and circumferential (TT) loading. The circumferential stresses appear to have a slightly steeper increase in stress at higher strains. It is due to the orientation of the collagen fibres and their higher resistance to circumferential stretching than to axial stretching. Author also reported mechanical response of the AAA wall in biaxial tension tests (Figure 5-12). It is evident that the maximal strains in AAA wall are significantly less than maximal strains ina healthy artery wall whereas the maximum stress at the AAA wall is significantly larger than maximum stress at the healthy artery. Thus the trend of increase in arterial stiffness within the AAA tissue is evident.

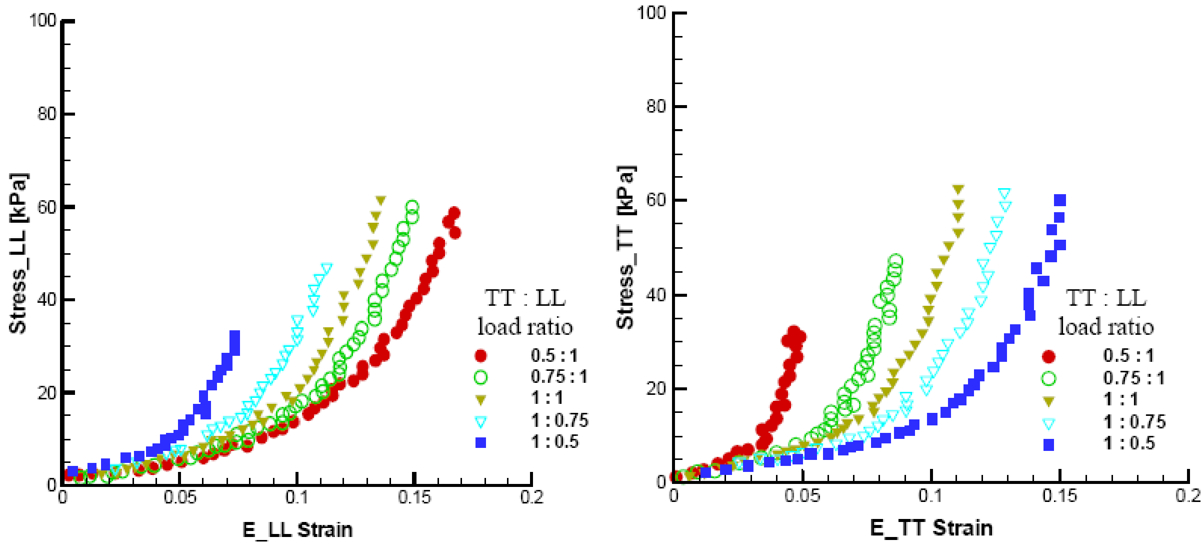

Figure 5-11 Biaxial mechanical properties of the healthy abdominal aorta [34], [38]

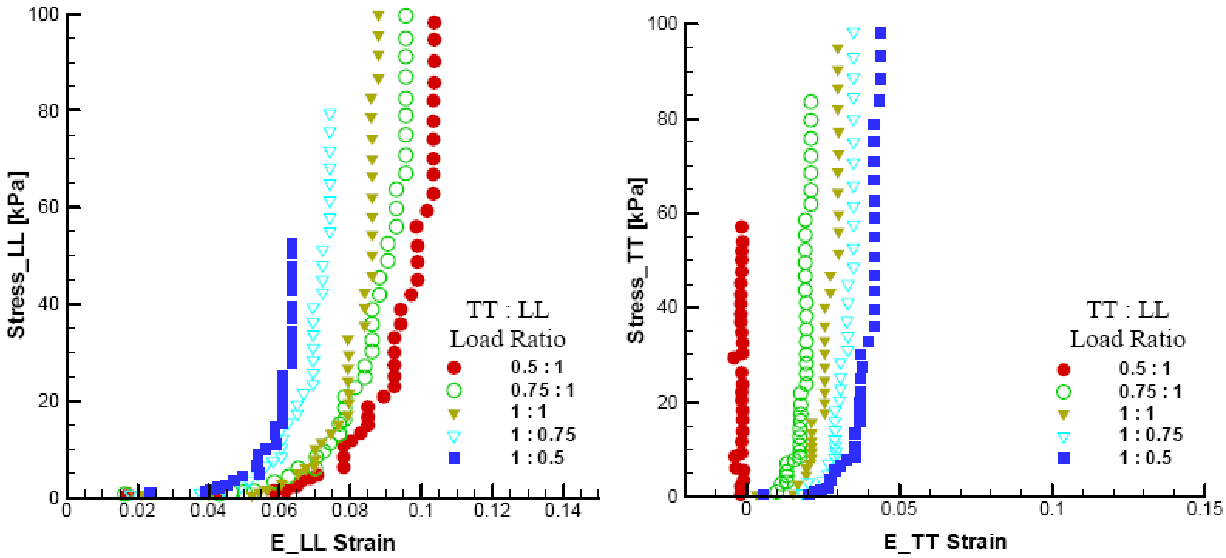

Figure 5-12 Biaxial mechanical properties of the AAA wall [34], [38]

Mohan [50] and Ohashi et al. [47] reported failure properties of the human aortic tissue in the biaxial tension tests. The biaxial stress state was realized using the pressure-imposed test. A detailed view of the experimental setup for specimen mounting is shown schematically in Figure 5-13. The pressure was applied not by water but by air through a rubber ballon. Both authors used the human thoracic aortas. The main emphasis in the first mentioned study [50] was on the impact-type high strain rate ($20s^{-1}$) behavior and all tests were performed with the intention of obtaining failure properties of the aortic tissue in biaxial tension compared to uniaxial tension.

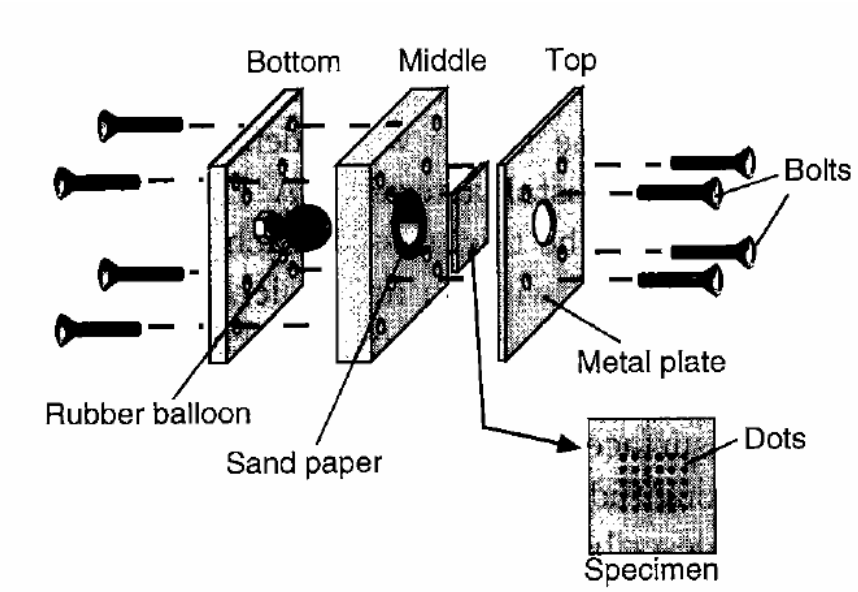

Figure 5-13 Experimental setup of the specimen mounting [47]

Both authors reported that the failure of the aortic tissue always took place always (by means of) with a tear in the direction perpendicular to the longitudinal axis of the aorta. Mohan [50] compared the failure properies in the biaxial mode with failure properties in the longitudinal uniaxial mode since in all tests the initial tear occurred in the tangential direction. That is, the failure was due to stretching in the longitudinal direction. The mean ratio of biaxial vs. uniaxial tension strength was 1.11 [-]. Ohashi et al. [47] also used biaxial and uniaxial tension tests. The reported breaking stress from the pressure-imposed tests was 2.3±0.8 MPa (mean±SD) and 2.0±0.7 MPa from uniaxial tension tests, thus the mean ratio of biaxial vs. uniaxial tension tests was 1.15 [-]. For all groups, there were no significant differences in breaking stress between the proximal and distal specimens. The breaking stress from the uniaxial tension tests in the circumferential direction results 3.3±0.6 MPa. In the pressure-imposed tests, a rupture of the aorta occurred and the crack propagation proceeded along the circumferential direction of the aortas. This result indicates that the ultimate tensile strength is higher in the circumferential direction than in the longitudinal direction.

The pressure-imposed test using the AAA specimens are not reported in the recent literature therefore there is no uniquely determined AAA failure criterion describing its biaxial behavior.

5.3.2 Thickness of the human AAA wall

Generaly contrast CT images were used to reconstruct AAA geometries. In some cases the boundary between outer wall, lumen or intraluminal thrombus is hardly discernible. In several studies hypothetical models of AAA or models reconstructed from CT images are simplified and the wall thickness is considered uniform. The most frequent AAA thickness used in literature are:

- 2.0 mm – E. van Nunen [37], Basciano Ch. A. [38], S. de Putter [42], Mohan and Melvin [50]
- 1.9 mm – Raghavan [28], [30], Jia Lu [43], [44]
- 1.5 mm – Raghavan [27], Rodriguez [45],
- 0.23 mm (at rupture side) to 4.26 mm (at calcified side) – Raghavan [29]

The most recent AAA modesl used in literature do not explicitly model the individual contributions from arterial layers (adventitia and media). Holzapfel [8] assume the media occupies 2/3 of the thickness but this ration is based on data for the rabbit carotid artery. Holzapfel also assumes that this to be true for the human left anterior descending coronary artery. In the next study [10] Holzapfel reported tension testing of human abdominal aorta where the mean thicknesses of intimal, medial and adventitial samples were measured and these values are 0.33, 1.32 and 0.96 mm; thus the total wall thickness is 2.61 mm.

5.3.3 Constitutive model and material parameters used in literature

The following chapter summarize the constitutive models and their material parameters used in recent literature in AAA stress-strain analyses:

- Thubrikar et al. [52] used the linear elastic constitutive model with Young´s modulus 4.66 MPa and Poisson ratio μ=0.45 [-].
- Putter et al. [42] and Lu et al. [43] used isotropic constitutive model (Yeoh model see. chapter 4.2.1) in AAA simulations. For the material parameteres a and b they used the mean values of 0.174 MPa and 1.881 MPa respectively.
- In the following study Lu et al. [44] used the anisotropic constitutive model described by Holzapfel [8]. For the material parameters authors used c=0.15 MPa, $k1$=2 MPa, $k2$=1.25, φ= ±36.25° (from circumferential to axial direction) and d=0.00002 MPa.

The comparisons between the constitutive models are shown on the following figures (Figure 5-14, Figure 5-15 and Figure 5-16) using virtual equibiaxial and planar tension tests:

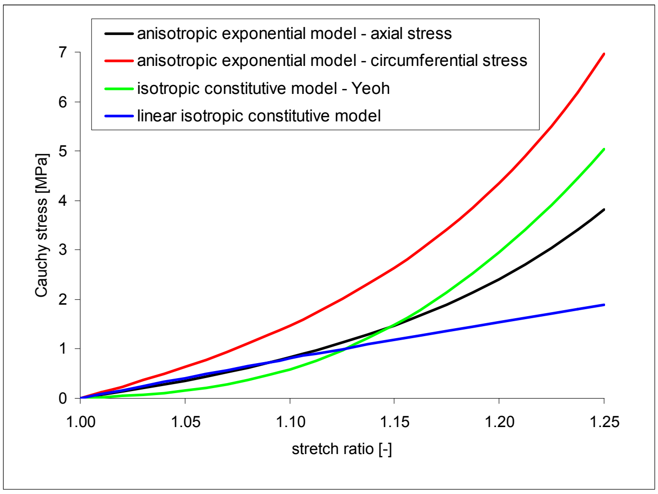

Figure 5-14 Stress-stretch responses in equibiaxial tension test

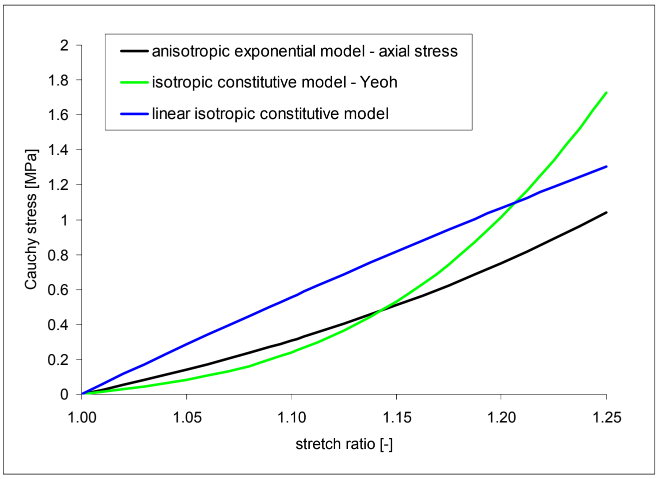

Figure 5-15 Stress-stretch responses in planar tension test – axial direction

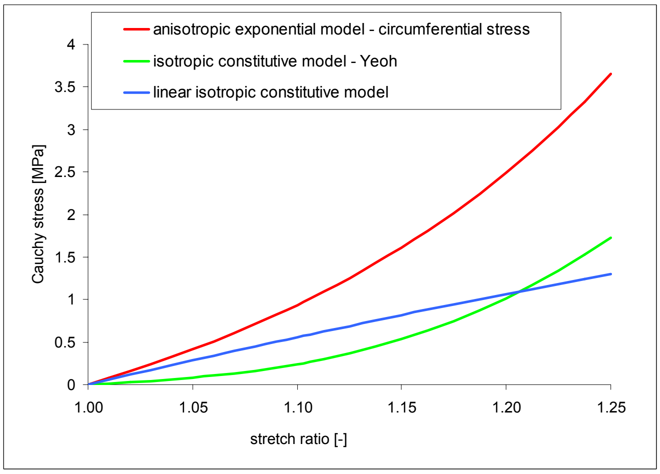

Figure 5-16 Stress-stretch responses in planar tension tests – circumferential direction

5.3.4 Constitutive models and material parameters used in presented AAA simulations

As mentioned in the introduction of this chapter, isotropic exponential and single-layer anisotropic exponential constitutive model were used in this work. For the single-layer anisotropic constitutive model of AAA, the material parameters described in chapter (5.3.3) were used. The material parameters used for the isotropic exponential constitutive model were derived from the material parameters for the anisotropic constitutive model using a virtual experiment (Figure 5-17). The objective is an analysis of influence of anisotropy vs. isotropy on extreme stresses in aneurysm.

Tab. 7 Anisotropic and isotropic exponential constitutive models – material parameters

Model	c	k_1	k_2	φ	d
	[MPa]	[MPa]	[-]	[deg]	[MPa]
Single-layer (4.2.6)	0.150	2.000	1.250	53.72°	0.00002
Model	a	b	d		
	[MPa]	[-]	[MPa]		
Isotropic (4.2.2)	1.800	3.590	0		

*note: the angle of fibres φ is measured from axial to circumferential direction

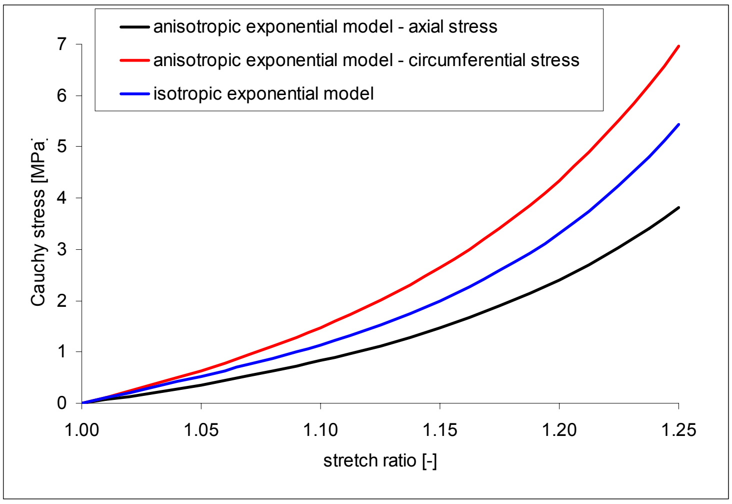

Figure 5-17 Stress-stretch responses in the simulated equibiaxial tension test

Material parameters used for the anisotropic double-layer exponential model were calculated from the mechanical response of the AAA wall (Figure 5-12). The numerical data were not available therefore the data were derived only from the mentioned Figure 5-12. The approximation is shown on the Figure 5-18:

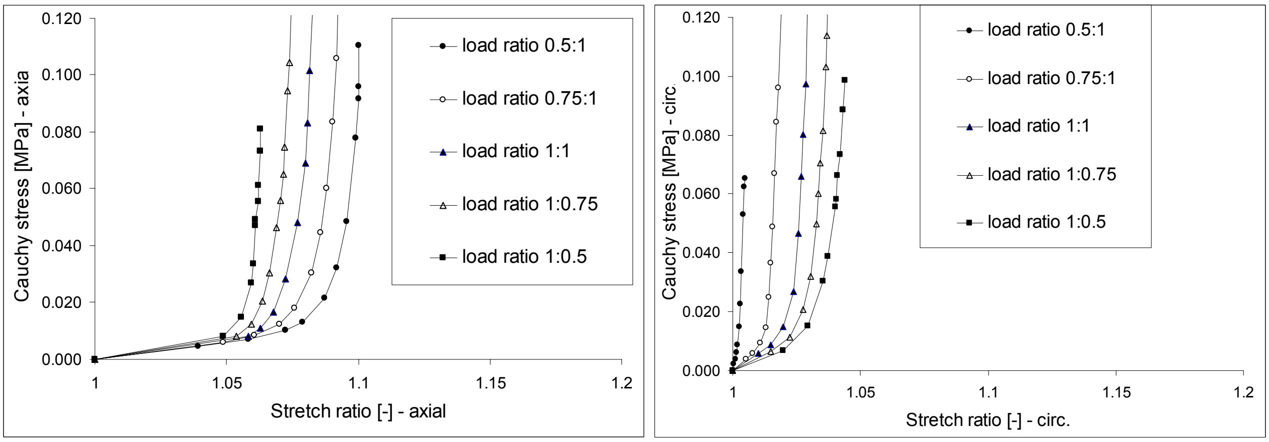

Figure 5-18 Biaxial mechanical properties of AAA wall reconstructed from [34]

Tab. 8 Anisotropic exponential double-layer constitutive model – material parameters

Model	c	k_{1A}	k_{2A}	φ_A	k_{1M}	k_{2M}	φ_M	f^A	f^M
	[MPa]	[MPa]	[-]	[deg]	[MPa]	[-]	[deg]	[-]	[-]
Double-layer (4.2.7)	0.027	0.00025	460	39.9°	0.004	430	49.9°	0.42	0.58

*note: the angle of fibres φ is measured from axial to circumferential direction

The assumption of magnitude of f^A and f^M volume fraction factors of artery layer A (adventitia) and M (media) was based on values described by Holzapfel et al. [10]. The intima layer was not considered. The angles of adventitia φ^A and media φ^M fibers are similar to findings reported in [10] where these angles (measured from circumferential to axial direction) reach 58.9° and 37.8° respectively. The stiffness of the AAA wall in the circumferential direction is evidently higher (Figure 5-12) then the stiffness in the axial direction, which causes the calculated stiffness of media fibers k_{1M} to be high order than stiffness of the adventitia fibers k_{1A}. The study [10] reported uniaxial stress-strain behavior of isolated aortic layers where the stiffness of media in circumferential direction is higher then the stiffness of the adventitia. The stiffness of media in axial direction is higher at lower strains and vice versa the stiffness of adventitia is higher at higher strains. Similar results and rate of material parameters are also reported in [8] where data for a carotid artery from a rabbit are used. The exponentiality of fibers stiffness k_{2A} and k_{2M} are similar for both layers.

5.4 Hypothetical idealised geometrical aneurysm model

Hypothetical idealised geometrical model was used for analysis of the influence of each individual geometric variable (maximum diameter, asymmetry index, saccular index, AAA thickness) on the mechanical response of AAA wall. The influence of various constitutive models (isotropy vs. anisotropy) was also evaluated. All the FE models solved here consist of linear solid elements SOLID185 (3D 8node). Four elements through the thickness of the artery wall were used. For the anisotropic constitutive exponential model the directions of unit vector of family collagen fibres were defined for every element individually. For the physiological range of loading the inner pressure 0.016MPa (120 mmHg) was considered. The thickness is considered 1.5mm and 1.9mm (chapter 5.3.2) for all models except for the anisotropic double-layer constitutive model where the total thickness is 2.28mm (0.96mm adventitia and 1.32mm media).

5.4.1 Geometric model

The shape of the hypothetical aneurysm is defined by a function according equation (5-13) proposed in [45] (see Figure 5-19). The selected lenght of the healty cylindrical artery in the hypothetical idealised geometrical AAA model was found to be the minimum required for the boundary conditions to have no influence on the stress distribution in the evaluated locations [45].

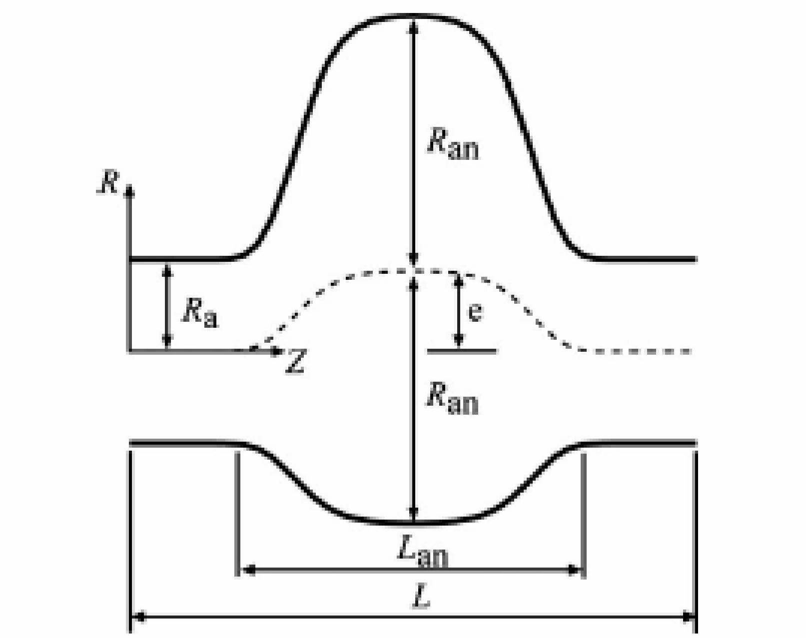

Figure 5-19 Hypothetical parametrical geometric model of the AAA

The mathematical function describing the geometry of the longitudinal section (see Figure 5-19) is given by:

$$R(Z) = R_a + (R_{an} + e - R_a - c_3 \frac{Z^2}{R_a}) \exp\left(-c_1 \left(\frac{Z}{R_a}\right)^{c_2}\right) \tag{5-13}$$

where R_a is the radius of the healty artery, R_{an} is the maximum radius of the aneurysm, c_1, c_4 is constants and c_2, c_3 are geometrical parameters depending on the geometry according to:

$$c_1 = const. \qquad c_4 = const. \qquad c_2 = \frac{c_4}{(0.5L_{an}/R_a)^{c_1}} \qquad c_3 = \frac{R_{an} - R_a}{R_a(0.8L_{an}/R_a)^2} \tag{5-14}$$

where L_{an} is the length of aneurysm. The differences between shapes are defined through dimensionless geometrical parameters, i.e.:

$$F_R = \frac{R_{an}}{R_a} \qquad F_L = \frac{L_{an}}{R_{an}} \qquad F_E = \frac{e}{(F_R - 1)R_a} \tag{5-15}$$

where F_R is ratio of maximum aneurysm radius vs. radius of healty artery, F_L is ratio between length of aneurysm vs. maximum aneurysm radius (reciprocal of the saccular index) and F_E is a measure of the aneurysmal eccentricity (asymmetry).

5.4.2 Finite element mesh and boundary conditions

Figure 5-20 shows purely hexahedral finite element mesh, applied boundary conditions and the orientation of collagen fibres included in the anisotropic exponential constitutive model.

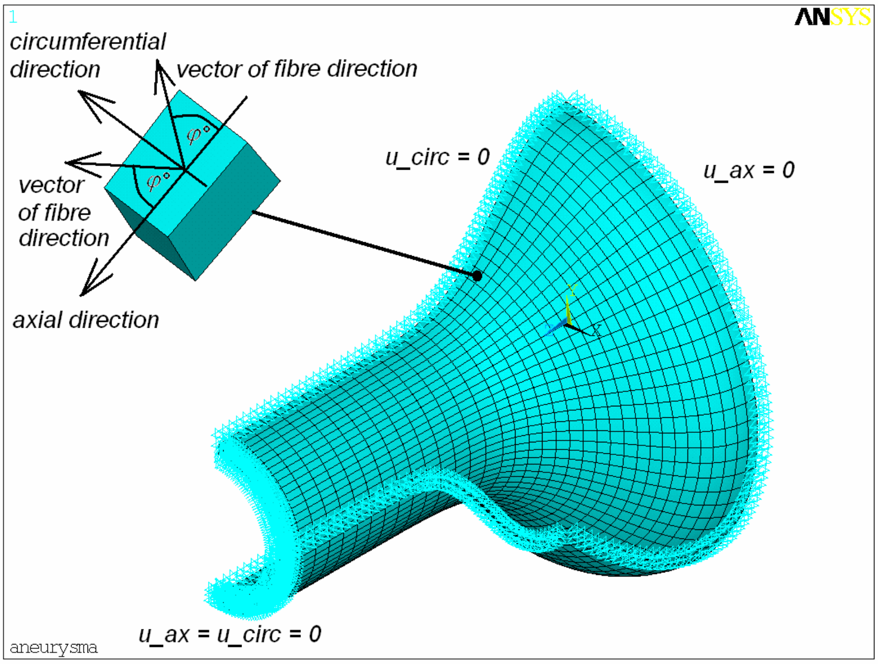

Figure 5-20 Boundary conditions and orientation of collagen fibres

5.4.3 Probabilistic design [63]

The ANSYS Probabilistic Design System (PDS) analyzes a component or a system involving uncertain input parameters. All these input parameters (geometry, material properties, boundary conditions, etc.) must be defined in the ANSYS model. The variation of these input parameters are defined as random input variables and are characterized by their distribution type (Gaussian, Lognormal, Uniform, etc.) and their distribution parameters (mean values, standard deviation, etc.). Any interdependencies between random input variables are also defined as correlation coefficients. The important results are defined as random output parameters. During the probabilistic analysis, ANSYS executes multiple analysis loops to compute the random output parameters as a function of the sets of random input variables. The values for the input variables are generated either randomly (using Monte Carlo simulation) or as prescribed samples (using Response Surface Methods).

The usual process for probabilistic design consists of the following general steps:

1. Creating of an analysis file for use during looping.
2. Establishing parameteres which correspond to those used in analysis file.
3. Declaring random input variables.
4. Specifying any correlations between the random variables.
5. Specifying random output variables.
6. Choosing the probabilistic design tool or method.
7. Executing the loops required for the probabilistic design analysis.
8. Fitting the response surface (see the note below*).
9. Generating Monte Carlo simulation samples on the response surfaces.
10. Reviewing the results of the probabilistic analysis.

*note: A response surface is an approximation describing the random output parameters as an explicit function of the random input variables. In ANSYS PDS the linear and quadratic approximations are implemented.

For the input parameters a uniform distribution and no interdependencies are considered. For the Monte Carlo simulation with the response surface the default 10,000 simulation loops [63] were used. For the correlation coefficients evaluation between the sampled data Parson linear eq. (5-16) or Spearman rank-order correlation eq. (5-17) can be used in ANSYS PDS. Generally, for the values closer to zero, the two variables are weakly correlated. For the values closer to 1 or -1, the two variables are highly correlated either in the positive or negative sense, respectively. The Figure 5-21 [72] shows the examples of sets of (x,y) points with the correlation coefficients. In the case of non-normal distributions, Pearson´s correlation coefficient will give wrong results. Basically the Spearman´s rank correlation differs from Pearson´s correlation only in the fact that the values are converted to ranks before computing the coefficient [74]. The Spearman correlation is also less sensitive to strong outliers existing in the tails of both samples (Figure 5-22) than the Pearson correlation.

$$\textit{Pearson}: \quad r = \frac{\sum_{i=1}^{n}(x_i - \bar{x})(y_i - \bar{y})}{\sqrt{\sum_{i=1}^{n}(x_i - \bar{x})^2 \sum_{i=1}^{n}(y_i - \bar{y})^2}} \quad (n = \textit{number of data points}) \tag{5-16}$$

$$\textit{Spearman}: \quad r = 1 - \frac{6\sum(Rx_i - Ry_i)^2}{n(n^2 - 1)} \quad (n = \textit{number of data points}) \tag{5-17}$$

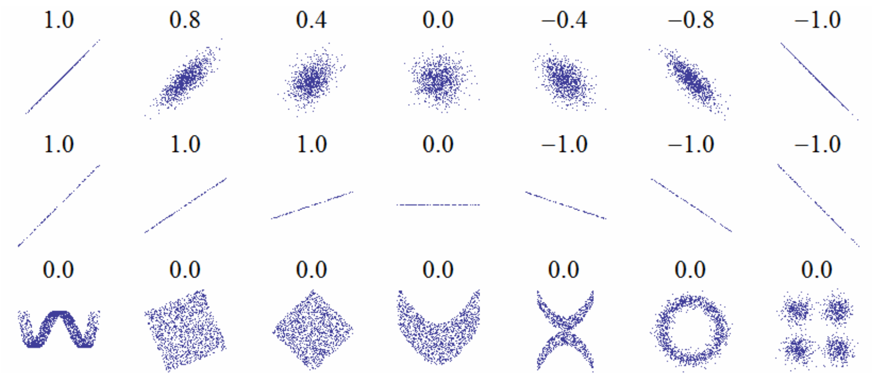

Figure 5-21 Examples of sets of (x,y) points with the correlation coefficient of x and y for each set.

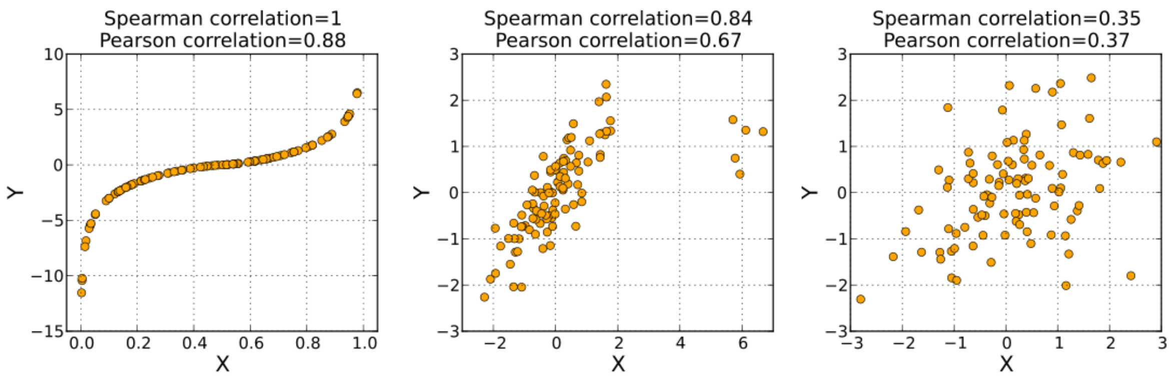

Figure 5-22 Comparison between Spearman and Pearson´s correlation coefficients

5.4.4 Influence of asymmetry, saccular index, andAAA thickness

First the influence of the AAA asymmetry (F_E parameter) and saccular index are evaluated. The range of the AAA asymmetry is from symmetrical geometry (F_E=0) to the most asymmetric geometry (F_E=1). The saccular index was generally defined as ratio of the maximum AAA diameter to the length of the AAA (1.3.1) but in this analysis the influence of saccular index was evaluated using reciprocal F_L parameter. The ratio of the AAA length and AAA maximum diameter was subdivided into two cases using c_1 and c_4 constants which control the AAA curvature at the transition part. The range of these parameters is shown in Figure 5-23, Figure 5-24 and Figure 5-25 and is in good agreement with values used in parametric study [45] as well as with clinical investigtions [27].

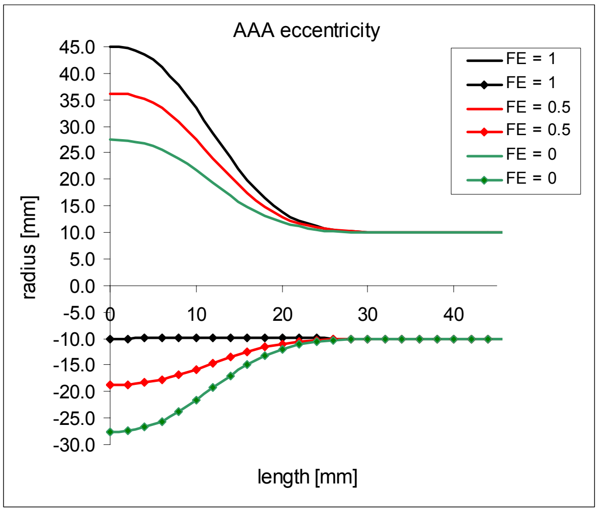

Figure 5-23 Range of AAA eccentricity

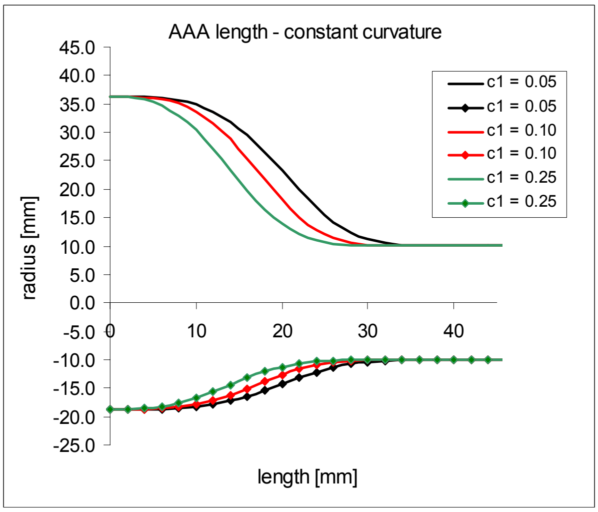

Figure 5-24 Range of AAA length – constant curvature

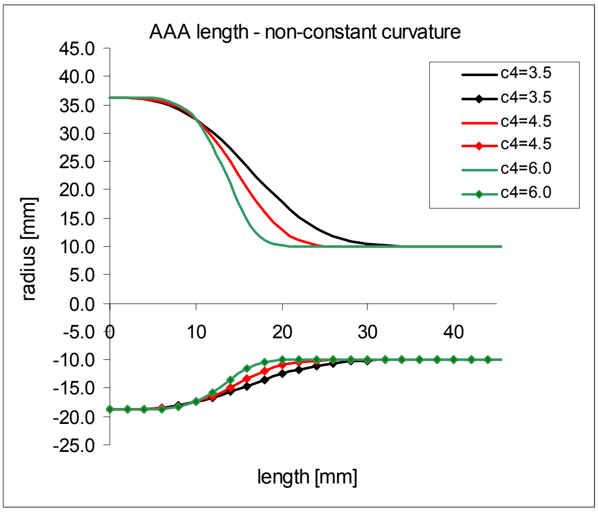

Figure 5-25 Range of AAA length – non-constant curvature

The influence of the c_1, c_4 and F_E parameters was evaluated in relation to the maximum principal stress occurred in AAA wall. Total 15 simulations were performed for evaluation what is the impact of the individual parameters on the stress response. Calculated correlation coefficients between geometrical parameters and maximum principal AAA wall stress are summarized in Tab. 9. The results show that c_1 parameter has not impact on the stress response (the correlation coefficient is approximately 0.1) thus the length of the AAA with constant curvature is independent regarding to the maximum stress. The location of the maximum principal stress is in a transition part of the AAA at outer side (Figure 5-26 and Figure 5-27). The other critical locations are at inner side of AAAs. The direction of the maximum principal stress is related with cirumferential direction. For anisotropic double-layer constitutive model the location of the maximum principal stress is on the contrary at inner side of the AAA wall (Figure 5-28).

Tab. 9 Summary of Spearman rank order correlation coefficients between geometrical parameters (c_1, c_4, F_E) and maximum principal AAA wall stress

constitutive model	input parameters		correlation coefficients		
	thickness [mm]	pressure [kPa]	c_1 [-]	c_4 [-]	F_E [-]
isotropic exponential	1.5	16	0.081	0.653	0.715
isotropic exponential	1.9	16	0.085	0.516	0.836
anisotropic - single layer	1.5	16	0.088	0.875	0.465
anisotropic - single layer	1.9	16	0.115	0.777	0.592
anisotropic - double layer	2.28	16	0.010	0.589	0.797

The tables (Tab. 23 to Tab. 25) summarize all calculated variants of c_1, c_4 and F_E parameters using different AAA thickness. The influence of the AAA thickness (1.5mm vs. 1.9mm) is approximatelly 10-20%. The stress increase ratio between maximal stresses at AAA wall (σ_1) and normal part of artery (σ_{1nom}) is approximately 3 to 4 [-] (σ_1/σ_{1nom}) and 2 to 3 [-] using the anisotropic constitutive model.

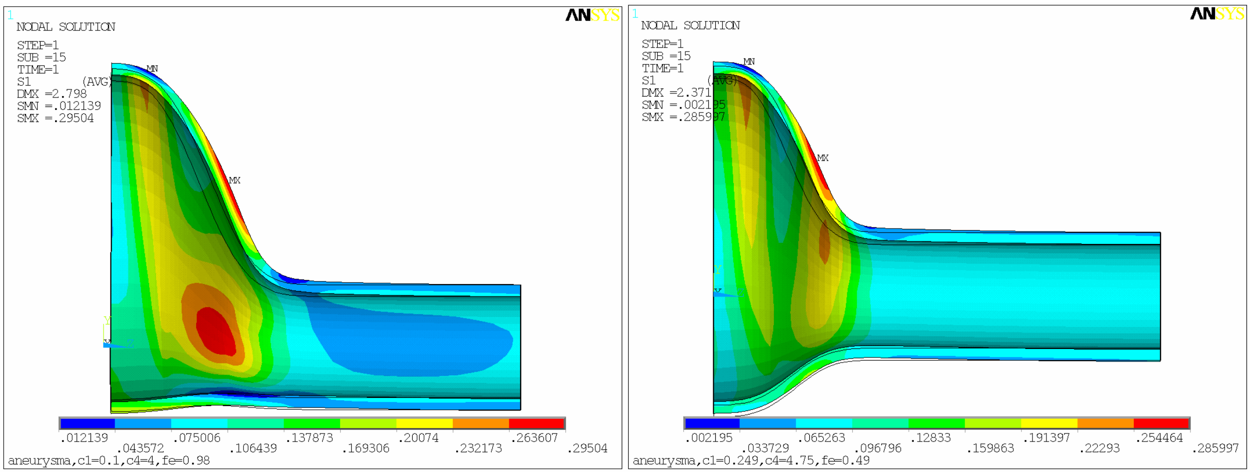

Figure 5-26 Isotropic constitutive model – maximum principal stress [MPa]

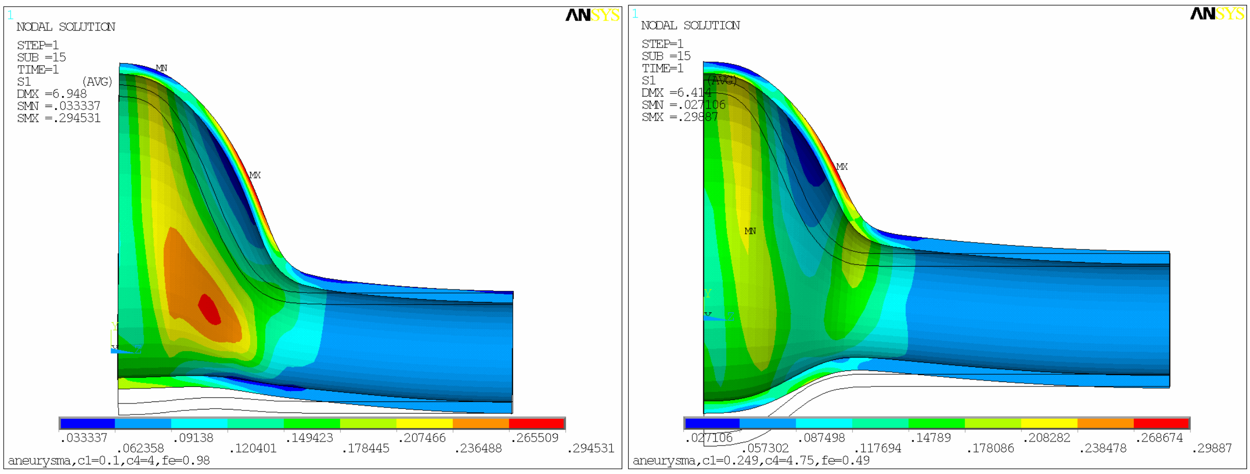

Figure 5-27 Anisotropic single-layer constitutive model – maximum principal stress [MPa]

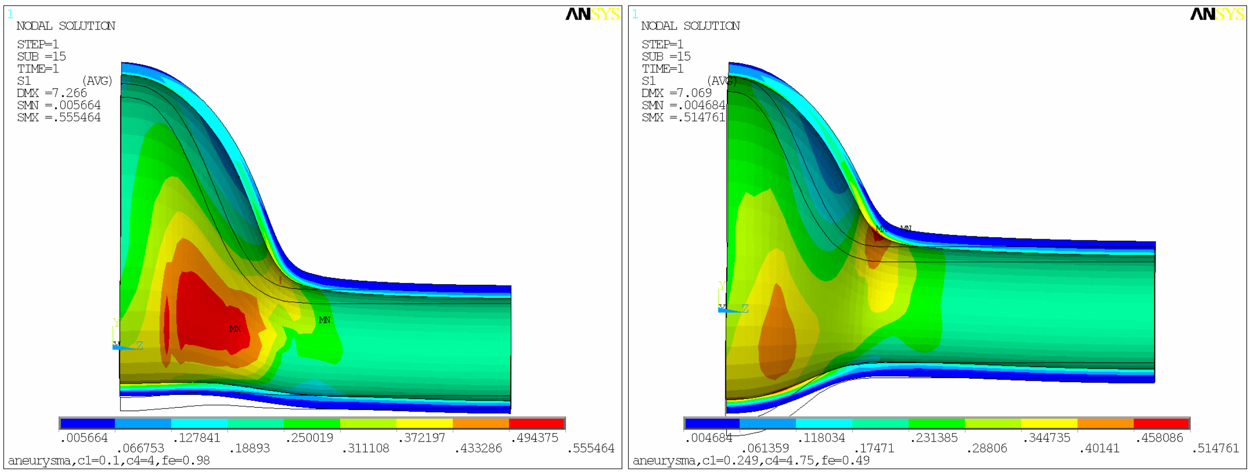

Figure 5-28 Anisotropic double-layer constitutive model – maximum principal stress [MPa]

5.4.5 Influence of maximum diameter, asymmetry and saccular index

The second analysis is focused on the analysis of the influence of the maximum diameter (F_R parameter) in combination with the asymmetry (F_E) and saccular index using non-constant curvature (c_4 parameter) defined at previous chapter. The range of the AAA maximum diameter is shown on the Figure 5-29. Total 15 simulations were performed for evaluation what is the impact of the individual parameters on the stress response. Tab. 10 summarizes the correlation coefficients which are computed using Monte Carlo simulations using 10,000 loops on response surface as mentioned in chapter 5.4.3 and correlation coefficient computed without fitting on the response surface using the software STATISTICA. The differencies in the computed correlation coefficients are minimal. The influence of the individual parameters is evident but different in dependence of the used constitutive model. Maximum stresses are compared in Tab. 26. The impact of these calculations on the stress response is clearly presented in the next chapter 5.4.6. The stress increase ratio between stresses at AAA wall (σ_I) and normal part of artery (σ_{1nom}) is approximately 2.4 to 4.0 [-] (σ_1/σ_{1nom}) and 1.9 to 2.5 [-] using the anisotropic double-layer constitutive model.

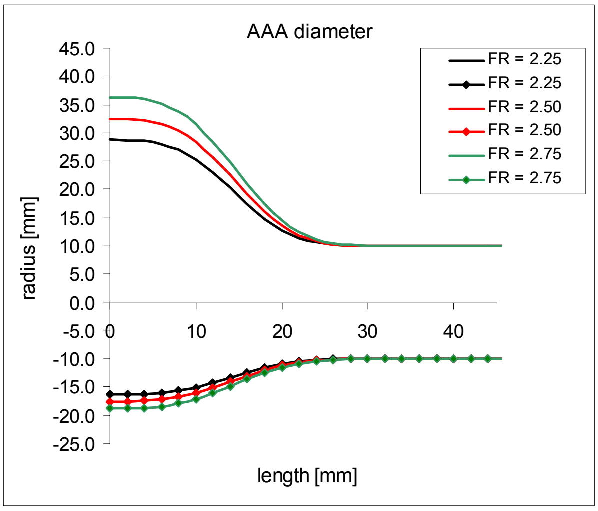

Figure 5-29 Range of AAA maximum diameter

Tab. 10 Summary of Spearman rank order correlation coefficients between geometrical parameters (F_R, c_4, F_E) and maximum principal AAA wall stress

	Input parameters		correlation coefficients ANSYS			correlation coefficients STATISTICA		
constitutive model	thickness [mm]	pressure [kPa]	F_R [-]	c_4 [-]	F_E [-]	F_R [-]	c_4 [-]	F_E [-]
isotropic exponential	1.9	16	0.437	0.395	0.788	0.489	0.348	0.778
isotropic - Yeoh	1.9	16	0.682	0.668	0.263	0.660	0.660	0.322
anisotropic - single layer	1.9	16	0.436	0.649	0.607	0.356	0.686	0.619
anisotropic - double layer	2.28	16	0.671	0.613	0.359	0.617	0.536	0.335

5.4.6 Example of response surface analysis

For demonstration of the response surface analysis, the isotropic exponential model was used. As mentioned in chapter 5.4.3 a response surface in an approximation describing random output parameters as an explicit function of random input variables (Figure 5-30 to Figure 5-32). To evaluate the response surface the random input variables have been scaled with a linear transformation. Then the response surface is fitted with the scaled random input variables. This means the response surface is expressed in terms of the scaled random input variables. The response surface is the sum of the regression terms, where each regression term includes a regression coefficient. Using analytical expression of the response surface the impact of the individual parameters can be compared. For example the value of maximum Cauchy stress vs. c_4 parameter or F_R parameter (Figure 5-33).

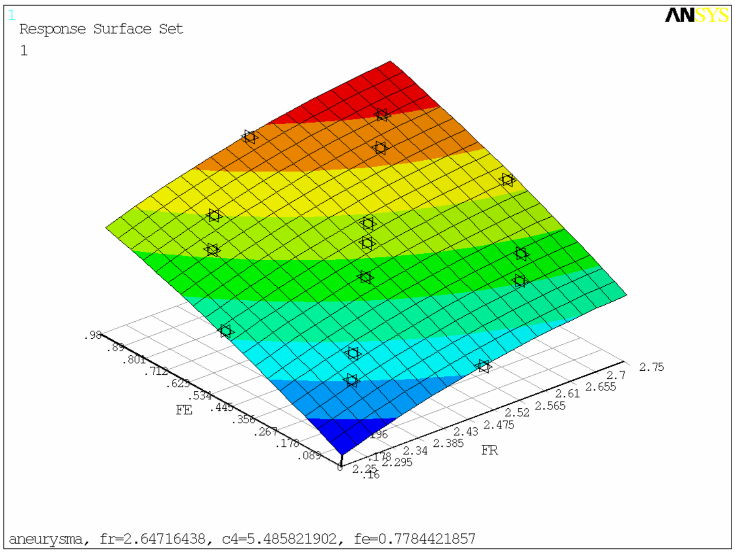

Figure 5-30 Response surface – maximum stress vs. F_E and F_R

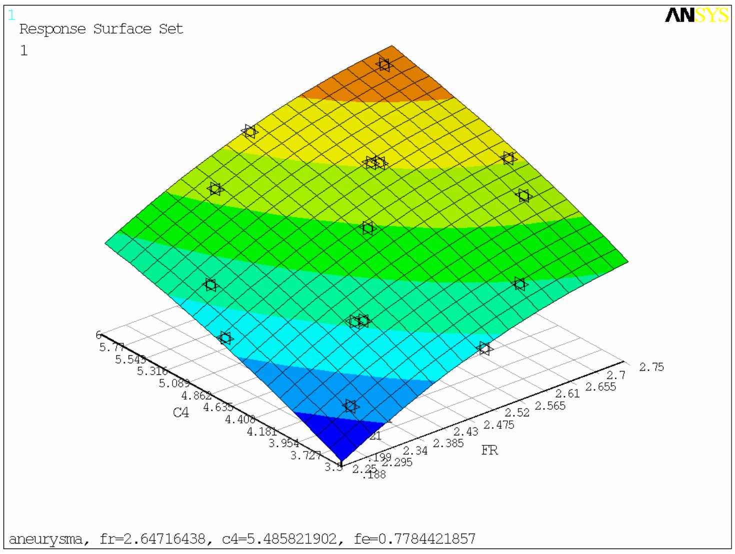

Figure 5-31 Response surface - maximum stress vs. c_4 and F_R

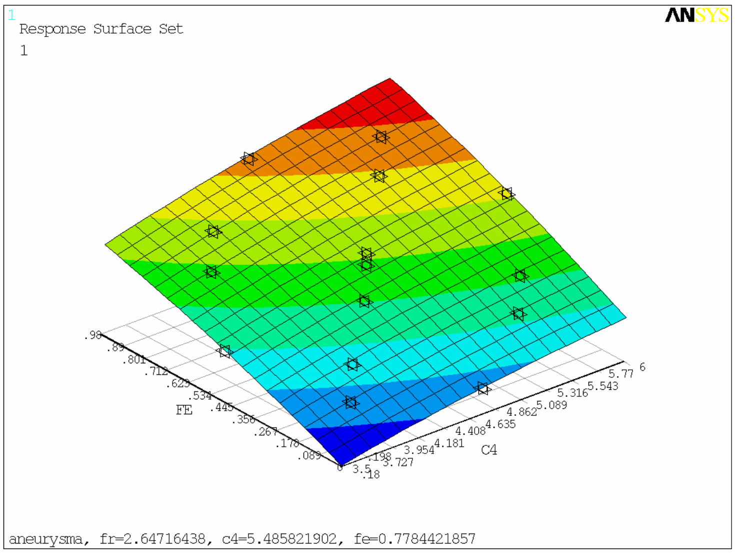

Figure 5-32 Response surface - maximum stress vs. F_E and c_4

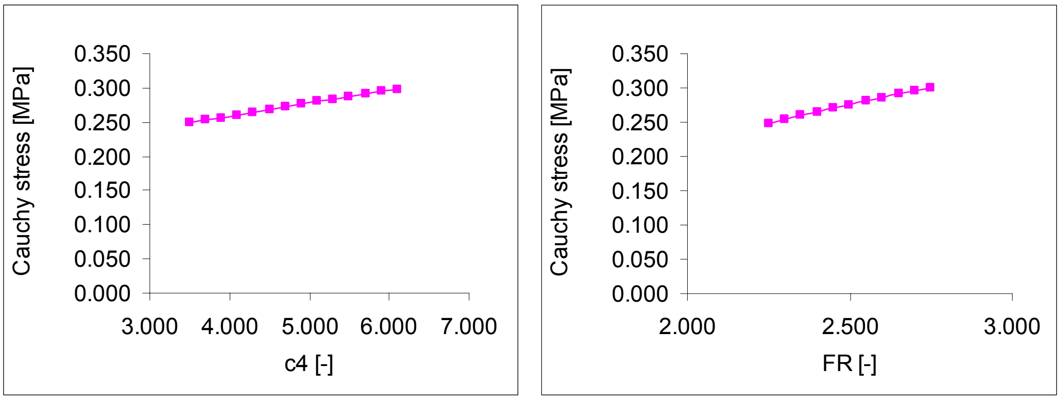

Figure 5-33 Maximum Cauchy stress vs. c_4 and F_R parameter [MPa]

The following two hypothetical aneurysms (Figure 5-34) were analysed using an analytical expression of the response surface. First (black line) aneurysm has its maximum diameter 45mm and the angle between AAA and nominal part α=111°. The second (red line) aneurysm has maximum diameter 50.1mm and the angle α=121°. From the analytical expression the maximum principal Cauchy stress in both AAAs is 280kPa. The stresses at both aneurysms were verified numerically using ANSYS and the maximum stresses are 272kPa and 269kPa (Figure 5-35). From this point of view the AAA with smaller diameter and higher skewness of transition part is dangerous like AAA with smaller skewness and higher maximum diameter.

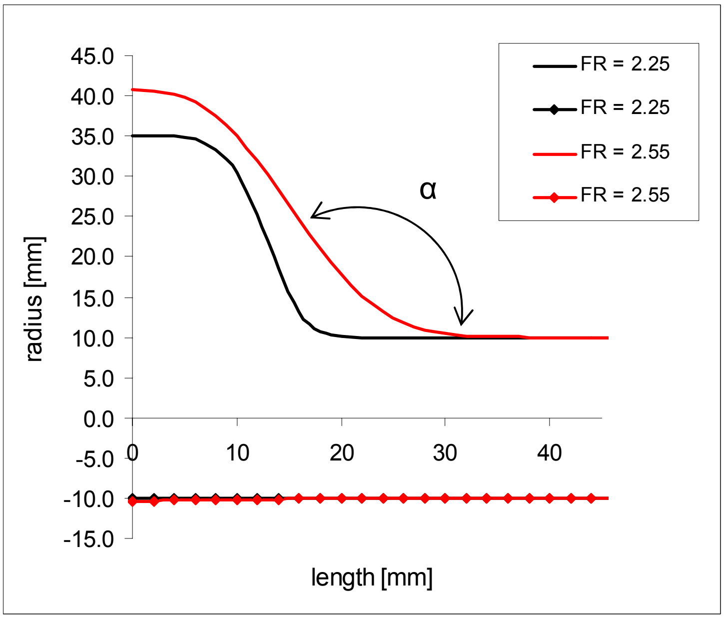

Figure 5-34 Two hypothetical aneurysms

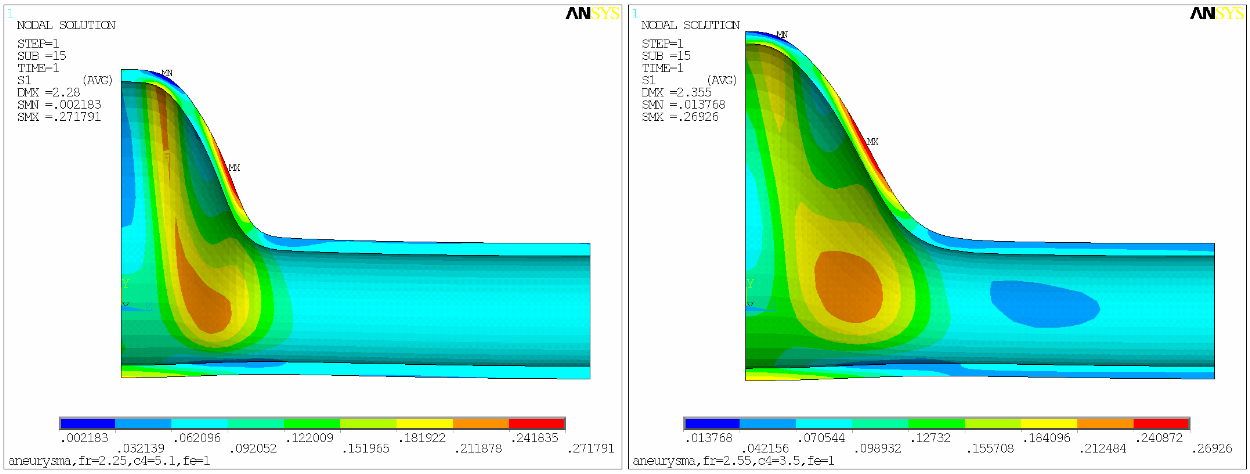

Figure 5-35 Contour plot of the maximum Cauchy principal stress [MPa]

5.5 Aneurysm model based on the patient-specific CTA data

As mentioned in chapter 5.3, in cooperation with St. Ann Hospital in Brno only CT scans were available for geometry reconstruction of the real human AAA. The 3D model was generated using software ProEngineer (Ryšavý [62]) from a series of scans that included abdominal aneurysm as well as parts of the proximal and distal healthy arteries (Figure 5-36 and Figure 5-37). The only out of AAA and normal artery wall surface from every scan was used for geometry reconstruction. In axial direction the outline profiles are connected by series of splines which are continues smooth curves. The Figure 5-38 and Figure 5-39 shows the wireframe and sufrace model.

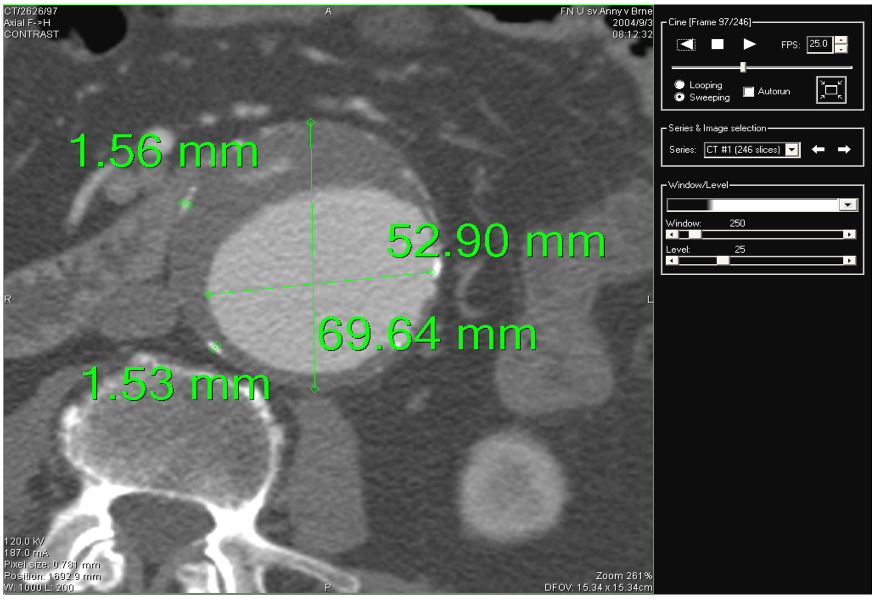

Figure 5-36 CT scan - abdominal aneurysm – (diameter and thickness) [62]

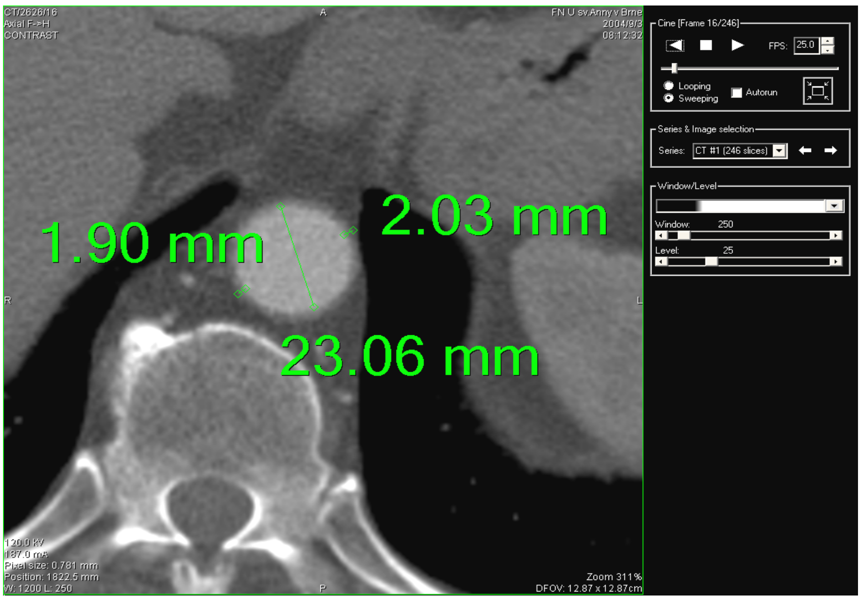

Figure 5-37 CT scan – healthy artery (diameter and thickness) [62]

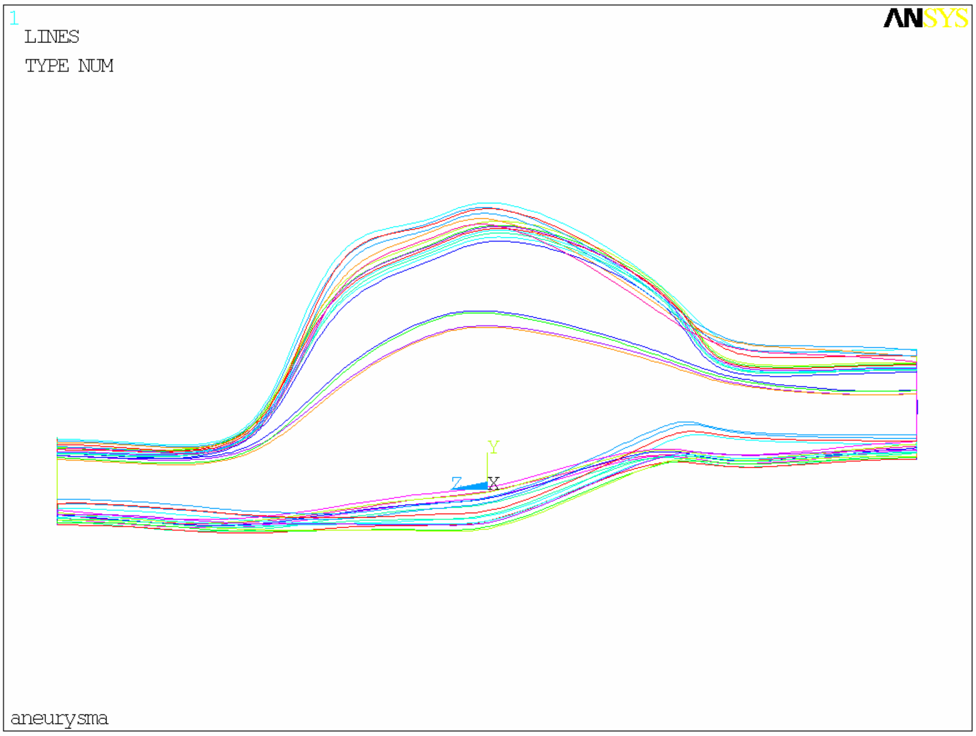

Figure 5-38 AAA wireframe model

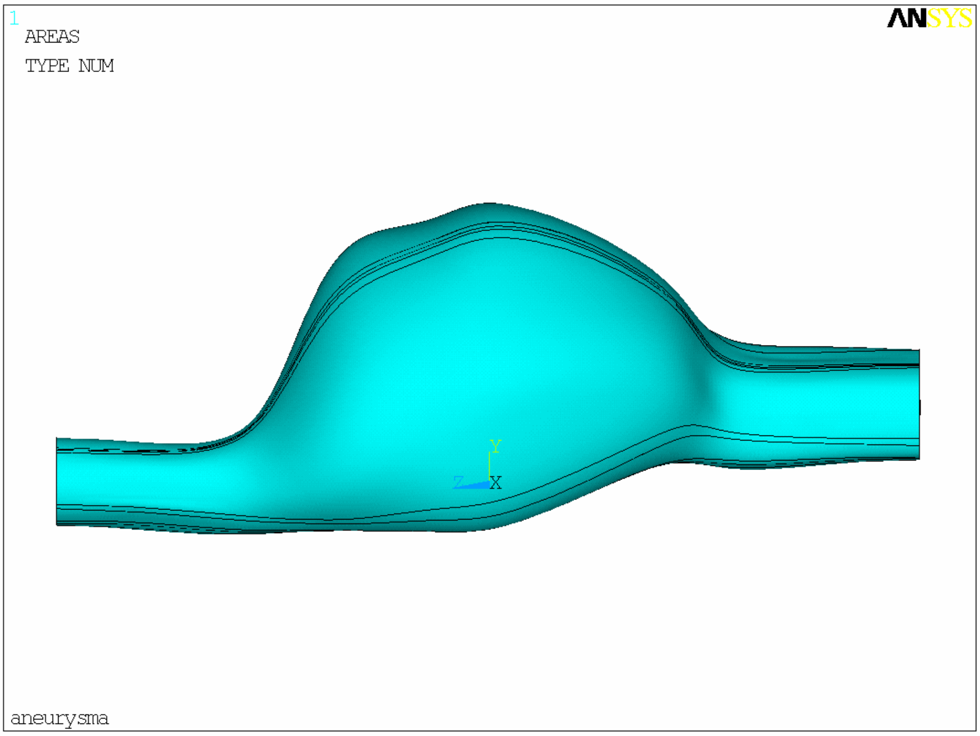

Figure 5-39 AAA surface model

5.5.1 Backward incremental method application in ANSYS

Generally the backward incremental method is based on the backward application of computed forward deformations. The algorithm used in this thesis is schematically depicted in Figure 5-40. The process of unloaded creation of the stress-free geometry consists of the following steps:

1. Definition of the internal pressure $\boldsymbol{P}$, number of pressure increment $\boldsymbol{k}$, pressure increment $\boldsymbol{\Delta P=P/k}$ and number of iterations $\boldsymbol{l}$
2. Applying pressure $\boldsymbol{k\times\Delta P=P_k}$ on the stress free geometry $\boldsymbol{X}$. In the described algorithm the pressure increment is constant. Putter [41], used a nonconstant pressure increment in the simulations, defined by:

$$P_k = P \cdot sin\left(\frac{n \cdot \pi}{2k}\right) \qquad 0 \le n \le k \tag{5-18}$$

   This pressure increment calculation was tested and compared in chapter 5.5.4.

   Tab. 11 Example of different pressure increment calculation

k	ΔP = const	Pk [kPa]	ΔP ≠ const	Pk [kPa]
1	8	8	11.31	11.31
2	8	16	4.69	16.00

3. Determining of the deformed geometry $\boldsymbol{x_k}$, displacement vector field $\boldsymbol{U_k}$ and create candidate zero pressure geometry $\boldsymbol{X_{0k}=X\text{-}f\times U_k}$ using mulfiplication factor $\boldsymbol{f}$. The value of multiplication factor is (-1×const). The constant in multiplication factor has no physical meaning and is used only for number of $\boldsymbol{l}$ iterations reduction. The constant was tested in the range 0.8 to 1.6 and the results are compared in chapter 5.5.4.
4. For anisotropic constitutive model updating the fiber direction at every element. This step is necessary because the fiber direction is defined in reference to global coordinate system and the position of elements change during the zero pressure geometry creation.
5. Applying pressure $\boldsymbol{P_k}$ and determining deformed geometry $\boldsymbol{x_{0k}}$.
6. Calculating objective function ***Eobj*** that calculate the average difference between original and evaluated „node“ coordinates.
7. If the prescribed value of objective function is achieved the algorithm stops the actual iteration and continues next of $\boldsymbol{k}$ iteration. If the value of objective function is not achieved, calculate residual displacement vector field $\boldsymbol{U_{0k}}$, create candidate zero pressure geometry $\boldsymbol{X_{lk}}$. For anisotropic constitutive model update fiber direction.
8. Applying pressure $\boldsymbol{P_k}$ and determining deformed geometry $\boldsymbol{x_{lk}}$ (then $\boldsymbol{x_{0k}}$ in the objective function changes to $\boldsymbol{x_{lk}}$).
9. If the prescribed value of the objective function is achieved, the algorithm stops and continues next $\boldsymbol{k}$ iteration. If the value is not achieved continues next $\boldsymbol{l}$ iteration.

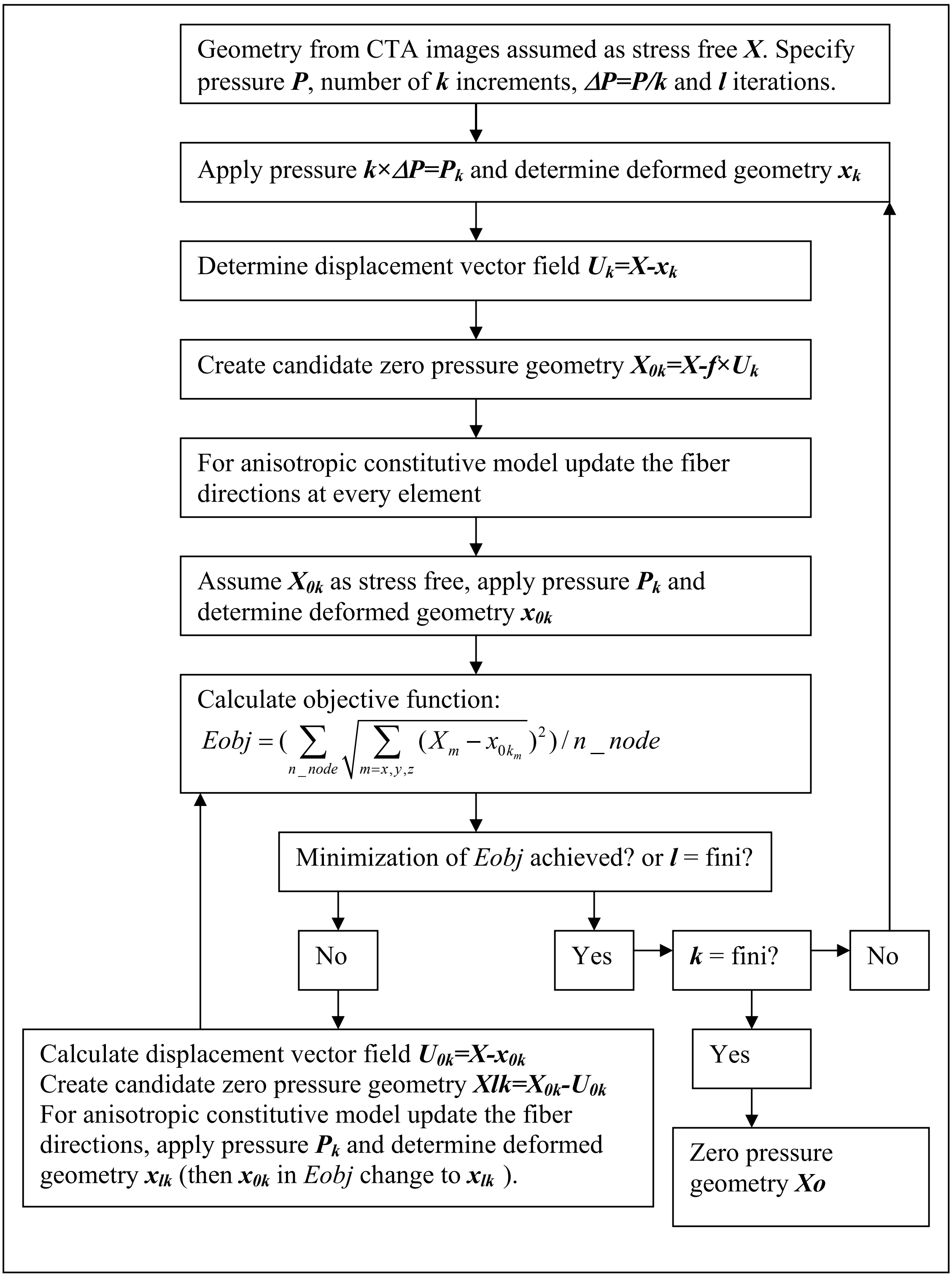

Figure 5-40 Backward incremental method algorithm

5.5.2 Verification of backward incremental method

For verification of the backward incremental method, the hypothetical idealised geometrical aneurysm model (5.4) was used. First the original model („A“ Figure 5-41) was loaded by the physiological pressure of 16kPa and the displacements at every nodes from the deformed state („B“ Figure 5-41) are added to the initial geometry („A“ Figure 5-41) using „*upgeom*“ command [63]. This operation creates deformed geometry as if obtained from CT scans („C“ Figure 5-41). Then the backward incremental method was applied on created deformed geometry („C“ Figure 5-41) to verification whether the presented algorithm is able to find unloaded original geometry („D“ Figure 5-41). The backward incremental method was tested for several constitutive models (Tab. 12) and several AAA thicknesses (Tab. 12). The thickness is considered .15mm and 1.9mm (chapter 5.3.2) for all models except for the anisotropic double-layer constitutive model where the total thickness is 2.28mm (0.96mm adventitia and 1.32mm media). The residual value of objective function ***Eobj*** was choosen 0.03mm and the pressure was applied at one step (***k***=1).

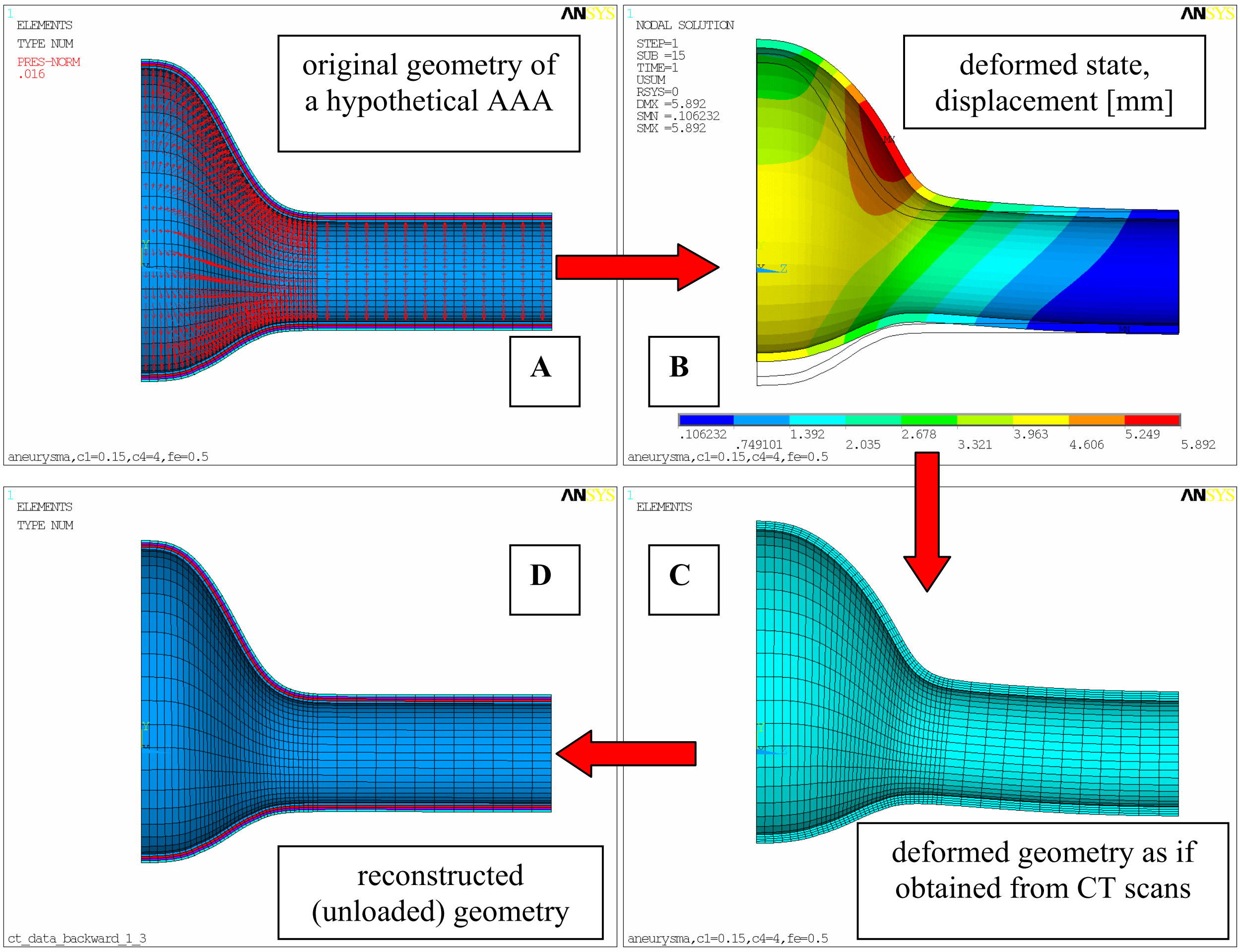

Figure 5-41 Verification of the backward incremental method

The following Tab. 12 summarizes constitutive models, input variables and the maximum principal Cauchy stress comparison between the original („A“ Figure 5-41) and reconstructed (unloaded) geometry („D“ Figure 5-41) after pressure loading. The difference between stresses is 2 - 4%. Consequently, the results show, that the presented algorithm of the backward incremental method is able to find unloaded geometry.

Tab. 12 Stress comparison between original and reconstructed (unloaded) geometry

constitutive model	AAA thickness [mm]	number of *I* iterations	average difference ***Eobj*** [mm]	maximum principal Cauchy stress [MPa]		difference [%]
				original geometry	reconstucted geometry	
Isotropic - Yeoh (5.3.3)	1.9 1.5	2 3	0.054 - 0.027 0.072 - 0.032 - 0.017	0.258 0.337	0.263 0.345	1.9 2.4
Isotropic (5.3.4)	1.9 1.5	1 1	0.009 0.014	0.268 0.330	0.261 0.321	2.6 2.7
Single-layer (5.3.4)	1.9 1.5	3 3	0.065 - 0.036 - 0.018 0.079 - 0.047 - 0.024	0.275 0.317	0.266 0.306	3.3 3.5
Double-layer (5.3.4)	2.28	3	0.079 - 0.059 - 0.024	0.499	0.517	3.6

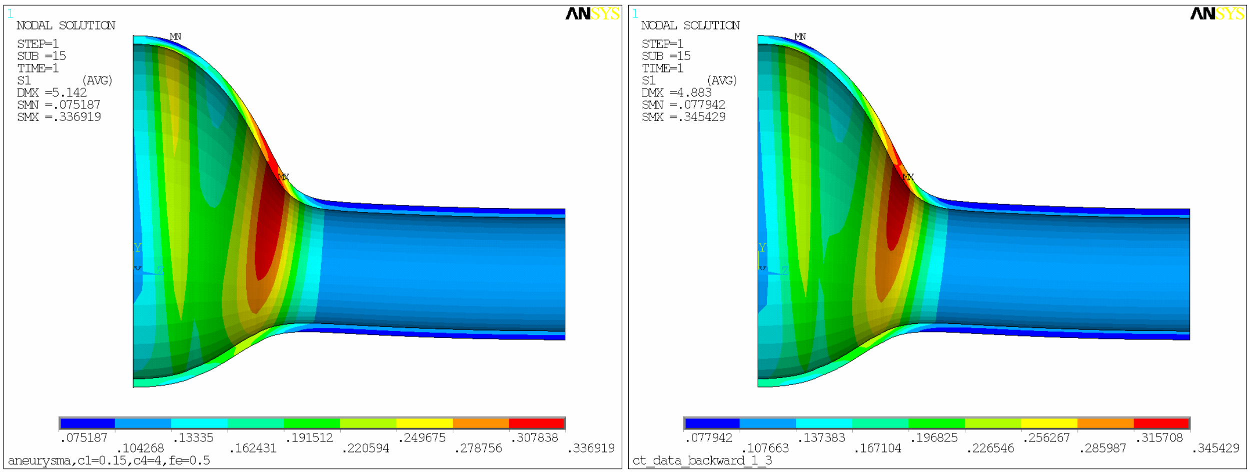

Figure 5-42 Maximum principal Cauchy stress [MPa] for original geometry (left) and reconstructed (unloaded) geometry (right) – Yeoh constitutive model (Tab. 12)

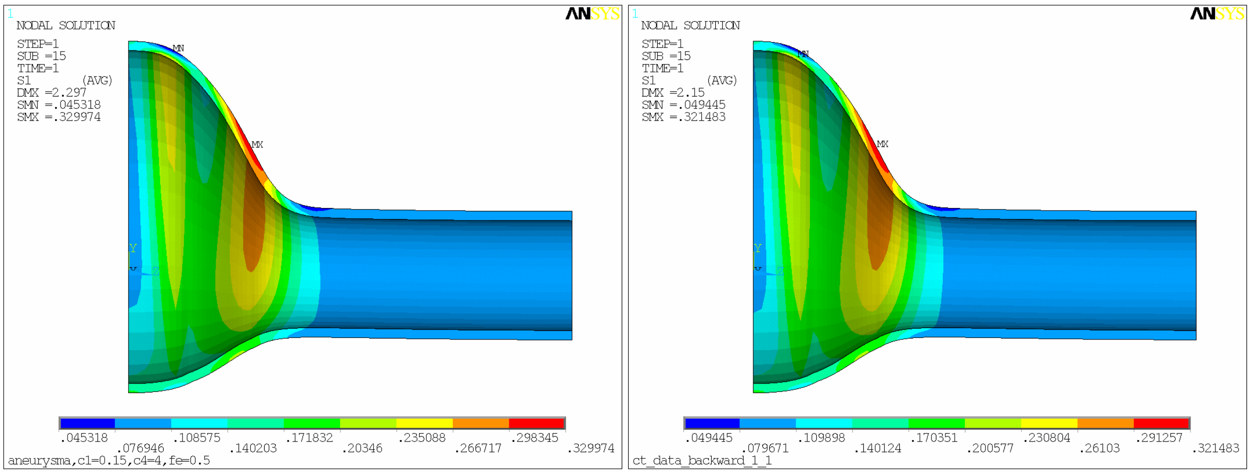

Figure 5-43 Maximum principal Cauchy stress [MPa for original geometry (left) and reconstructed (unloaded) geometry (right) - Isotropic constitutive model (Tab. 12)

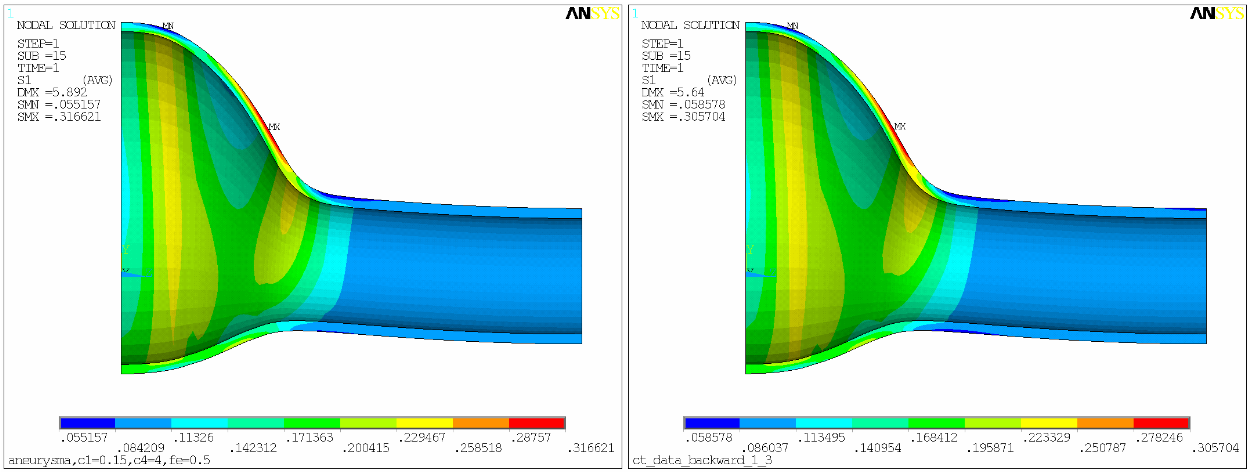

Figure 5-44 Maximum principal Cauchy stress [MPa] for original geometry (left) and reconstructed (unloaded) geometry (right) – Single-layer constitutive model (Tab. 12)

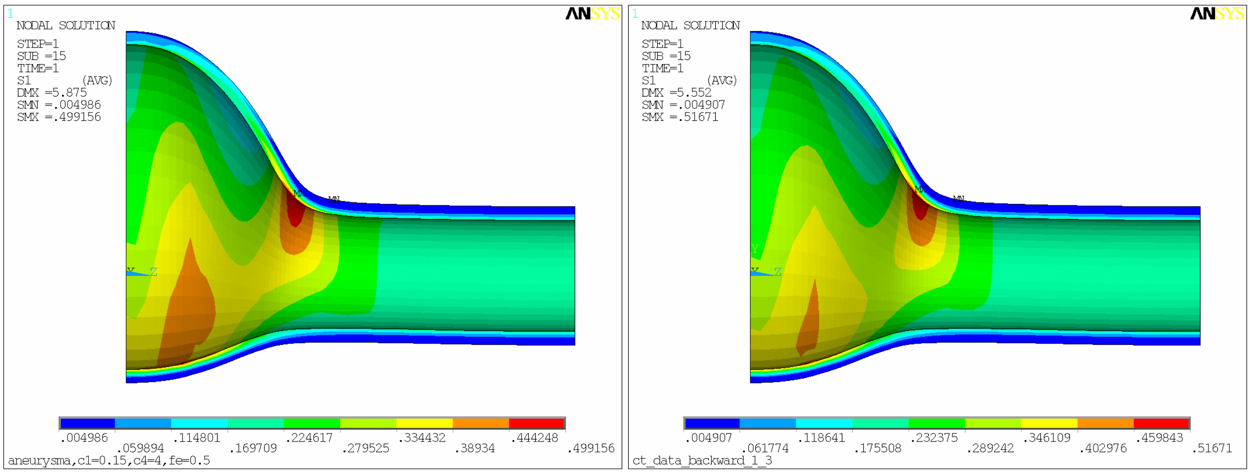

Figure 5-45 Maximum principal Cauchy stress [MPa] for original geometry (left) and reconstructed (unloaded) geometry (right) – Double-layer constitutive model (Tab. 12)

5.5.3 Finite element model of the real AAA geometry

Figure 5-46, Figure 5-47 and Figure 5-48 show a purely hexahedral finite element mesh with the prescribed boundary conditions and the orientation of collagen fibres in the anisotropic exponential constitutive model. Four elements through the thickness of the artery wall were used. For the anisotropic double-layer constitutive model two element through thickness are used for the adventitia layer and two for the media layer. The following boundary conditions were applied at the patient specific model of the the AAA. Axial displacement at both ends u_ax=0. Circumferential displacement u_circ=0 were prescribed for nodes at both ends of the model always in a specific local coordinate system. In this way only radial displacement of artery ends are enabled (Figure 5-48). The thickness is considered 1.9mm (chapter 5.3.2) for all models except for the anisotropic double-layer constitutive model where the total thickness is 2.28mm (0.96mm adventitia and 1.32mm media).

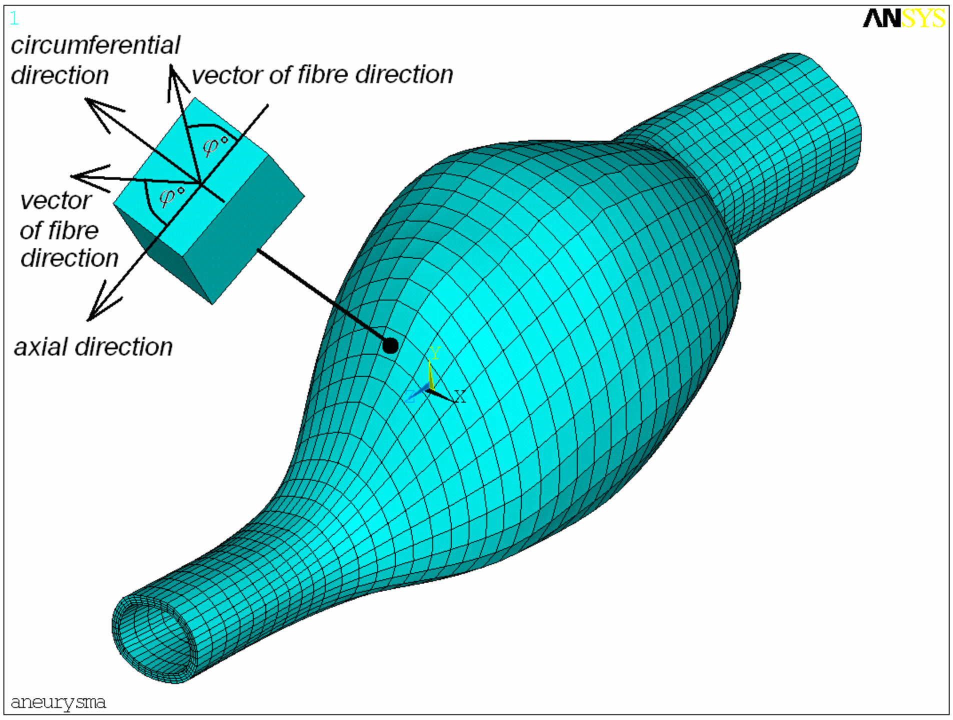

Figure 5-46 Finite element model of the patient-specific AAA

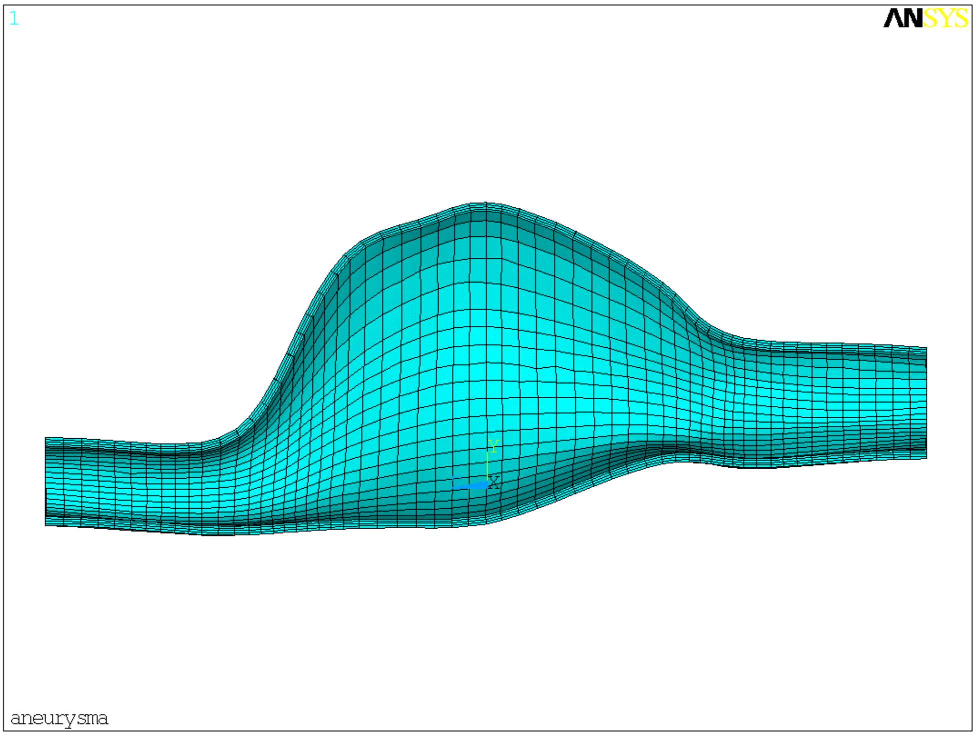

Figure 5-47 Finite element model of patient-specific AAA – sectional view

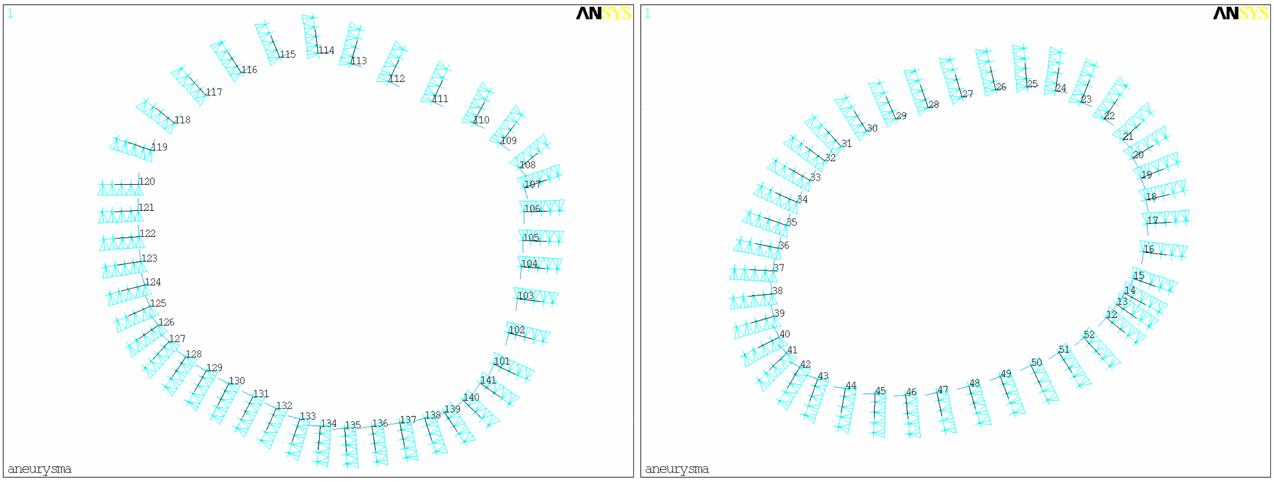

Figure 5-48 Circumferential boundary conditions applied at proximal (left) and distal (right) ends of the healthy aorta

5.5.4 Results

The influence of the multiplication factor ***f*** described in chapter 5.5.1 was tested for the isotropic exponential constitutive model in the range 0.8 to 1.6 [-] (Tab. 13 and Tab. 14). The results show that there are no significant differences in the number of ***l*** iterations. Neverthless it is suitable to select the ***f*** factor greater than or equal to 1. The influence in the pressure increment calculations (Tab. 11) are compared in Tab. 15 for 13kPa internal pressure and Tab. 16 for 16kPa internal pressure. The results also show that there are no significant differences between the mentioned pressure increment calculations. The isotropic Yeoh constitutive model was also tested for different ***f*** factor but in the comparison with the isotropic exponential model the residual average difference achieve high order values. The average difference is about 0.35mm (Tab. 17). The similar results are achieved for anisotropic single-layer or double-layer constitutive model where the ***f***-factor was used 1.1 and the resulting residual average differences are 0.44mm (Tab. 18) and 1.02mm (Tab. 19) respectively. The residual average difference 1.02mm (using double-layer constitutive model) is due to small number of ***l*** iterations which is two in this case. The geometry update in additional 3rd ***l*** iteration causes an intersection in the nominal part of the artery (Figure 5-49) therefore the backward incremental algorithm is not able to find better unloaded geometry using this constitutive model.

Tab. 13 ***f***-factor comparison (13kPa) – isotropic exponential constitutive model

	Isotropic constitutive exponential model, internal pressure 13kPa average difference *Eobj* [mm]								
	f - factor								
l - iteration	0.8	0.9	1.0	1.1	1.2	1.3	1.4	1.5	1.6
1	0.16354	0.15410	0.14469	0.13522	0.12579	0.11655	0.10779	0.09995	0.09328
2	0.10363	0.09862	0.09366	0.08879	0.08390	0.07912	0.07445	0.06990	0.06557
3	0.06856	0.06556	0.06259	0.05966	0.05677	0.05391	0.05111	0.04834	0.04565
4	0.04657	0.04463	0.04270	0.04080	0.03890	0.03704	0.03519	0.03338	0.03159
5	0.03207	0.03079	0.02951	0.02823	0.02697	0.02573	0.02450	0.02328	0.02207
6	0.02235	0.02148							
Max. stress [MPa]	0.824	0.825	0.817	0.818	0.820	0.821	0.822	0.823	0.825

Tab. 14 ***f***-factor comparison (16kPa) – isotropic exponential constitutive model

	Isotropic constitutive exponential model, internal pressure 16kPa average difference *Eobj* [mm]								
	f - factor								
l - iteration	0.8	0.9	1.0	1.1	1.2	1.3	1.4	1.5	1.6
1	0.20083	0.19100	0.18107	0.17108	0.16112	0.15129	0.14180	0.13308	0.12552
2	0.13645	0.13097	0.12552	0.12010	0.11474	0.10944	0.10422	0.09910	0.09411
3	0.09687	0.09348	0.09012	0.08681	0.08353	0.08030	0.07711	0.07396	0.07087
4	0.07099	0.06865	0.06633	0.06402	0.06173	0.05945	0.05720	0.05498	0.05278
5	0.05272	0.05104	0.04938	0.04772	0.04607	0.04442	0.04280	0.04119	0.03959
6	0.03952	0.03831	0.03710	0.03590	0.03471	0.03353	0.03236	0.03119	0.02966
7	0.02991	0.02902	0.02815	0.02727	0.02640	0.02554	0.02469	0.02384	
Max. stress [MPa]	1.047	1.048	1.050	1.051	1.053	1.054	1.056	1.057	1.047

Tab. 15 **ΔP** comparison (13kPa)

	average difference *Eobj* [mm]			
	f - factor = 1.2			
	ΔP = const		ΔP ≠ const	
	k - iteration		*k* - iteration	
l - iteration	1	2	1	2
1	0.04504	0.05667	0.07849	0.03441
2	0.02335	0.03718	0.04647	0.01892
3		0.02602	0.02772	
Max. stress [MPa]		0.820		0.828

Tab. 16 **ΔP** comparison (16kPa)

	average difference *Eobj* [mm]			
	f - factor = 1.2			
	ΔP = const		ΔP ≠ const	
	k - iteration		*k* - iteration	
l - iteration	1	2	1	2
1	0.06350	0.07818	0.10509	0.05356
2	0.03572	0.05231	0.06693	0.02852
3	0.02021	0.03904	0.04309	
4		0.02937	0.02811	
Max. stress [MPa]		1.053		1.048

Tab. 17 ***f***-factor comparison – Yeoh constitutive model

	Isotropic Yeoh constitutive model average difference *Eobj* [mm]			
	f - factor			
l - iteration	1.1	1.2	1.2	1.4
1	0.43140	0.42470	0.42470	0.41430
2	0.38650	0.38175	0.38175	0.37160
3	0.35900	0.35831	0.35831	0.35830
Max. stress [MPa]	1.337	1.349	1.361	1.375

Tab. 18 Single-layer anisotropic constitutive model

Anisotropic constitutive single-layer model average difference *Eobj* [mm]	
l - iteration	*f* - factor = 1.1
1	0.50811
2	0.45905
3	0.43812
Max. stress [MPa]	1.116

Tab. 19 Double-layer anisotropic constitutive model

Anisotropic constitutive double-layer model average difference *Eobj* [mm]	
l - iteration	*f* - factor = 1.1
1	1.11390
2	1.02210
Max. stress [MPa]	1.360

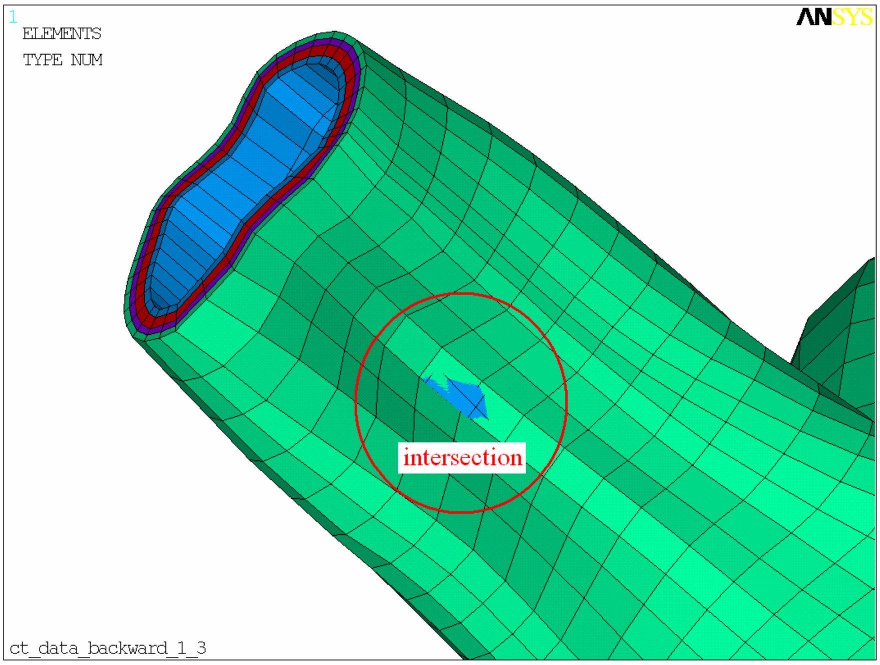

Figure 5-49 Intersection in the reconstructed (unloaded) geometry

The reconstructed (unloaded) and deformed (obtained from CT scans) configurations for the individual constitutive models are shown in Figure 5-50 to Figure 5-53 through the several cross-sections in different locations (1 to 7). It is evident that the reconstructed (unloaded) geometry strongly depends on the used constitutive model used. For example, the isotropic exponential constitutive model (Figure 5-50) gives a different unloaded configuration in contrast to the anisotropic single-layer exponential model (Figure 5-52) which was used for the evaluations of the isotropic model parameters (5.3.4). Therefore the identification of the parameters from the experimental data (where the anisotropy of the material is evident) by isotropic model conductes to a different reconstructed unloaded geometry. From the point of view of maximum wall stress (Tab. 21) the relative difference in stresses is 6% (1.051 MPa for the isotropic model vs. 1.116 MPa for the anisotropic model) for the physiological range of loading (16kPa). For higher loads (e.g. hypetension of 21kPa), the stress difference is approximately 3% therefore the impact of the different geometries has not essential influence on the resulting stress response. The reconstructed (unloaded) geometry for the anisotropic double-layer exponential constitutive model is highly diferent, even if a significant stiffening is evident (Figure 5-18) in comparison with the other constitutive models (Figure 5-14, Figure 5-15 and Figure 5-16). On the contrary the stiffness in the lower strain region is lower than with the other constitutive models. An explanation is related to the lower stiffness at the beginning of the loading, where radical changes in the geometry occur. From the point of view of the resulting residual average differences, the results show also that the reconstruction process may not be successful in any case, e.g. in the case of above mentioned anisotropic double-layer constitutive model where an intersection occurred (Figure 5-49). Considering these results the double-layer constitutive model of the AAA contributes to more credible simulation of the AAA behavior.

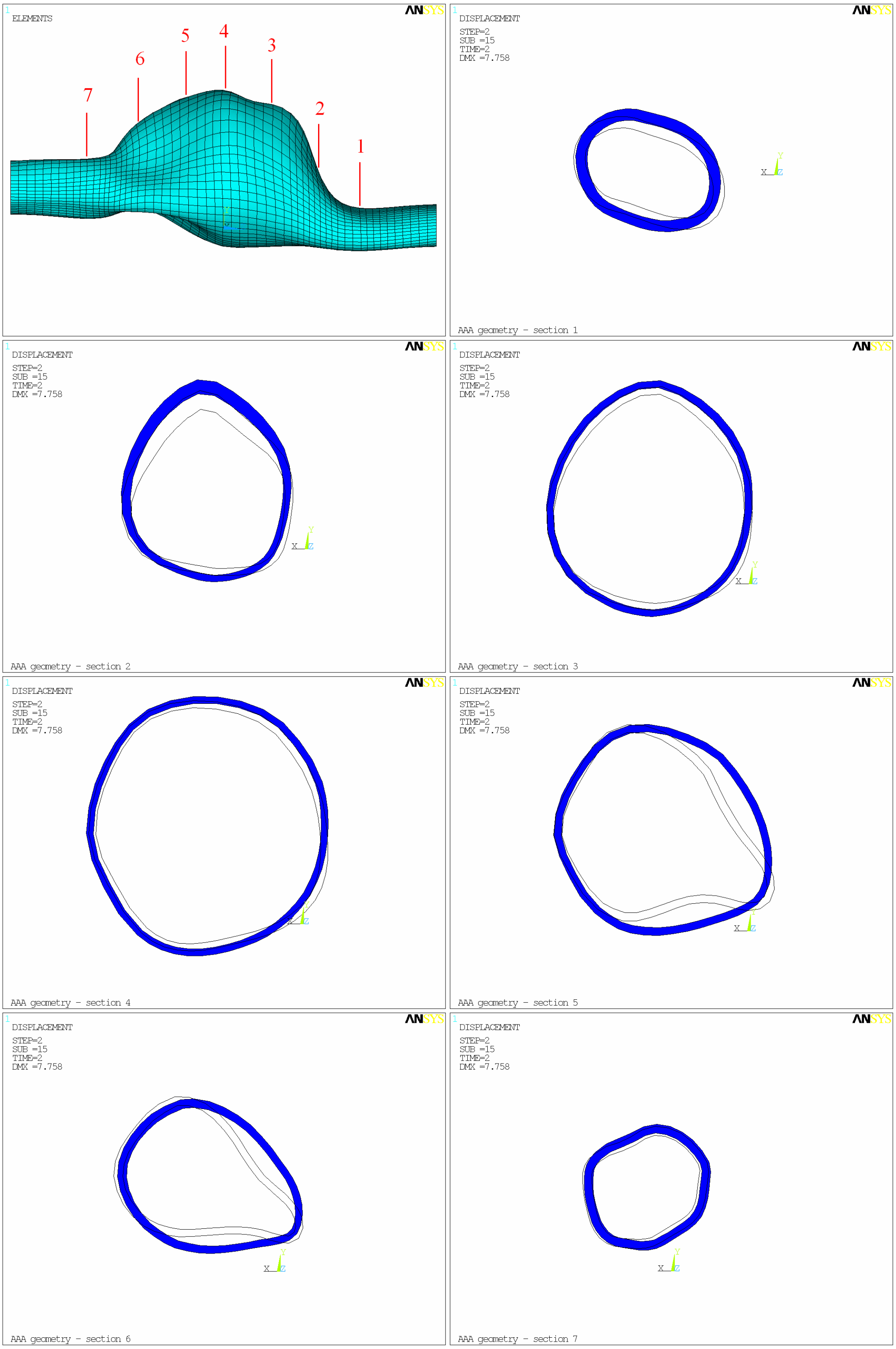

Figure 5-50 Reconstructed (unloaded) and deformed (from CT scans) geometry – isotropic exponential constitutive model

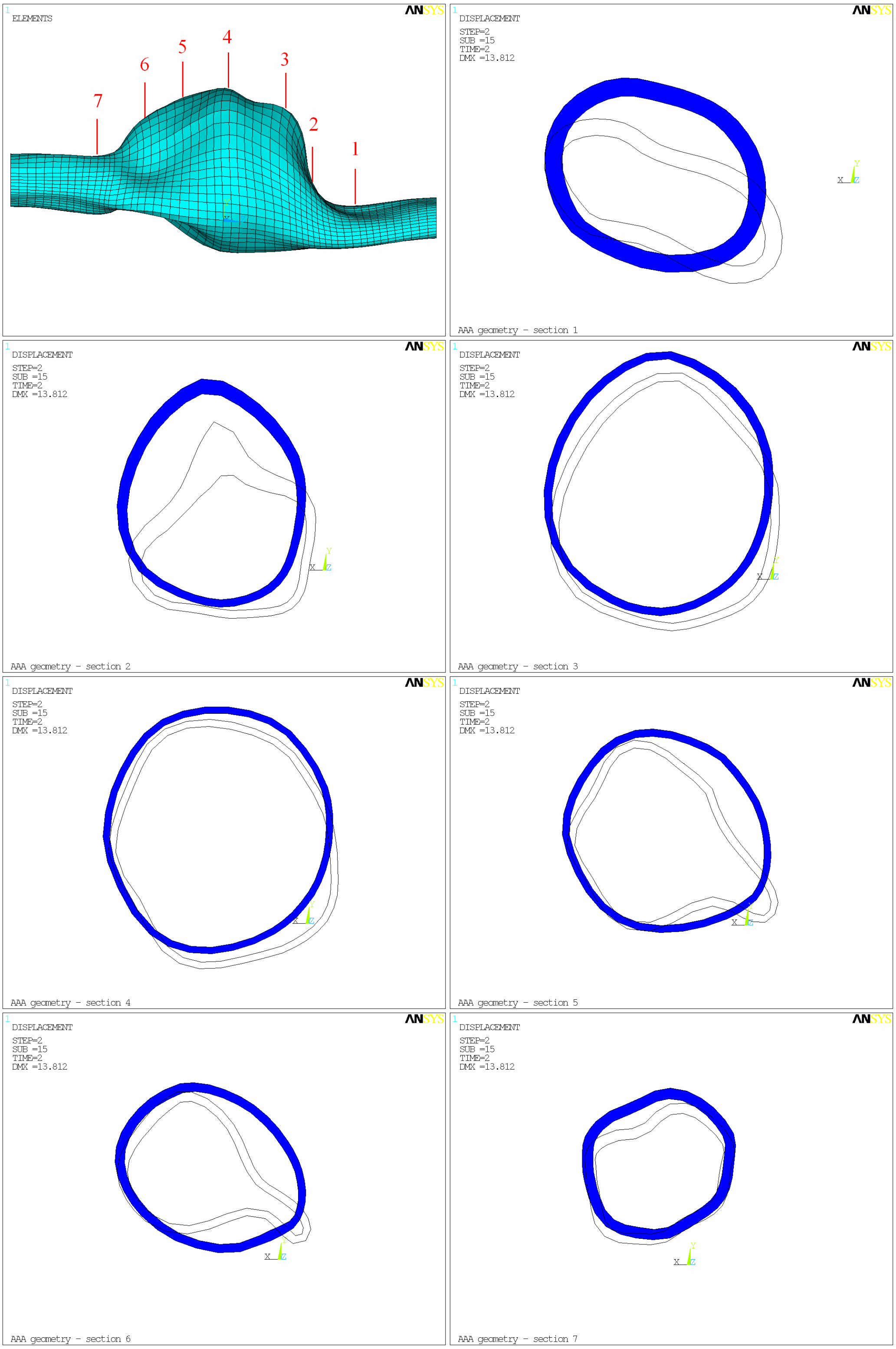

Figure 5-51 Reconstructed (unloaded) and deformed (from CT scans) geometry – isotropic Yeoh constitutive model

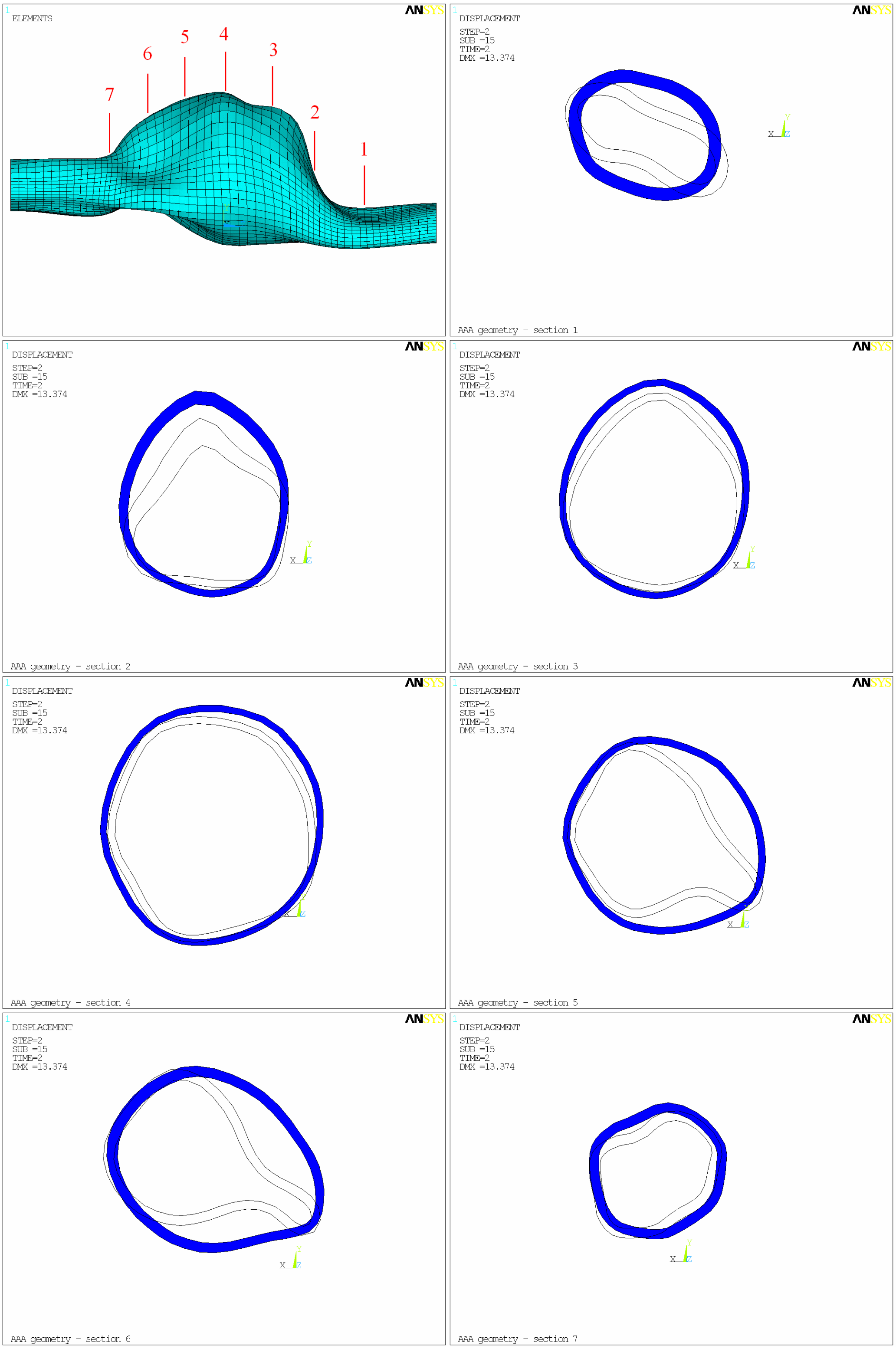

Figure 5-52 Reconstructed (unloaded) and deformed (from CT scans) geometry – anisotropic single-layer exponential model

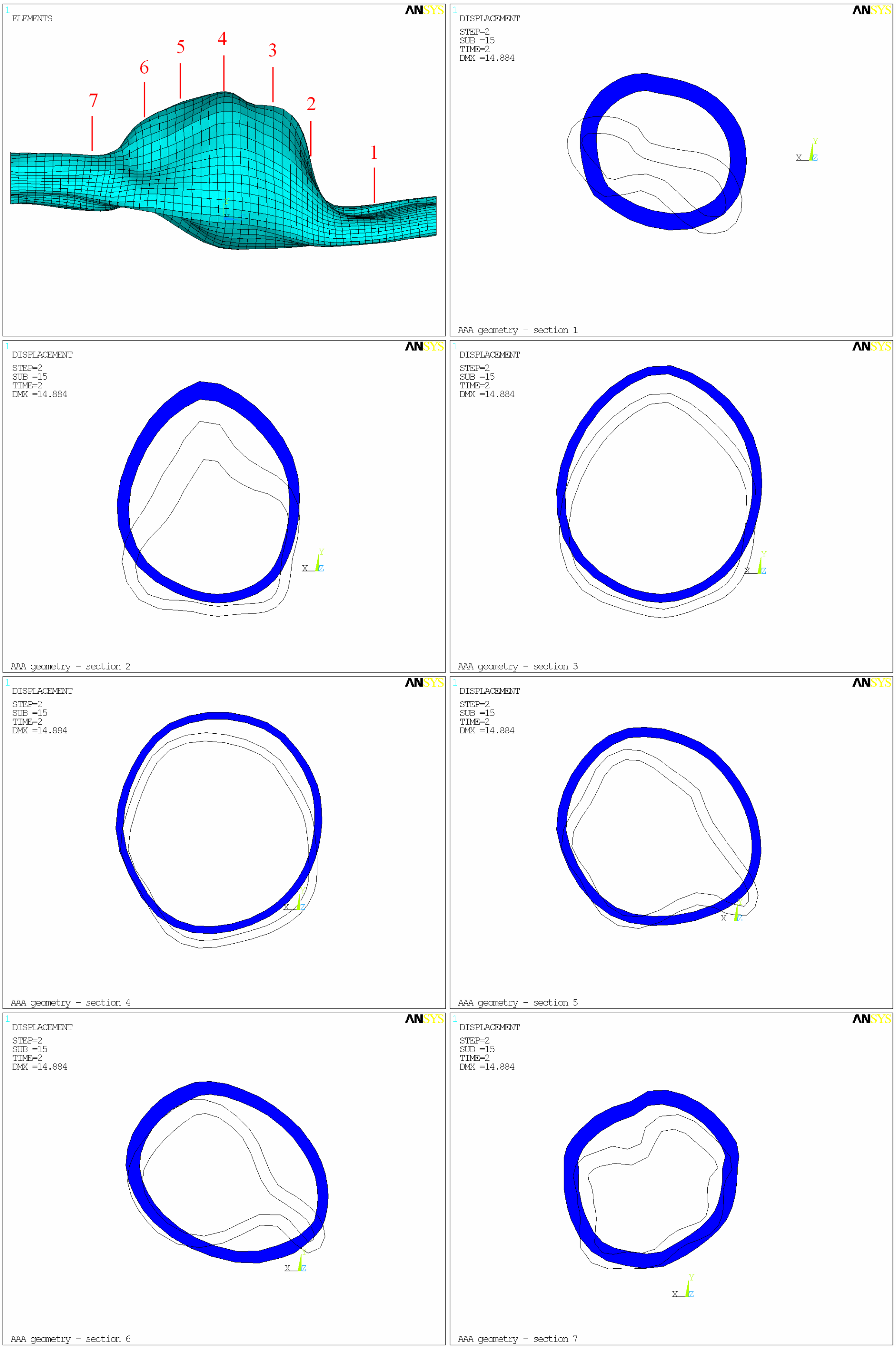

Figure 5-53 Reconstructed (unloaded) and deformed (from CT scans) geometry – anisotropic double-layer exponential model

5.6 Simulation of hypertension

As mentioned in chapter 1.3.1 clinically, the hypertension is considered to be a one of the key factors contributing to AAA rupture. This rupture risk criterion was simulated in this chapter.

5.6.1 Finite element model

The influence of hypertension was simulated using reconstructed (unloaded) geometry of the real AAA geometry described in the previous chapter 5.5 using all considered constitutive models and the same boundary conditions. The range of the pressure loading was considered from 100mmHg (13kPa) to 160mmHg (21kPa) (see Tab. 20).

Tab. 20 Classification of hypertension [73]

Classification	Systolic pressure		Diastolic pressure	
	mmHg	kPa	mmHg	kPa
Normal	90–119	12–15.9	60–79	8.0–10.5
Prehypertension	120–139	16.0–18.5	80–89	10.7–11.9
Stage 1	140–159	18.7–21.2	90–99	12.0–13.2
Stage 2	≥160	≥21.3	≥100	≥13.3
Isolated systolic hypertension	≥140	≥18.7	<90	<12.0
Source: American Heart Association (2003)				

5.6.2 Results

The Tab. 21 summarizes stress comparison between individual constitutive models. The highest maximum principal Cauchy stress occur using isotropic Yeoh model (Figure 5-55) and anisotropic double-layer model (1.74 MPa) but this value is localizated and concentrated. The second critical location using this anisotropic double-layer model is nearly in the same location as achieved using other constitutive models but closer to the maximum diameter location. For all constitutive models the maximum principal stress occurs at the circumferential direction (Figure 5-54).

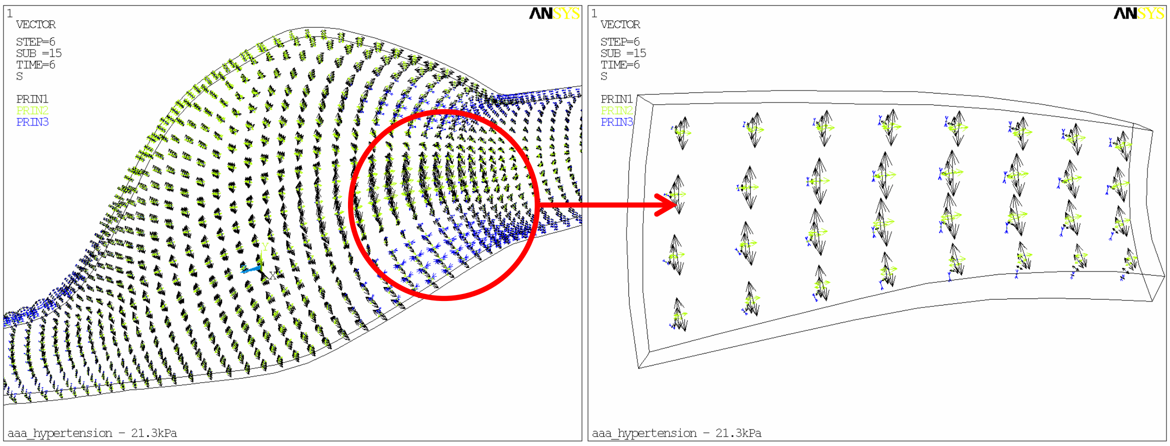

Figure 5-54 Vector plot of principal stresses (left) and detail of the critical area (right)

The influence of the element size and shape on the stress response was eliminated using stress-linearizing [63] (see *note below the Tab. 22) through the AAA thickness at the critical location. For the linearized stress "*membrane+bending*" stress components were considered. From this point of view the higher stress occurs when using both isotropic constitutive models (Figure 5-56).

The comparison of the longitudinal (axial) stresses is in the Tab. 22 and shown on the Figure 5-57 and Figure 5-58. The critical location is the same as for the circumferential stress. The critical location computed using the anisotropic double-layer constitutive model is in the maximum diameter location. As mentioned in chapter 5.3.1 the ultimate strength of the thoracic aorta wall is a lower in the longitudinal direction. The ultimate stress for the longitudinal direction was derived from the results using thoracic aortas. The estimated mean value of the ultimate stress was computed as:

$$\sigma_{ult} = 0.864MPa \times 1.15 = 0.994MPa \tag{5-19}$$

where 0.864MPa is the mean value of the ultimate Cauchy stress for AAA_{long} specimens (5.3.1) and 1.15 is ratio of breaking stress from biaxial vs. uniaxial tension test (5.3.1). This ultimate stress was not verified experimentally therefore the real value can be quite different. Only for comparison pupose and considering these condions the computed stresses are lower than the ultimate value for all of the constitutive models used.

Some of the general assumptions (5.1) need to be also mentioned. First of all, residual stress in the AAA wall stress analyses was not accounted for. Residual stress can be estimated through the opening angle of an artery sample but unfortunately, no methods are currently available to incorporate this phenomenon in AAA wall stress analyses. The Intra-luminal thrombus and local calcifications are not modeled because it is difficult to include them in the FEA model and to specify the interactions with the AAA wall. These phenomena also have not negligible effect on the resulting wall stress and should be accounted for in future AAA wall stress analyses.

The AAA FEA models and all wall stress results are showed on the Figure 5-59 through Figure 5-71.

Tab. 21 Stress comparison for individual constitutive models – circumferential stresses

h [mmHg]	press [MPa]	Circumferential Cauchy stress [MPa]				
		Isotropic - exp	isotropic - Yeoh	aniso single-layer	aniso double-layer (first location)	aniso double-layer (second location)
100	0.013	0.897	1.093	0.971	1.134	0.959
120	0.016	1.051	1.337	1.116	1.360	1.146
130	0.017	1.113	1.439	1.174	1.456	1.223
140	0.019	1.179	1.547	1.235	1.557	1.304
150	0.020	1.238	1.643	1.290	1.649	1.375
160	0.021	1.296	1.738	1.343	1.740	1.436
h [mmHg]	press [MPa]	Circumferential Cauchy stress - membrane+bending [MPa]				
100	0.013	0.861	0.851	0.680	0.550	0.532
120	0.016	1.004	1.035	0.788	0.663	0.643
130	0.017	1.060	1.109	0.834	0.710	0.690
140	0.019	1.118	1.186	0.883	0.761	0.744
150	0.020	1.170	1.255	0.928	0.808	0.797
160	0.021	1.220	1.323	0.971	0.854	0.848

Tab. 22 Stress comparison for individual constitutive models – axial stresses

h [mm] Hg	press [MPa]	Cauchy stress - axial direction [MPa]			
		isotropic	isotropic - Yeoh	aniso single-layer	aniso double-layer
100	0.000	0.463	0.486	0.443	0.375
120	0.000	0.520	0.571	0.486	0.462
130	0.000	0.541	0.604	0.504	0.500
140	0.000	0.563	0.637	0.523	0.541
150	0.000	0.581	0.667	0.539	0.579
160	0.000	0.599	0.695	0.554	0.617
h [mm] Hg	press [MPa]	Cauchy stress - axial direction (membrane+bending) [MPa]			
100	0.000	0.432	0.461	0.365	0.306
120	0.000	0.485	0.540	0.408	0.378
130	0.000	0.505	0.571	0.426	0.409
140	0.000	0.525	0.602	0.444	0.443
150	0.000	0.543	0.629	0.461	0.474
160	0.000	0.559	0.656	0.478	0.505

*note: The finite element stress distribution includes local effect due to mesh quality etc. However the forces have to balance in a Finite Element model regardless of the mesh size used. The purpose of stress linearization is to obtain the nominal (membrane or average) stress along path (wall thickness) and bending stress (the difference in stress from inside to outside node of the path) across a section. The procedure is to integrate the stress distribution through the section to get the equivalent normal force and bending moment and then calculate the equivalent membrane stress and bending stress. Membrane+bending stress is the sum of above two terms. Total stress is just the finite element stress on the surface including local effect. The stress linearization is intended for the strength evaluation.

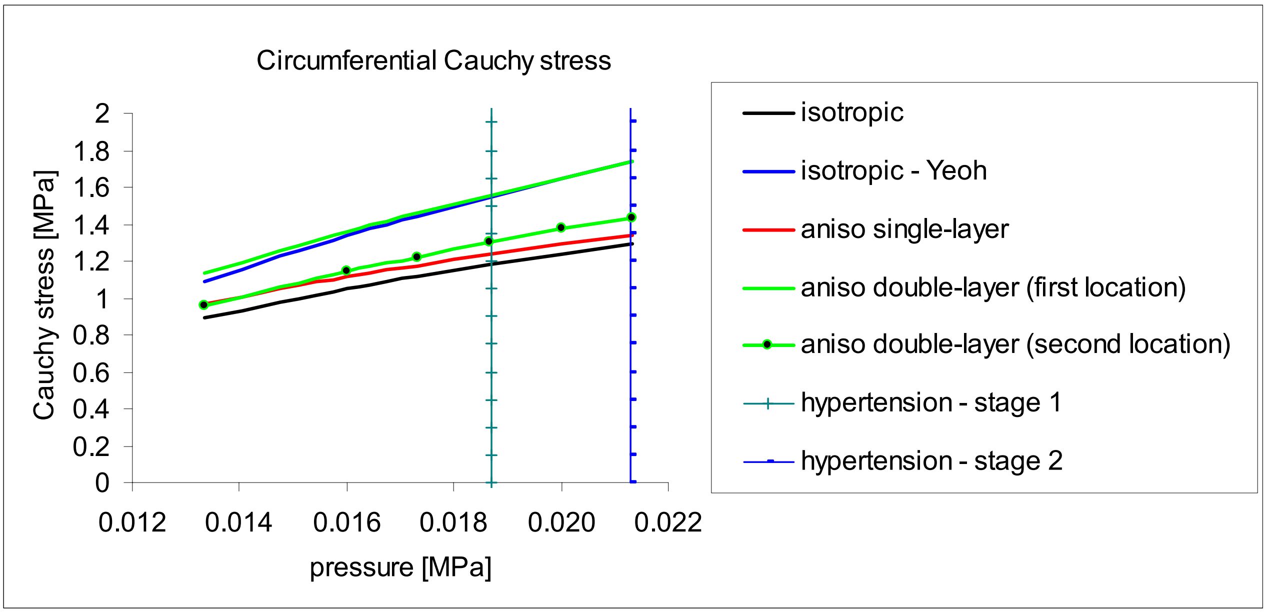

Figure 5-55 Circumferential Cauchy stress [MPa]

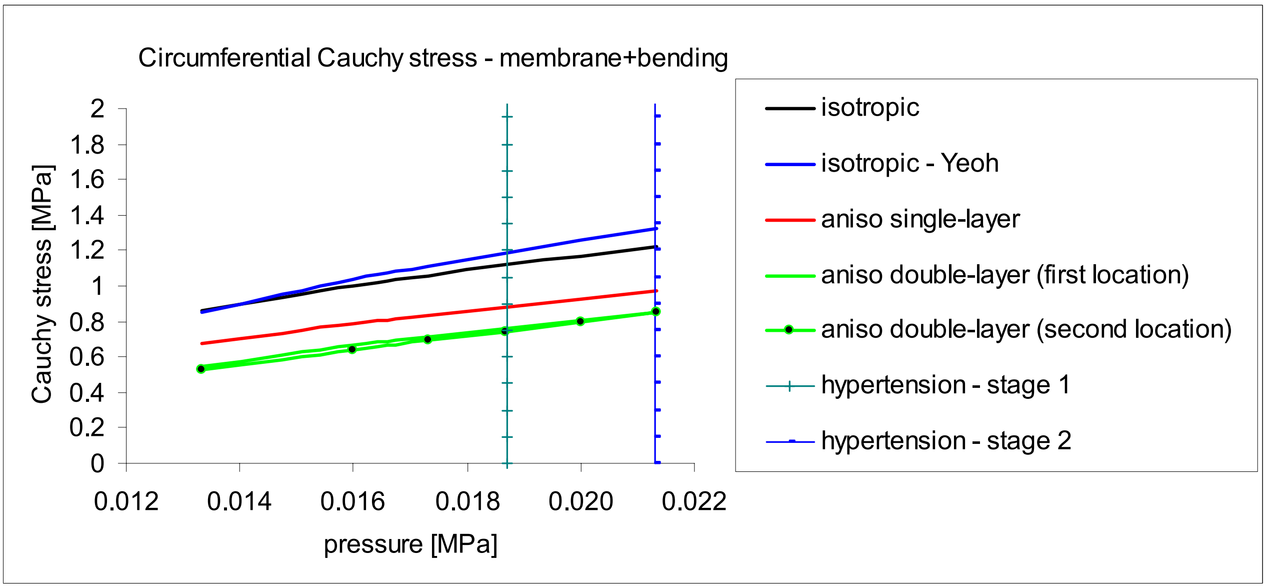

Figure 5-56 Circumferential linearized “membrane+bending” stress [MPa]

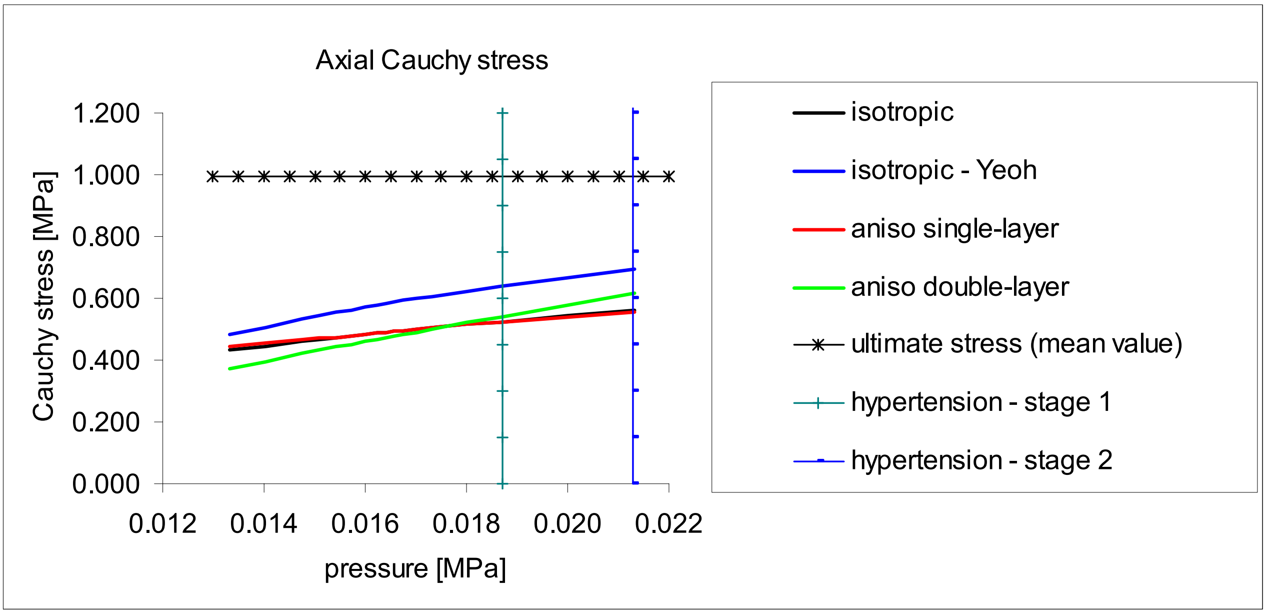

Figure 5-57 Axial Cauchy stress [MPa]

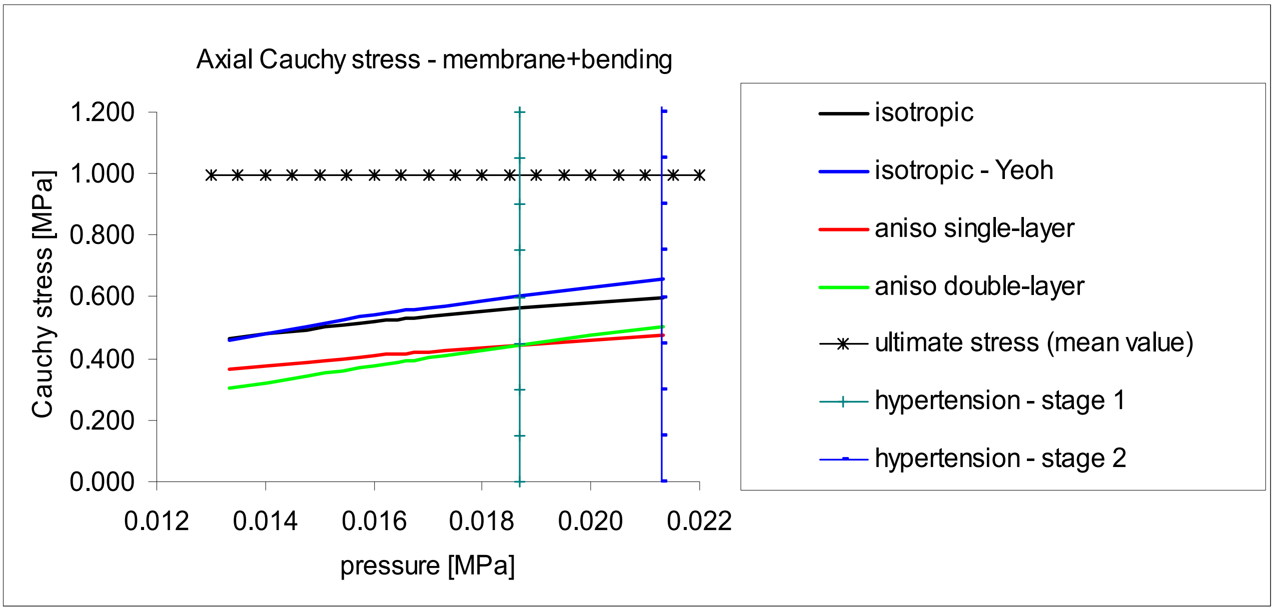

Figure 5-58 Axial linearized “membrane+bending” stress [MPa]

- isotropic constitutive exponential model

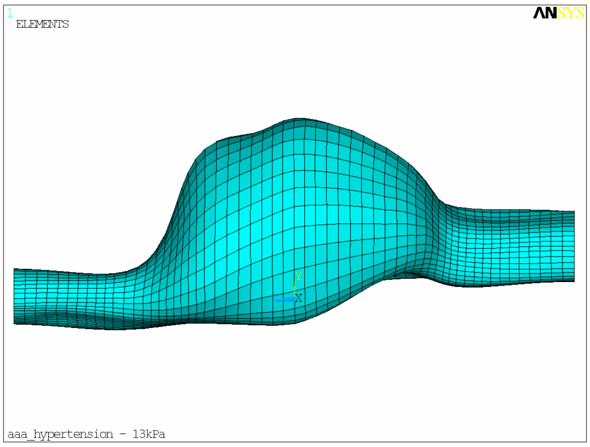

Figure 5-59 FEA mesh

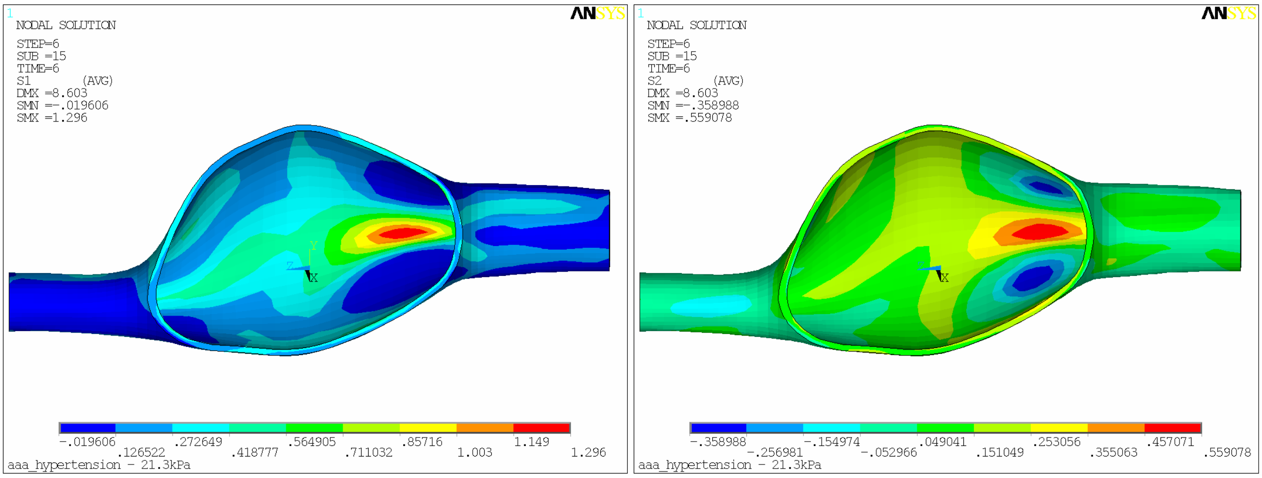

Figure 5-60 Contour plot of the circumferential (left) and axial (right) Cauchy stresses [MPa]

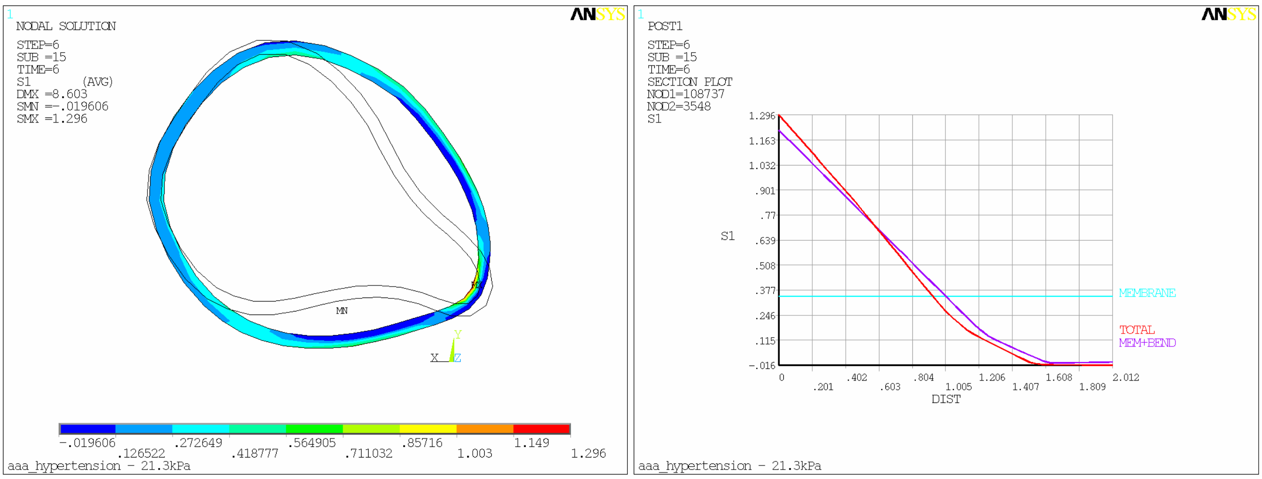

Figure 5-61 Maximum principal stress in cross-section (left) and linearized circumferential (right) Cauchy stress [MPa] through artery thickness at critical location

- isotropic Yeoh constitutive model

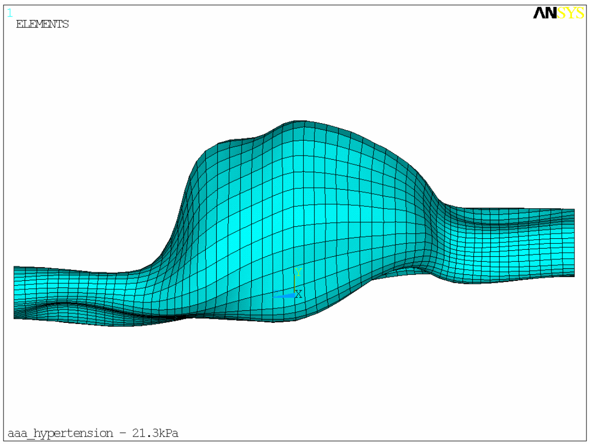

Figure 5-62 FEA mesh

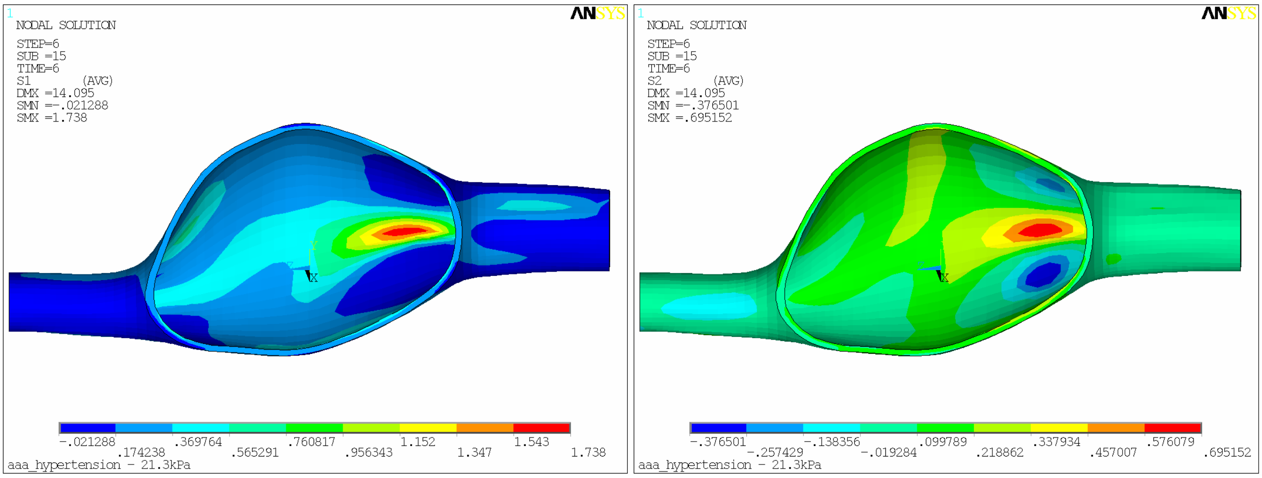

Figure 5-63 Contour plot of the circumferential (left) and axial (right) Cauchy stresses [MPa]

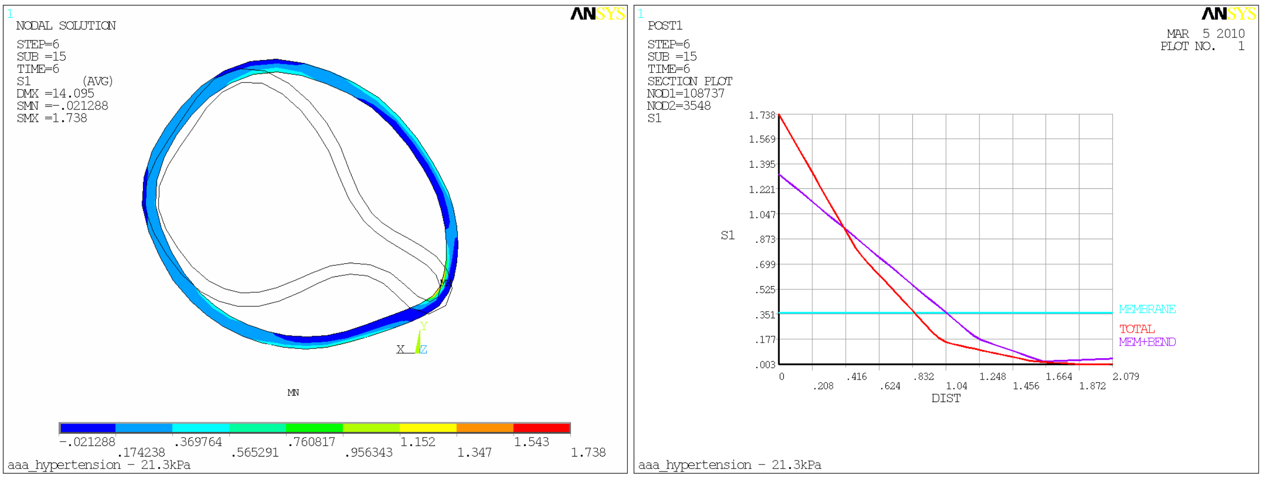

Figure 5-64 Maximum principal stress in cross-section (left) and linearized circumferential (right) Cauchy stress [MPa] through artery thickness at critical location

- anisotropic single-layer exponential constitutive model

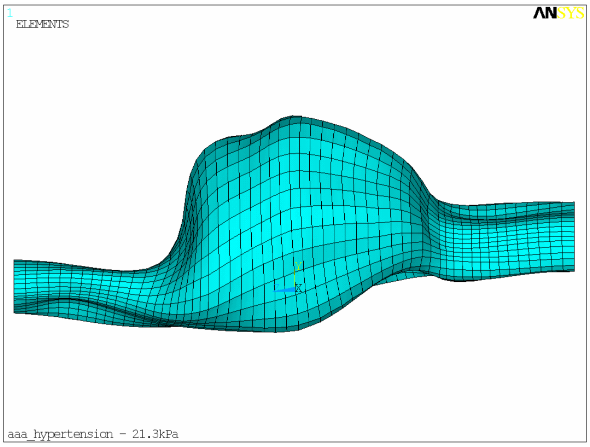

Figure 5-65 FEA mesh

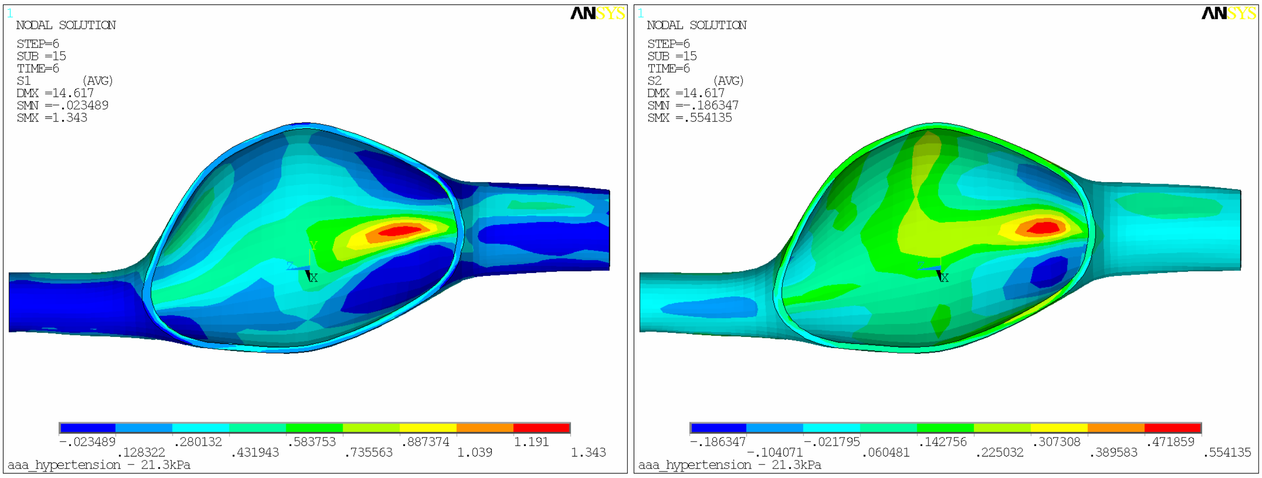

Figure 5-66 Contour plot of the circumferential (left) and axial (right) Cauchy stresses [MPa]

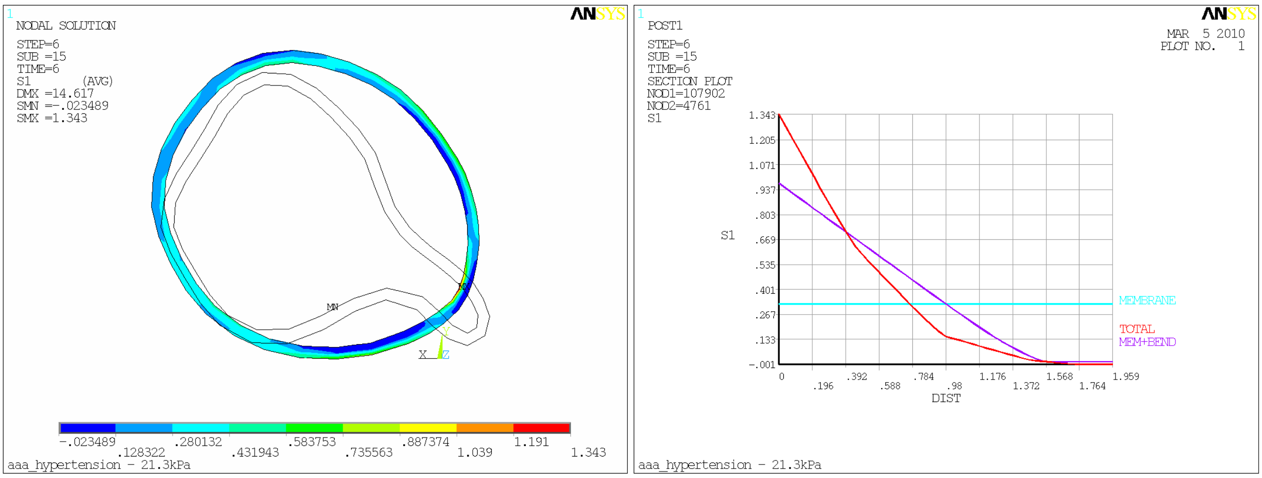

Figure 5-67 Maximum principal stress in cross-section (left) and linearized circumferential (right) Cauchy stress [MPa] through artery thickness at critical location

• anisotropic double-layer exponential constitutive model – first location

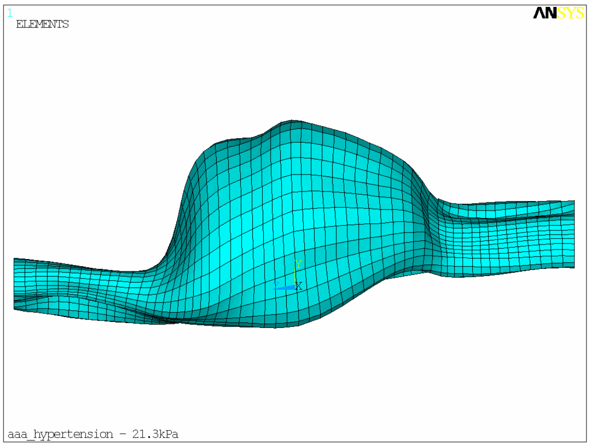

Figure 5-68 FEA mesh

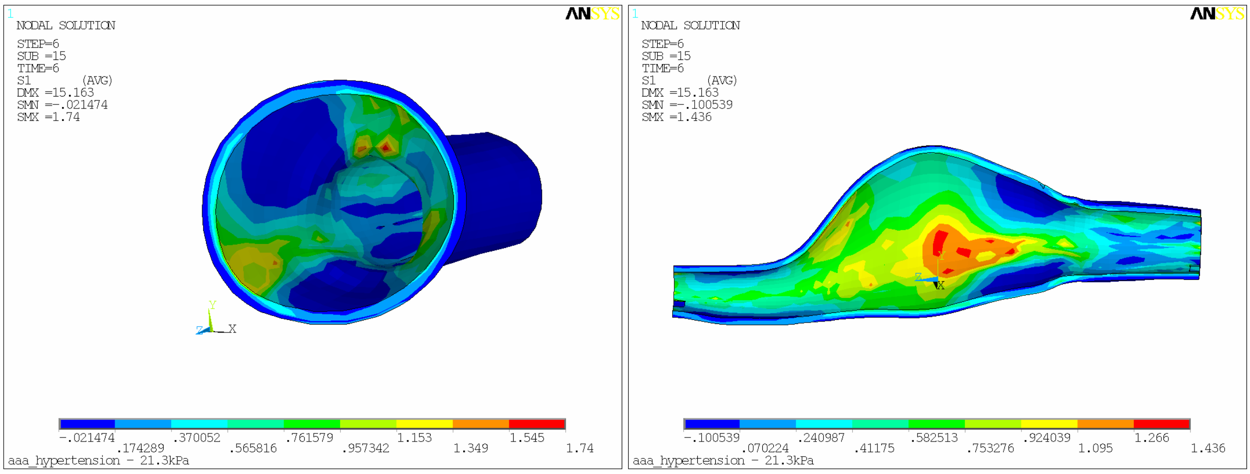

Figure 5-69 Contour plot of the circumferential Cauchy stresses [MPa] – first and second location

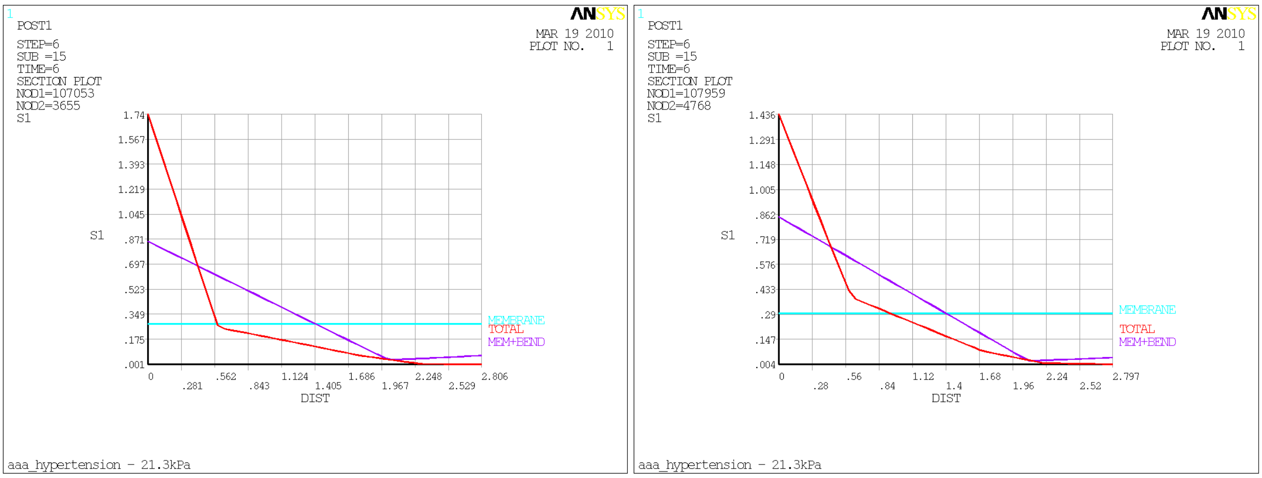

Figure 5-70 Linearized circumferential Cauchy stress [MPa] through artery thickness at first and second critical locations

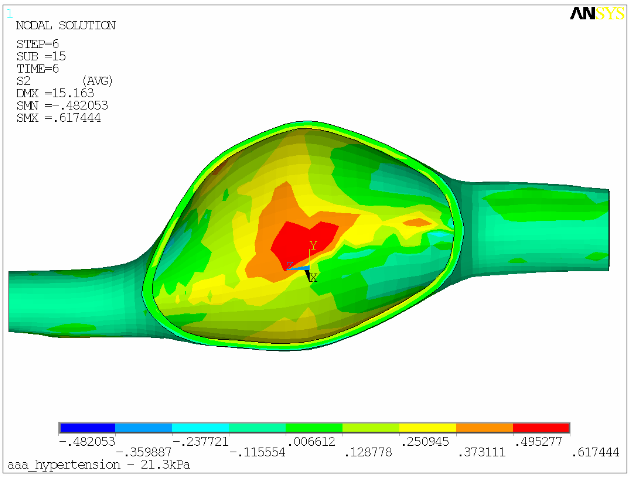

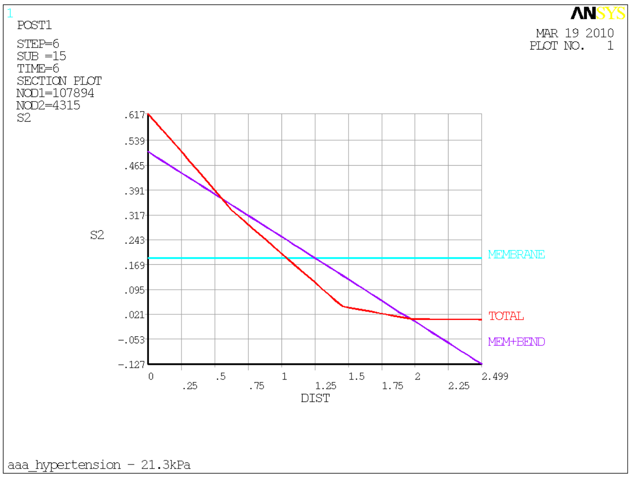

Figure 5-71 Contour plot of the axial Cauchy stress [MPa] (left) and linearized axial (right) Cauchy stress [MPa] through artery thickness at critical location

6 GENERAL DISCUSSION

6.1 Conclusion and future work

As mentioned in chapter 1.2 the main goal of this thesis is to determine the important modeling aspects (described above) significant for prediction of the AAA wall stress and the risk of its rupture. First, this work has attempted to investigate systematically the influence of some factors, such as boundary and loading conditions, on the results of mechanical tests of soft tissues. The conclusions are as follows:

- Influence of preconditioning is important in uniaxial and planar tension tests; on the contrary, no preconditioning is necessary in equibiaxial tension tests. The material behaviour during uniaxial tension tests is in accordance with the findings in literature [12]. It can be concluded that the changes in specimen stiffness are given by a re-orientation of loadbearing fibres towards the direction of the first principal stresses; in equibiaxial tests, however, the in-plane principal stresses are approximately equal, therefore there is no reason for fibre reorientation and no significant preconditioning effect occurs.
- The influence of specimen location is important because the material properties change significantly along the thoracic aorta. Impossibility of getting more specimens from the same location represents a limitation in statistical evaluation of biaxial tension tests and in identification of material parameters of constitutive models.
- Influence of the strain rate is negligible in the tested range ($0.004s^{-1} \sim 0.100s^{-1}$).
- Influence of the tissue freezing is negligible. The mechanical properties show no difference between fresh specimens and those after refrigeration.
- It is impossible to measure the ultimate tensile stress due to the type of the specimen clamping used in the presented equibiaxial testing rig. It would be needed to collect and analyzed the posibilities of the different types of the specimen clamping or the shape of the specimens and to suggest a solution if exists.

The next part of this thesis is focused on FEA modeling. The comprehensive tests presented above brought the following conclusions:

- First the key factors for the creation of the AAA FEA models are summarized and analyzed. The future work should include the mechanical multiaxial testing of the real AAA specimens, because these experimental data absent in up-to-date literature. Additional biaxial tension tests should be aimed at the anatomic location of samples within the AAA in order to study the influence of their location. These characteristic of the AAA tissues are not included in the biaxial study of Van de Geest et al. [34]. The future FEA models should include non-uniform thickness of the AAA wall and different parameters for the constitutive models for the AAA and healthy part of the artery.
- A double-layer exponential model performed at the author´s side was used and analytically and numerically verified. The main advantage of this model is its ability to identify the

parameters for an individual artery layer without the layer separation before the mechanical testing. It is recommended used the multi-layer constitutive model in future AAA analyses because this similarity to the real aortas contributes to more credible simulation of the AAA behavior.

- The Hypothetical idealised geometrical aneurysm model based on several constitutive models is suitable for a better analysis of the influence of each individual geometric variable such as the maximum diameter, asymmetry index and saccular index.
- The probabilistic desing was used for evaluation of the impact of each geometric variable on the stress response in the AAA wall. The analysis based on this methodology is able to predict the extreme stress in dependence of each of the geometrical parameters.
- The backward incremental method used for evaluation of the unloaded geometry based on CT scans was implemented and verified in the ANSYS. Several constitutive models were used for finding of the unloaded geometry. The differences between the single-layer and double-layer FEA models are not negligible therefore it is appropriate in the future to model the individual artery layers in the future, which is more credible and realistic.
- The influence of the hypertension as a one of the key factors for the AAA rupture risk criteria was analyzed using the reconstructed unloaded geometry from the CT scans. The influence of the hypetension is modeled using several constitutive models. The longitudinal stresses were compared with the computed estimated mean value of the ultimate stress. From this point of view the computed stresses are not critical. The ultimate stress was derived from the experimental data using the human thoracic aortas and the pressure-imposed test. It will be necessary to test the real human AAAs with the aim to get the ultimate stress (tension strength) under various biaxial tension states. The initial circumferential stress and influence of the intra-luminal thrombus and calcifications are omitted in the AAA wall stress analyses. These factors should be accounted for in the future AAA more comprehensive wall stress analyses.

6.2 Scope and limitations

All the FEA calculation results are applicable only for the same geometry configuration, constitutive models, type of loading and boundary conditions.

6.3 Clinical perspectives

The results in this thesis describe the influence of the selected geometrical parameters on the AAA wall stress. A significant positive stress-skewness-eccentricity relation of the AAA shape was identified and related with the AAA wall stress. The backward incremental method was implemented and tested in ANSYS. Additional possibilities of the AAA FEA modeling usable to standardize AAA wall stress analysis was also discused. Therefore the future research will be required to increase the accuracy of the AAA wall stress analyses. The clinical relevance of the wall stress evaluations will be now investigated. The cooperation with Clinics of Imaging Methods will be more cooperatively as well as acquisition of CT scans which are essential to next research. The unanswered question is the possibility of the AAA mechanical ex vivo testing that will be world-wide uniquely and comparable with the science findings publicated by the best worl-wide scientific organizations.

7 APPENDIX - A

Tab. 23 Stress comparison (AAA thickness 1.5mm, pressure 16kPa)

AAA thickness 1-5mm, pressure 16kPa								
constitutive model	*c1* [-]	*c4* [-]	F_E [-]	σ1 [Mpa]	σ2 [Mpa]	σ1 nom. [Mpa]	σ1 /σ1 nom.	σ1/σ2
isotropic	0.150	4.750	0.490	0.352	0.223	0.102	3.5	1.6
anisotropic	0.150	4.750	0.490	0.340	0.186	0.103	3.3	1.8
isotropic	0.051	4.750	0.490	0.344	0.213	0.102	3.4	1.6
anisotropic	0.051	4.750	0.490	0.334	0.176	0.102	3.3	1.9
isotropic	0.249	4.750	0.490	0.352	0.231	0.102	3.5	1.5
anisotropic	0.249	4.750	0.490	0.338	0.182	0.103	3.3	1.9
isotropic	0.150	3.513	0.490	0.312	0.197	0.102	3.1	1.6
anisotropic	0.150	3.513	0.490	0.300	0.172	0.102	2.9	1.7
isotropic	0.150	5.988	0.490	0.375	0.252	0.102	3.7	1.5
anisotropic	0.150	5.988	0.490	0.371	0.186	0.104	3.6	2.0
isotropic	0.150	4.750	0.005	0.298	0.182	0.101	3.0	1.6
anisotropic	0.150	4.750	0.005	0.308	0.140	0.101	3.1	2.2
isotropic	0.150	4.750	0.975	0.369	0.262	0.104	3.5	1.4
anisotropic	0.150	4.750	0.975	0.354	0.169	0.105	3.4	2.1
isotropic	0.091	4.014	0.202	0.298	0.163	0.101	3.0	1.8
anisotropic	0.091	4.014	0.202	0.295	0.143	0.101	2.9	2.1
isotropic	0.209	4.014	0.202	0.308	0.184	0.101	3.1	1.7
anisotropic	0.209	4.014	0.202	0.304	0.159	0.101	3.0	1.9
isotropic	0.091	5.486	0.202	0.338	0.216	0.101	3.3	1.6
anisotropic	0.091	5.486	0.202	0.344	0.174	0.102	3.4	2.0
isotropic	0.209	5.486	0.202	0.341	0.220	0.101	3.4	1.6
anisotropic	0.209	5.486	0.202	0.348	0.168	0.102	3.4	2.1
isotropic	0.091	4.014	0.778	0.338	0.213	0.103	3.3	1.6
anisotropic	0.091	4.014	0.778	0.322	0.175	0.103	3.1	1.8
isotropic	0.209	4.014	0.778	0.348	0.233	0.103	3.4	1.5
anisotropic	0.209	4.014	0.778	0.329	0.198	0.103	3.2	1.7
isotropic	0.091	5.486	0.778	0.378	0.266	0.103	3.7	1.4
anisotropic	0.091	5.486	0.778	0.362	0.198	0.105	3.4	1.8
isotropic	0.209	5.486	0.778	0.379	0.267	0.103	3.7	1.4
anisotropic	0.209	5.486	0.778	0.362	0.208	0.105	3.4	1.7

Tab. 24 Stress comparison (AAA thickness 1.9mm, pressure 16kPa)

AAA thickness 1-9mm, pressure 16kPa								
constitutive model	*c1* [-]	*c4* [-]	F_E [-]	σ1 [Mpa]	σ2 [Mpa]	σ1 nom. [Mpa]	σ1 /σ1 nom.	σ1/σ2
isotropic	0.150	4.750	0.490	0.286	0.211	0.078	3.7	1.4
anisotropic	0.150	4.750	0.490	0.298	0.175	0.079	3.8	1.7
isotropic	0.051	4.750	0.490	0.276	0.191	0.079	3.5	1.4
anisotropic	0.051	4.750	0.490	0.286	0.153	0.079	3.6	1.9
isotropic	0.249	4.750	0.490	0.286	0.218	0.078	3.7	1.3
anisotropic	0.249	4.750	0.490	0.299	0.173	0.079	3.8	1.7
isotropic	0.150	3.513	0.490	0.251	0.169	0.079	3.2	1.5
anisotropic	0.150	3.513	0.490	0.257	0.148	0.078	3.3	1.7
isotropic	0.150	5.988	0.490	0.306	0.241	0.079	3.9	1.3
anisotropic	0.150	5.988	0.490	0.328	0.186	0.080	4.1	1.8
isotropic	0.150	4.750	0.005	0.230	0.153	0.078	2.9	1.5
anisotropic	0.150	4.750	0.005	0.259	0.129	0.078	3.3	2.0
isotropic	0.150	4.750	0.975	0.317	0.239	0.080	4.0	1.3
anisotropic	0.150	4.750	0.975	0.320	0.197	0.081	4.0	1.6
isotropic	0.091	4.014	0.202	0.233	0.146	0.078	3.0	1.6
anisotropic	0.091	4.014	0.202	0.245	0.127	0.078	3.1	1.9
isotropic	0.209	4.014	0.202	0.242	0.157	0.078	3.1	1.5
anisotropic	0.209	4.014	0.202	0.258	0.137	0.078	3.3	1.9
isotropic	0.091	5.486	0.202	0.265	0.186	0.078	3.4	1.4
anisotropic	0.091	5.486	0.202	0.296	0.153	0.078	3.8	1.9
isotropic	0.209	5.486	0.202	0.269	0.192	0.078	3.4	1.4
anisotropic	0.209	5.486	0.202	0.301	0.162	0.078	3.9	1.9
isotropic	0.091	4.014	0.778	0.282	0.203	0.080	3.5	1.4
anisotropic	0.091	4.014	0.778	0.282	0.172	0.079	3.6	1.6
isotropic	0.209	4.014	0.778	0.291	0.217	0.079	3.7	1.3
anisotropic	0.209	4.014	0.778	0.293	0.176	0.079	3.7	1.7
isotropic	0.091	5.486	0.778	0.319	0.251	0.080	4.0	1.3
anisotropic	0.091	5.486	0.778	0.328	0.194	0.081	4.0	1.7
isotropic	0.209	5.486	0.778	0.319	0.243	0.079	4.0	1.3
anisotropic	0.209	5.486	0.778	0.328	0.200	0.081	4.0	1.6

Tab. 25 Stress comparison (AAA thickness 2.28mm)

AAA thickness 2-28mm, anisotropic double-layer constitutive model						
c1 [-]	*c4* [-]	F_E [-]	σ1 [Mpa]	σ2 [Mpa]	σ1 nom. [Mpa]	σ1 /σ1 nom.
0.150	4.750	0.490	0.524	0.063	0.223	2.4
0.051	4.750	0.490	0.582	0.129	0.220	2.6
0.249	4.750	0.490	0.515	0.115	0.224	2.3
0.150	3.513	0.490	0.498	0.128	0.218	2.3
0.150	5.988	0.490	0.549	0.119	0.232	2.4
0.150	4.750	0.005	0.458	0.097	0.221	2.1
0.150	4.750	0.975	0.642	0.058	0.233	2.8
0.091	4.014	0.202	0.476	0.098	0.219	2.2
0.209	4.014	0.202	0.480	0.087	0.220	2.2
0.091	5.486	0.202	0.526	0.097	0.222	2.4
0.209	5.486	0.202	0.535	0.048	0.222	2.4
0.091	4.014	0.778	0.499	0.151	0.220	2.3
0.209	4.014	0.778	0.507	0.126	0.222	2.3
0.091	5.486	0.778	0.600	0.096	0.235	2.6
0.209	5.486	0.778	0.587	0.082	0.237	2.5

8 APPENDIX - B

Tab. 26 Stress comparison between individual constitutive models

constitutive model	F_R [-]	c4 [-]	F_E [-]	σ1 [Mpa]	σ1 nom. [Mpa]	σ1 /σ1 nom.
isotropic exponential	2.500	4.750	0.490	0.256	0.078	3.3
isotropic-Yeoh	2.500	4.750	0.490	0.250	0.090	2.8
anisotropic single-layer	2.500	4.750	0.490	0.275	0.078	3.5
anistotropic double-layer	2.500	4.750	0.490	0.494	0.220	2.2
isotropic exponential	2.253	4.750	0.490	0.223	0.078	2.9
isotropic-Yeoh	2.253	4.750	0.490	0.222	0.090	2.5
anisotropic single-layer	2.253	4.750	0.490	0.248	0.078	3.2
anistotropic double-layer	2.253	4.750	0.490	0.455	0.218	2.1
isotropic exponential	2.748	4.750	0.490	0.266	0.072	3.7
isotropic-Yeoh	2.748	4.750	0.490	0.276	0.090	3.1
anisotropic single-layer	2.748	4.750	0.490	0.297	0.079	3.8
anistotropic double-layer	2.748	4.750	0.490	0.567	0.223	2.5
isotropic exponential	2.500	3.513	0.490	0.225	0.078	2.9
isotropic-Yeoh	2.500	3.513	0.490	0.221	0.090	2.5
anisotropic single-layer	2.500	3.513	0.490	0.236	0.078	3.0
anistotropic double-layer	2.500	3.513	0.490	0.450	0.217	2.1
isotropic exponential	2.500	5.988	0.490	0.274	0.078	3.5
isotropic-Yeoh	2.500	5.988	0.490	0.272	0.090	3.0
anisotropic single-layer	2.500	5.988	0.490	0.307	0.079	3.9
anistotropic double-layer	2.500	4.750	0.005	0.422	0.219	1.9
isotropic exponential	2.500	4.750	0.005	0.203	0.078	2.6
isotropic-Yeoh	2.500	4.750	0.005	0.239	0.089	2.7
anisotropic single-layer	2.500	4.750	0.005	0.234	0.078	3.0
anistotropic double-layer	2.500	4.750	0.005	0.422	0.219	1.9
isotropic exponential	2.500	4.750	0.975	0.293	0.079	3.7
isotropic-Yeoh	2.500	4.750	0.975	0.271	0.090	3.0
anisotropic single-layer	2.500	4.750	0.975	0.302	0.080	3.8
anistotropic double-layer	2.500	4.750	0.975	0.541	0.227	2.4
isotropic exponential	2.353	4.014	0.202	0.194	0.078	2.5
isotropic-Yeoh	2.353	4.014	0.202	0.218	0.090	2.4
anisotropic single-layer	2.353	4.014	0.202	0.214	0.078	2.7
anistotropic double-layer	2.353	4.014	0.202	0.416	0.217	1.9
isotropic exponential	2.647	4.014	0.202	0.229	0.078	2.9
isotropic-Yeoh	2.647	4.014	0.202	0.249	0.090	2.8
anisotropic single-layer	2.647	5.486	0.202	0.287	0.078	3.7
anistotropic double-layer	2.647	4.014	0.202	0.478	0.219	2.2
isotropic exponential	2.353	5.486	0.202	0.219	0.078	2.8
isotropic-Yeoh	2.353	5.486	0.202	0.247	0.090	2.7
anisotropic single-layer	2.353	5.486	0.202	0.258	0.078	3.3
anistotropic double-layer	2.353	5.486	0.202	0.468	0.220	2.1
isotropic exponential	2.647	5.486	0.202	0.253	0.078	3.2
isotropic-Yeoh	2.647	5.486	0.202	0.284	0.089	3.2
anisotropic single-layer	2.647	5.486	0.202	0.287	0.078	3.7
anistotropic double-layer	2.647	5.486	0.202	0.524	0.222	2.4
isotropic exponential	2.353	4.014	0.778	0.242	0.079	3.1
isotropic-Yeoh	2.353	4.014	0.778	0.227	0.090	2.5
anisotropic single-layer	2.353	4.014	0.778	0.254	0.078	3.3
anistotropic double-layer	2.353	4.014	0.778	0.443	0.217	2.0
isotropic exponential	2.647	4.014	0.778	0.279	0.079	3.5
isotropic-Yeoh	2.647	4.014	0.778	0.257	0.090	2.9
anisotropic single-layer	2.647	4.014	0.778	0.284	0.079	3.6
anistotropic double-layer	2.647	4.014	0.778	0.483	0.220	2.2
isotropic exponential	2.353	5.486	0.778	0.273	0.079	3.5
isotropic-Yeoh	2.353	5.486	0.778	0.259	0.090	2.9
anisotropic single-layer	2.353	5.486	0.778	0.298	0.079	3.8
anistotropic double-layer	2.353	5.486	0.778	0.470	0.226	2.1
isotropic exponential	2.647	5.486	0.778	0.309	0.079	3.9
isotropic-Yeoh	2.647	5.486	0.778	0.287	0.090	3.2
anisotropic single-layer	2.647	5.486	0.778	0.321	0.080	4.0
anistotropic double-layer	2.647	5.486	0.778	0.512	0.233	2.2

9 REFERENCES

[1] Fung Y. C.: Biomechanics, Material Properties of Living Tissues, 2nd edition, Springer, 1993, New York Berlin Heidelberg.

[2] Humphrey J.D.: Cardiovascular Solid Mechanics, Cells, Tissues, and Organs, Springer, 2002, New York Berlin Heidelberg.

[3] Gasser T.C., Ogden R.W., Holzapfel G.A., Hyperelastic modelling of arterial layers with distributed collagen fibre orientations, J. R. Soc. Interface, 2005, 15-35.

[4] Holzapfel G.A.: Collagen: Structure and Mechanics, Springer Science+Business Media, LLc 2008.

[5] Ogden R.W., Schulze-Bauer C.A.J.: Phenonenological and structural aspects of the mechanical response of arteries, Mechanics in Biology, 2000, 125-140.

[6] Spencer A.J.M.: Constitutive Theory for Strongly Anisotropic Solids. In: A.J.M. Spencer, ed., Continuum Theory of the Mechanics of Fibre-Reinforced Composites, Springer Verlag, Wien, CISM Courses and Lectures No. 282, International Centre for Mechanical Sciences, 1984, 1-31.

[7] Holzapfel G.A., Christian A.J., Schulze-Bauer, Stadler M.: Mechanics of angioplasty: Wall, balloon and stent, Mechanics in Biology, AMD-Vol. 242, BED-Vol. 46, 2000, 141-156.

[8] Holzapfel G.A., Gasser T.C., Ogden R.W.: A new constitutive framework for arterial wall mechanics and a comparative study of material models, Journal of Elasticity, 2000, 61:1-48.

[9] Schulze-Bauer C.A.J., Mörth C., Holzapfel. G.A.: Passive Biaxial Mechanical Response of Aged Human Iliac Arteries, J. Biomechanical Engineering 125 (2003) 395-406.

[10] Holzapfel G.A., Sommer G., Gasser T.C., Regitnig P.: Determination of layer-specific mechanical properties of human coronary arteries with non-atherosclerotic intimal thickening, and related constitutive modelling, American J. Physiology – Heart Circulation Physiology 289 (2005) H2048-2058.

[11] Holzapfel G.A., Sommer G., Auer M., Regitnig P., Ogden W.: Layer-Specific 3D residual deformations of Human Aortas with Non-Atherosclerotic Intimal Thickening, Annals of Biomedical Engineering, Vol. 35, No. 4, April 2007, pp. 530-545.

[12] Schmid F., Sommer G., Rappolt M., Schulze-Bauer C.A.J., Regitnig P., Holzapfel G.A., Laggner P., Amenitsch H.: In situ tensile testing of human aortas by time-resolved small angle X-ray scattering, J. Synchrotron Radiation (2005) 727-733.

[13] Lally C., Reid A.J., Prendergast P.J.: Elastic Behavior of Porcine Coronary Artery Tissue under Uniaxial and Equibiaxial Tension, Annals of Biomedical Engineering 32 (2004) 1355-1364.

[14] Armentano R.L. et al.: An in vitro strudy of cryopreserved and fresh human arteries: a comparison with ePTFE prostheses and human arteries studied noninvasively in vivo, Cryobiology 52 (2006) 17-26.

[15] Wang P. et al.: The viability, structure and mechanical properties of cryopreserved rabbit carotid artery, Cell preservation technology 3 (2005) 85-95.

[16] Venkatasubramanian R.T. et al.: Effects of freezing and cryopreservation on the mechanical properties of arteries, Annals of Biomedical engineering 34 (2006) 823-832.

[17] Stemper B.D. et al.: Mechanics of fresh, refrigerated and frozen arterial tissue, J. Surgical Research 139 (2007) 236-242.

[18] Humphrey J.D., Strumpf R. K., Yin F. C. P.: Determination of a Constitutive Relation for Passive Myocardium: I. A new Functional Form, Journal of Biomechanics Engineering, August, 1990, Vol. 112/335.

[19] Lin D.H.S., Yin F.C.P.: A Multiaxial Constitutive Law for Mammalian Left Ventricular Myocardium in Steady-State Barium Contracture or Tetanus, Transactions of the ASME, August, 1998, Vol. 120/505.

[20] Holzapfel G.A.: Determination of material models for arterial walls from uniaxial extension tests and histological structure, Journal of Theoretical Biology 238, 2006, 290-302.

[21] Patel D.J., Vaishnav R.N.: The Rheology of Large Blood Vessels. Cardiovascular Fluid Dynamics 2, Academic Press, 1972, London and New York.

[22] Takamizawa K., Hayashi K.: Strain energy density function and uniform strain hypothesis for arterial mechanics. Journal of Biomechanics 20, 1987, 20:7-17.

[23] Matsumoto T., Hayashi K.: Stress and strain Distribution in Hypertensive and Normotensive Rat Aorta Considering Residual Strain, Journal of Biomechanical Engineering, February, 1996, Vol. 118, 62-73.

[24] Delfino A., Stergiopulos N., Moore J. E., Meister J. J.: Residual strain effects on the stress field in a thick wall finite element model of the human carotid bifurcation, J. Biomech., 1997, 30:777-786.

[25] Zhong H., Terry M. P.: Exponential Elastic Model and Its Application in Real-Time Simulation, Proc. of SPIE Vol. 6141 61410Y-1, 2006

[26] Young J. M., Beecher E. M., Filas B. A., Taber L. A. and Perucchio R., FEM voxel modeling of the tubular embryonic chick heart for finite stran analysis, Proceeding of the ASME 2008 Summer Bioengineering Conference (SBC2008-192756), June 25-29 2008.

[27] Raghavan M. L., Vorp D. A., Toward a biomechanical tool to evaluate rupture potential of abdominal aortic aneurysm: identification of a finite strain constitutive model and evaluation of its applicability, Journal of Biomechanics 33, 2000, 475-482.

[28] Raghavan M. L., Webster M.W., Vorp D.A.: Ex vivo biomechanical behavior of abdominal aortic aneurysm: Assessment using a new mathematical model, Annals of Biomedical Engineering, Vol. 24, 1996, pp. 573-582.

[29] Raghavan M. L., Kratzberg J., Erasmo Magalhaes Castro de Tolosa, Hanaoka M.M., Walker P., Erasmo Simao da Silva: Regional distribution of wall thickness and failure properties of human abdominal aortic aneurysm, Journal of Biomechanics 39, 2006, pp. 3010-3016.

[30] Raghavan M.L., Fillinger M.F., Marra S.P., Naegelein B.P., Kennedy F.E.: Automated methodogy for determination of stress distribution in human abdominal aortic aneurysm, Journal of biomechanical engineering Vol. 127, October 2005, pp. 868-871.

[31] Raghavan M.L., Ma B., Fillinger M.F.: Non-invasive determination of zero-pressure geometry of arterial aneurysms, Annals of Biomedical Engineering, Vol. 34. No. 9, Septermber 2006, pp. 1414-1419.

[32] Raghavan M., Vorp D., Federle M., Makaroun M., Webster M.: Wall stress distribution on three-dimensionally reconstructed models of human abdominal aortic aneurysm, Journal of Vascular Surgery, 2000, pp. 760-769.

[33] Vorp D.A., Raghavan M.L., Muluk S.C., Makaroun M.S., Steed D.L., Shapiro R., Webster M.W.: Wall strength and stiffness of aneurysmal and nonaneurysmal abdominal aorta, Ann N Y Acad Sci. Nov 18, 1996, pp. 274-276.

[34] Vande Geest J.P., Sacks M.S., Vorp D.A.: The effects of aneurysm on the biaxial mechanical behavior of human abdominal aorta, Journal of Biomechanics 39, 2006, pp. 1324-1334.

[35] Clement Kleinstreuer, Zhonghua Li, Analysis and computer program for rupture-risk prediction of abdominal aortic aneurysms, BioMedical Engineering OnLine, 2006.

[36] Scotti Ch. M., Jimenez J., Muluk S. C., Finol E. A., Wall stress and flow dynamics in abdominal aortic aneurysms: finite element analysis vs. fluid-structure interaction, Computer Methods in Biomechanics and Biomedical Engineering, Vol. 11, No. 3., 2008, 301-322.

[37] E. van Nunen: Modelling Aspects of Stress Analysis for Abdominal Aortic Aneurysm, Master´s thesis, Technische Universiteit Eindhoven, 2004.

[38] Basciano Ch. A.: Computational analysis and simulation of the non-linear arterial wall dynamics with application to abdominal aortic aneurysms, A thesis submitted to the Graduate Faculty of North Carolina State University. 2007.

[39] Peattie R. A., Asbury C. L., Bluth E. I. And Riehle T. J., Steady flow in models of abdominal aortic aneurysms, Part II: Wall stresses and their implication for in vivo Thrombosis and rupture, J. Ultrasound Med., 15(10), pp.689-696, 1996.

[40] Vorp D. A., Raghavan M. L. and Webster M. W., Mechanical wall stress in abdominal aortic aneurysm: Influence of diameter and asymmetry, J. Vasc. Surg., 27, pp. 632-639, 1998.

[41] S. de Putter, On patient-specific wall stress analysis in abdominal aortic aneurysms, Doctoral thesis, Technische Universiteit Eindhoven, 2006.

[42] S. de Putter, Wolters B. J. B. M., Rutten M. C. M., Breeuwer M., Gerritsen F. A., F. N. van de Vosse, Patient-specific inital wall stress in abdominal aortic aneurysm with a backward incremental method, Journal of Biomechanics 40, 2007, 1081-1090.

[43] Lu J., Zhou Xianlian, Raghava M. L., Inverse elastostatic stress analysis in pre-deformed biological structures: Demonstration using abdominal aortic aneurysms, Journal of Biomechanics 40, 693-696, 2007.

[44] Lu J., Zhou Xianlian, Raghava M. L., Computational method of inverse elastostatics for anisotropic hyperelastic solids, International journal for numerical methods in engineering 69, 2007, pp. 1239-1261.

[45] Rodríguez J. F., Ruiz C., Doblaré M., Holzapfel G. A.: Mechanical stresses in abdominal aortic aneurysms: Influence of diameter, asymmetry, and material anisotropy, Journal of Biomechanical Engineering, Vol. 130/021023-1, 2008.

[46] Wang W.Q., Liang D.K., Yang D.Z., Qi M.: Analysis of the transient expansion behavior and design optimization of coronary stents by finite element method, Journal of Biomechanics 39, 2006, 21-32.

[47] Ohashi T., Sugita S., Matsumoto T., Kumagai K., Akimoto H., Tabayashi K., Sato M.: Rupture properties of blood vessel walls measured by pressure-imposed test, JSME Internation Journal, Series C, Vol. 46, No. 4, 2003, 1290-1296.

[48] Xenos M., Rambhia S., Alemu Y., Einav S., Ricotta J. J., Labropoulos N., Tassiopoulos A., Bluestein D.: Mimics based image reconstruction augments diagnosis and management of vascular pathologies: A study of ruptured abdominal aortic aneurysms. Mimics Innovation Awards 2009 2nd place. http://bme.sunysb.edu/people/faculty/d_bluestein.html

[49] Mohan D., Melvin J.W.: Failure properties of passive human aortic tissue I – uniaxial tension tests, J. Biomechanics Vol. 15, No. 11, 1982, pp. 887-902.

[50] Mohan D., Melvin J.W.: Failure properties of passive human aortic tissue II – biaxial tension tests, J. Biomechanics Vol. 16, No. 1, 1982, pp. 31-44

[51] Roy C.S.: Elastic properties of arterial wall. J. Physiol,. Lond. 3, 1880, pp. 129-159.

[52] Thubrikar M.J., Al-Soudi J, Robicsek F.: Wall stress studies of abdomina aortic aneurysm in a clinical model, Annals of Vascular Surgery 15(3), 2001, pp. 355-366.

[53] Hierton T. E., Jordan P.: The tensile strength of canine aortic segments. Angiology 7, 1956, pp. 67-76.

[54] Milch R.A.: Matrix properties of the aging arterial wall. Monogr. Surs. Sci. 2, 1965, pp. 261-341.

[55] Wolinsky H., Glagov S.: Structural basis for the static mechanical properties of the aortic media. Circulation Res. XIX, 1964, pp. 400-413.

[56] Gasbarro M.D., di Martino E.S., Scotti C.M., Finol E.A. and Shimada K.: Computational modeling of abdominal aortic aneurysms: A new simulation technique that demonstrates the importance of including realistic fluid motion, spinal column, and internal organs, Proceeding of the 2005 Summer Bioengineering Conference, Vail CO, 2005.

[57] Speelman Lambert, Biomechanical analysis for abdominal aortic aneurysm risk stratification, Proefschrift, December 2009.

[58] Scotti C.M., Shkolnik A.D., Muluk S.C., Finol E.A.: Fluid-structure interaction in abodiminal aortic aneurysms: Effect of asymmetry and wall thickness, Biomedical Engineering OnLine 2005, 4:64.

[59] Wang D., Makaroun M., Webster M., Vorp D.A.: Effect of intraluminal thrombus in abdominal aortic aneurysm, Journal of Vascular Surgery, 2002, 3:598-604.

[60] Wolf Y.G., Thomas W.S., Brennan F.J., Goff W.G., Sise M.J., Bernsten E.F.: Computed tomography scanning findings associated with rapid expansion of abdominal aortic aneurysm, Journal of Vascular Surgery, 1994, 20:529-538.

[61] Skácel P., Burša J.: Material parameter identification of arterial wall layers from homogenized stress-strain data, Computer Method in Biomechanics and Biomedical Engineering, 2010, preliminary accepted.

[62] Ryšavý P.: Deformačně-napěťová analýza aneurysmatu břišní aorty, Pojednání ke státní doktrorské zkoušce, 2008.

[63] ANSYS User´s Manual, Version 11.0.

[64] STATISTICA User´s Manual, Version 7.

[65] http://www.nlm.nih.gov/medlineplus/ency/imagepages/18072.htm

[66] http://www.healthpoints.info/

[67] http://www.nhlbi.nih.gov/health/dci/Diseases/arm/arm_treatments.html

[68] http://www.vascularweb.org/patients/NorthPoint/Abdominal_Aortic_Aneurysm.html

[69] http://www.daylife.com/photo/0402gXA2fubf1

[70] http://www.arid.cz/

[71] http://en.wikipedia.org/wiki/Aneurysm

[72] http://en.wikipedia.org/wiki/Correlation_coefficient

[73] http://en.wikipedia.org/wiki/Hypertension

[74] http://www.statistics4u.info/fundstat_eng/cc_corr_spearman.html

[75] http://www.mayoclinic.org/aortic-aneurysm/types.html

[76] http://www.daviddarling.info/encyclopedia/A/aneurysm.html

[77] http://www.scopus.com/authid/detail.url?authorId=24280895000

10 AUTHOR´S PUBLICATIONS

Journal articles

I. Zemánek M., Burša J., Děták M.: Biaxial tension tests with soft tissues of arterial wall, Engineering mechanics, Vol. 16, 2009, ISSN 1802-1484, pp. 3-12, Engineering Academy of the Czech Republic.
II. Burša J., Zemánek M.: Evaluation of Biaxial Tension Tests of Soft Tissues, Technology and Informatics, Vol. 133, 2007, No.1, ISSN 0926-9630, IOS Press, pp. 45-55, Regensburg Applied Biomechanics.

Conference papers

III. Děták M., Burša J., Zemánek M.: Influence of geometric simplifications on stresses and strains in aneurysm model, IFMBE Proceedings, ISBN 978-3-642-03897-6, 2009, pp. 529-532.
IV. Děták M., Burša J., Zemánek M.: Biaxial tensile testing of porcine aortas, Human Biomechanics 2008, pp.38. ISBN 978-80-01-04163-5, Czech Society of Biomechanics.
V. Burša J., Skácel P., Zemánek M., Kreuter D.: Implementation of hyperelastic models for soft tissues in FE program and identification of their parameters, Proccedings of the Sixth IASTED International Conference on Biomedical Engineering, 2008, ISBN 978-0-88986-722-2, pp.205-209.
VI. Zemánek M., Burša J.: Identification of parameters of constitutive models for soft tissues from biaxial tension tests, Engineering Mechanics 2007, pp. 327-328, Academy of Sciences of the Czech Republic, v.v.i., Prague. ISBN 978-80-87012-06-2.
VII. Zemánek M., Burša J.: Identification of parameters of hyperelastic models from biaxial tension tests, Experimental Stress Analysis 2007, pp. 121-122. ISBN 978-80-7043-552-6.
VIII. Zemánek M., Burša J.: Zařízení pro dvojosé tahové zkoušky měkkých tkání, 7th International Scientific Conference Applied Mechanics 2005, pp.84. ISBN 80-214-2373-0.

The 2 documents (II and V) were incorporated in international database SCOPUS. The first mentioned document was cited in SCOPUS [77].

11 AUTHOR´S CURRICULUM VITAE

Ing. ZEMÁNEK MIROSLAV

Telephone Number: +420737721794
E-mail: zemanek.miroslav@centrum.cz

Career profile

Specialist in structural designs of product components using linear and nonlinear FEM analysis tools and design of recommendation to the product development teams.

Key areas of expertise

Stress and thermal analysis, dynamic and transient analysis, contact analysis, design of optimization.

Professional experience

11/2005 – present: L. K. Engineering, Brno, Czech Republic, www.lke.cz
Analytical Engineer

- Stress, thermal and dynamic analysis of electrical generator components.
- Thermal and lifetime qualification (fracture mechanics and fatigue evaluation).
- Large and complex nonlinear models (contacts, plasticity).
- Seismic analysis of base frames of machine components.
- Verification and analysis of results, documentation of methodology and results.
- Example projects:
    - design of generator rotor retaining ring assembly
    - design of generator rotor end winding connectors
    - design of generator rotor blower blades assembly
    - design of turbocharger turbo-housing
    - design of turbocharger bearing-housing
    - design and analysis of components for axial overpressure fans
    - seismic analysis of base frames for glass wasching machine

Education & training

2004 - present
BRNO UNIVERSITY OF TECHNOLOGY, Faculty of Mechanical Engineering, Czech Republic
Ph.D. studies
Specialization: Applied Mechanics / Biomechanics
Topic of the dissertation thesis: Influence of geometrical parameters on rupture risk of abdominal aortic aneurysm.

1999 - 2004
BRNO UNIVERSITY OF TECHNOLOGY, Faculty of Mechanical Engineering, Czech Republic
Degree in Applied Mechanics, M.Sc. equivalent
Specialization: Applied Mechanics / Biomechanics
Thesis: Analysis of viscoelastic behavior of artery wall.

1993 – 1997
ISŠT BOSKOVICE, Czech Republic.
Specialization: Engineering management

Skills

Languages:	Czech (primary), English - intermediate.
Operating systems:	Windows XP.
Software:	ANSYS, Pro-Engineer, MathCAD, Statistica, MS_Office

References

Available upon request.